

**TR-687: Effect of Wind Induced Unsteady Vortex Shedding, Diurnal  
Temperature Changes, and Transit Conditions On Truss Structures  
Supporting Large Highway Signs**

**Final Report  
March 2018**

Submitted by

**George Constantinescu and Asghar Bhatti**  
Department of Civil & Environmental Engineering  
and  
IIHR-Hydrosience and Engineering Hydraulics Laboratory  
The University of Iowa  
Iowa City, IA

**Brent Phares**  
Department of Civil, Construction, and Environmental Engineering  
and  
The Bridge Engineering Center at the Institute for Transportation.  
Iowa State University  
Ames, IA

**Authors:**

Univ. Iowa: G. Constantinescu (ORCID 0000-0001-7060-8378), M. A. Bhatti (ORCID 0000-0002-0254-1367), D. Horna Munoz (ORCID 0000-0003-2493-9154), K. Basnet (0000-0003-1082-7866)

Iowa State Univ.: B. Phares (ORCID 0000-0001-5894-4774), B. Shafei (ORCID 0000-0001-5677-6324), S. Arabi (ORCID 0000-0002-5681-4922)

**Sponsored by**  
The Iowa Highway Research Board  
Iowa Department of Transportation  
And  
Federal Highway Administration

**Disclaimer Notice**

The contents of this report reflect the views of the authors, who are responsible for the facts and the accuracy of the information presented herein. The opinions, findings, and conclusions expressed in this publication are those of the authors and not necessarily of the sponsors. The sponsors assume no liability for the contents or use of the information contained in this document. This report does not constitute a standard, specification, or regulation.

The sponsors do not endorse products or manufacturers. Trademarks or manufacturer's names appear in this report only because they are considered essential to the objectives of the document.

**Statement of Non-Discrimination**

Federal and state laws prohibit employment and/or public accommodation discrimination on the basis of age, color, creed, disability, gender identity, national origin, pregnancy, race, religion, sex, sexual orientation or veteran's status. If you believe you have been discriminated against, please contact the Iowa Civil Rights Commission at 800-457-4416 or Iowa Department of Transportation's affirmative action officer. If you need accommodations because of a disability to access the Iowa Department of Transportation's services, contact the agency's affirmative action officer at 800-262-0003.

The University of Iowa does not discriminate on the basis of race, color, age, religion, national origin, sexual orientation, gender identity, sex, marital status, disability, or status as a U.S. veteran. Inquiries can be directed to the Director of Equal Opportunity and Diversity at the University of Iowa, (319) 335-0705. Iowa State University does not discriminate on the basis of race, color, age, religion, national origin, pregnancy, sexual orientation, gender identity, genetic information, sex, marital status, disability, or status as a U.S. veteran. Inquiries regarding non-discrimination policies may be directed to Office of Equal Opportunity, Title IX/ADA Coordinator and Affirmative Action Officer, 3350 Beardshear Hall, Ames, Iowa 50011, 515-294-7612, eooffice@iastate.edu.

**Acknowledgements**

The authors would like to thank the Iowa Highway Research Board and the Federal Highway Administration for supporting this study. The authors would also like to thank all the members of the Technical Advisory Committee for their advice and guidance and Ms. Vanessa Goetz for overseeing this project.

<b>1. Report No.</b> <b>TR-687</b>	<b>2. Government Accession No.</b> Optional	<b>3. Recipient Catalog No.</b> Optional
<b>4 Title and Subtitle</b>  Effect of Wind Induced Unsteady Vortex Shedding, Diurnal Temperature Changes, and Transit Conditions On Truss Structures Supporting Large Highway Signs		<b>5 Report Date</b> March 1, 2018
<b>Author(s)</b> G. Constantinescu (ORCID 0000-0001-7060-8378), M. A. Bhatti (ORCID 0000-0002-0254-1367), B. Phares (ORCID 0000-0001-5894-4774), B. Shafei (ORCID 0000-0001-5677-6324), D. Horna Munoz (ORCID 0000-0003-2493-9154), K. Basnet (0000-0003-1082-7866) S. Arabi (ORCID 0000-0002-5681-4922)		<b>6 Performing Organization Code</b> N/A  <b>8 Performing Organization Report No.</b>
<b>9 Performing Organization Name and Address</b> Dept. Civil and Environmental Engineering, The University of Iowa, Iowa City, IA, 52242 and Dept. Civil, Construction and Environmental Engineering and The Bridge Engineering Center at the Institute for Transportation, Iowa State University, Ames, Iowa.		<b>10 Work Unit No. (TRAIS)</b> Not Required
<b>12 Sponsoring Organization Name and Address</b> Iowa Department of Transportation 800 Lincoln Way Ames, Iowa 50010  Federal Highway Administration		<b>11 Contract or Grant No.</b> SPR Part II Funds
<b>15 Supplementary Notes</b> None		<b>13 Type of Report and Period Covered</b> Final Report  <b>14 Sponsoring Agency Code</b> <b>TR-687</b>

## 16 Abstract

Highway sign structures are called upon to support a variety of signs including large dynamic message signs (DMS) to better manage traffic flow by providing accurate and timely information to drivers. Overhead truss structures are employed to support DMS cabinets. DMS cabinets are much heavier, and have different depths and aspect ratios than typical highway signs. The current American Association of State Highway and Transportation Officials (AASHTO) *LRFD Specifications for Structural Supports for Highway Signs, Luminaries and Traffic Signals* (AASHTO 2015), which is the main document used for design of sign support structures by state DOTs in the US, do not give clear guidance for estimating wind loads in these situations. This increases the uncertainty in estimating stresses induced in the members of the truss structure supporting the DMS cabinet. Having detailed understanding of stresses caused during the service life of the trusses supporting DMS cabinets is crucial for their safe and economic design. In recent years, there is increasing evidence that the truss structures supporting a variety of large and heavy signs are subjected to much more complex loading than those typically accounted for in the codified design procedures. Consequently, some of these structures have required frequent inspections, retrofitting, and even premature replacement. In order to reliably predict the behavior of these structures, and to design them properly, detailed knowledge of the wind forces is obviously necessary. The first objective of this study is to accurately estimate unsteady wind loads acting on the DMS cabinets and other traffic signs and on the members of the truss structures supporting these signs. The cyclic oscillations of the total wind load associated with vortex shedding behind the signs may be a main contributor to premature fatigue failure. This is because these cyclic oscillations that occur even under steady incoming wind conditions can create a resonance condition.

Besides wind loading, the highway sign structures may be subjected to fatigue induced by stresses caused during the transport of trusses to the site and those caused by large diurnal temperature variations. Thus the second objective is to investigate possible fatigue failure due to vibrations during transportation from fabricator to the site where the truss and DMS cabinet will be deployed. The third objective is to investigate diurnal temperature effects on the fatigue life of structures.

The study was divided into two parts. The computational fluid dynamics (CFD) study, related to the first objective, was conducted by the University of Iowa. The truss monitoring during its transport and monitoring of diurnal temperature effects related to second and third objectives were conducted by Iowa State University. In Part I detailed CFD simulations were conducted to determine the air-induced mean (time-averaged) wind forces on the DMS cabinets and normal traffic signs of different configurations of interest to the Iowa DOT. The time-accurate simulations resolve the large scale turbulent eddies in the wake of the sign and take into account the unsteady wind loads associated with vortex shedding behind the sign. Based on this information, the mean drag coefficients for the DMS cabinets and other traffic signs were estimated. The CFD simulations also provided the time series of the instantaneous drag coefficient, based on which the main variables required to perform a structural fatigue analysis of the support structure can be estimated. A significant finding of this study was that AASHTO 2015 underestimates the wind drag coefficient for signs by as much as 25%. At the same time, the CFD results show that the *Minimum Design Loads for Buildings and Other Structures* (ASCE/SEI 7-10) recommendations for the design of aluminum sign structures is too conservative. The other main contribution of Part I was to propose a relatively simple procedure to estimate drag forces on the members of the support structure (e.g., truss). The current procedures to estimate wind loads on the members of the supporting structures are based on many simplifying assumptions and are not straightforward to apply for practical cases (e.g., as described in NCHRP Project 17-10(2), various AASHTO and ASCE specifications, and design manuals used by state DOTs). The proposed procedure is much simpler and less confusing than current procedures used by the Iowa DOT. In Part II, a detailed vulnerability assessment of sign support structures during transportation was conducted. To investigate the possibility and extent of damage during transportation, a detailed experimental and numerical study was conducted. One span of an overhead DMS-support truss was instrumented with strain gauges to measure the stress/strain induced during transportation. A numerical model was developed to quantitatively characterize vibration induced by the road profile. Several types of road roughness profiles were considered. Besides the data collected from the field, a detailed finite element model of the complete structure was created to obtain an in-depth understanding of the potential modes of damage and failure. A main finding of the fatigue analysis conducted for the truss structure was that transportation over a few hours can cause fatigue damage similar to up to months of in service loading. A fatigue analysis based on real time field monitoring of DMS support structures under long-term environmental conditions was also conducted. Beside the experimental study, a detailed finite element model was developed to investigate the fatigue life of the most critical parts of structure. Based on both experimental and numerical study, it was found that the diurnal temperature variations do not have a major effect on the truss structures used to support highway signs in Iowa.

<b>17 Key Words</b> Dynamic message cabinets, traffic signs, supporting trusses, wind loads, drag coefficient, fatigue.		<b>18 Distribution Statement</b> No restrictions. This document is available to the public through the National Technical Information Service, Springfield, Virginia 22161	
<b>19 Security Classification (of this report)</b> Unclassified	<b>20 Security Classification (of this page)</b> Unclassified	<b>21 No. of pages</b> 108	<b>22 Price</b> N/A

**Form DOT F 1700.7 (8-72)**

This page left intentionally blank

## TABLE OF CONTENTS

Executive Summary	9
1. Introduction	11
1.1. Background	11
1.2. Objectives	12
1.3. Main components of the study	14
2. Estimation of wind forces acting on traffic signs and members of the trusses supporting these traffic signs	14
2.1. Problem statement and present state of knowledge	14
2.2. Literature review	15
2.3. Numerical methodology used to estimate wind loads and drag coefficients	17
2.4. Validation: Flow past a wide thin plate with perpendicular incoming wind	20
2.5. Estimation of drag coefficient for an isolated DMS cabinet with varying incoming wind direction	21
2.6. Estimation of drag coefficient for traffic signs with perpendicular incoming wind	30
2.7 Effect of clearance ratio and sign aspect ratio on drag coefficient for a traffic sign with perpendicular incoming wind	31
2.8 Estimation of drag coefficients for the members of the truss supporting a DMS cabinet	32
3. Vulnerability assessment of sign support structures during transportation	37
3.1. Literature review	37
3.2. Field study	37
3.3. Numerical study	39
3.3.1. Road profiles	39
3.3.2. Suspension system	39
3.3.3. Validation of FE model	41
3.4. Results and discussion	41
3.4.1. Stress concentration factor	41
3.4.2. Fatigue damage analysis	42
4. Vulnerability assessment of Dynamic Message Sign support structures under environmental stressors	55
4.1. Field investigation and monitoring	55

4.1.1. DMS-support truss structures	56
4.1.2. Monitoring system setup	56
4.1.3. Findings from long-term data	56
4.2. Numerical modeling	57
4.3. Fatigue Analysis	58
4.4. Comparison of steel and aluminum DMS-support structures	60
5. Summary, conclusions and recommendations for future work	74
References	77

## Executive Summary

Highway sign structures are called upon to support a variety of signs including large dynamic message signs (DMS) to better manage traffic flow by providing accurate and timely information to drivers. Overhead truss structures are typically employed to support DMS cabinets allowing wide display over more lanes. DMS cabinets are much heavier, and have different depths and aspect ratios than typical highway signs. The current American Association of State Highway and Transportation Officials (AASHTO) *LRFD Standard Specifications for Structural Supports for Highway Signs, Luminaries and Traffic Signals* (AASHTO 2015), which is the main document used for design of sign support structures by state DOTs in the US, do not give clear guidance for estimating wind loads in these situations. This increases the uncertainty in estimating stresses induced in the members of the truss structure supporting the DMS cabinet. Having detailed understanding of stresses caused during the service life of the trusses supporting DMS cabinets is crucial for their safe and economic design. In recent years, there is increasing evidence that the truss structures supporting a variety of large and heavy signs are subjected to much more complex loadings than those typically accounted for in the codified design procedures. Consequently, some of these structures have required frequent inspections, retrofitting, and even premature replacement. Wind and strain resulting from temperature changes are main loads that affect the structures during their lifetime. In order to reliably predict the behavior of these structures, and to design them properly, detailed knowledge of the wind forces is obviously necessary.

The recent Iowa DOT project TR612: ‘Wind loads on dynamic message cabinets and behavior of supporting trusses’ has shown that the diurnal temperature variations may play an important role in explaining the development of cracks observed at some of the trusses supporting DMS cabinets. The same study also identified other possible causes for the development of cracks: 1) unsteady loads induced by vortex shedding behind the DMS cabinets, and 2) fatigue induced during the transport of trusses to the site. These two probable causes are investigated in the present study.

The first objective of this study is to accurately estimate unsteady wind loads acting on the DMS cabinets and other traffic signs and on the members of the truss structures supporting these signs. The cyclic oscillations of the total wind load associated with vortex shedding behind the signs may be a main contributor to premature fatigue failure. This is because these cyclic oscillations that occur even under steady incoming wind conditions can create a resonance condition.

Besides wind loading the highway sign structures may be subjected to fatigue induced by stresses caused during the transport of trusses to the site and those caused by large diurnal temperature variations. Thus the second objective is to investigate possible fatigue failure due to vibrations during transportation from fabricator to the site where the truss and DMS cabinet will be deployed. The third objective is to investigate diurnal temperature effects on the fatigue life of structures.

The study is divided into two parts. The computational fluid dynamics (CFD) study, related to the first objective, was conducted by the University of Iowa. The truss monitoring during its transport and monitoring of diurnal temperature effects related to second and third objectives were conducted by Iowa State University. In Part I detailed CFD simulations are conducted to determine the air-induced mean (time-averaged) wind forces on the DMS cabinets and normal traffic signs of different configurations of interest to the Iowa DOT. The time-accurate simulations resolve the large scale turbulent eddies in the wake of the sign and take into account the unsteady wind loads associated with vortex shedding behind the sign. Based on this information, the mean drag coefficients for the DMS cabinets and other traffic signs are estimated. The CFD simulations also provide the time series of the instantaneous drag coefficient, based on which the main variables required to perform a structural fatigue analysis of the support structure can be estimated. A significant finding of this study is that AASHTO 2015 underestimates the wind drag coefficient for signs by as much as 25%. At the same time, the CFD results show that the *Minimum Design Loads for Buildings and Other Structures* (ASCE/SEI 7-10) recommendations for the design of aluminum sign structures is too conservative. The other main contribution of Part I is to propose a relatively simple procedure to estimate drag forces on the members of the support structure (e.g., truss). The current procedures to estimate wind loads on the members of the supporting structures are based on many simplifying assumptions and are not straightforward to apply for practical cases (e.g., as described in NCHRP Project 17-10(2), various AASHTO and ASCE specifications, and design manuals used by state DOTs). The proposed procedure is much simpler and less confusing than current procedures used by the Iowa DOT. In Part II, a detailed vulnerability assessment of sign support structures during transportation are conducted. To investigate the possibility and extent of damage during transportation, a detailed experimental and numerical study is conducted. One span of an overhead DMS-support truss was instrumented with strain gauges to measure the stress/strain induced during transportation. A numerical model was developed to quantitatively characterize vibration induced by the road profile. Several types of road roughness profiles are considered. Besides the data collected from the field, a detailed finite element model of the complete structure was created to obtain an in-depth understanding of the potential modes of damage and failure. A main finding of the fatigue analysis conducted for the truss structure is that transportation over a few hours can cause fatigue damage similar to up to months of in-service loading. Results of a fatigue analysis based on real time field monitoring of DMS support structures under long-term environmental conditions are also reported. Beside the experimental study, a detailed finite element model is developed to investigate the fatigue life of the most critical parts of structure. Based on both experimental and numerical study, it is found that the diurnal temperature variations do not have a major effect on the truss structures used to support highway signs in Iowa.

# 1. Introduction

## 1.1. Background

The desire to provide drivers with up-to-date information on highway conditions has resulted in increased use of dynamic message sign (DMS) cabinets which are typically much heavier, and have different depths and aspect ratios than typical highway signs. Overhead truss structures are usually employed to support DMS cabinets allowing wide display over more lanes. As a result, the structural performance assessment of the overhead truss structures that support such DMS cabinets has become a subject of interest for those working on the design and maintenance of transportation infrastructure components. The failure of structures supporting large highway signs can result in accidents and even loss of life. This points to limitations in the current design guidelines. Given the hazard risk and also the large costs of prematurely replacing these structures, there is a demonstrated and urgent need to investigate all possible causes that can lead to failure of structures supporting large highway signs.

Having detailed understanding of stresses caused during the service life of the trusses supporting DMS cabinets is crucial for their safe and economic design. This in turn requires an accurate estimation of the wind loads acting on the DMS cabinets. There is increasing evidence that the truss structures supporting a variety of large and heavy signs are subjected to much more complex loadings than those typically accounted for in the codified design procedures (Stam et al., 2011). In addition, contribution of stresses induced during transportation from the fabricator to the site is also largely unknown. Consequently, some of these structures have required frequent inspections, retrofitting, and even premature replacement.

In order to reliably predict the behavior of highway sign support structures and to design them properly detailed knowledge of all potential causes of failure is required. Most of previous efforts were, however, primarily focused on wind load effects and neglected the potential contribution of thermal stresses that can cause damage to the truss structures, particularly at their joints. A potentially important effect of diurnal temperature variation was investigated in a recent Iowa DOT sponsored project completed by the present research team *TR612: 'Wind loads on dynamic message cabinets and behavior of supporting trusses'*. The study showed that the diurnal temperature variations may play an important role in explaining the development of cracks observed at some of the trusses supporting DMS cabinets. The study also identified other possible causes for the development of cracks, namely unsteady loads induced by vortex shedding behind the DMS cabinets and fatigue induced during the transport of the trusses to the site.

The current design practice for overhead truss structures is in accordance with the *LFRD Specifications for Structural Supports for Highway Signs, Luminaries and Traffic Signals* (AASHTO 2015). The specifications include updated provisions and criteria for extreme wind loads and new provisions and criteria on fatigue design. In particular, the AASHTO specifications address the effects of wind load, dead load, live load, ice load, and fatigue design for natural wind gust and truck-induced gust. An important observation is that the

AASHTO standard does not account for premature fatigue failure due to the cyclic oscillations of the total wind load associated with vortex shedding behind the sign nor for fatigue induced by diurnal oscillations in the temperature. Furthermore it does not give clear guidance for estimating wind loads for DMS cabinets which increases the uncertainty in estimating stresses induced in the members of the truss structures supporting these DMS cabinets.

## **1.2. Objectives**

The main goal of this study is to investigate probable causes of stresses leading to fatigue cracking in trusses supporting a variety of highway signs including DMS cabinets. The study involves computational fluid dynamics (CFD) simulations, field monitoring and structural analysis.

The first main objective of this study is to accurately estimate unsteady wind loads acting on the DMS cabinets and other traffic signs and on the members of the truss structures supporting these signs. Given that wind is the main load that affects the trusses during their lifetime, accurate estimation of the wind loads is essential. Moreover, the cyclic oscillations of the total wind load associated with vortex shedding behind the signs may be a main contributor to premature fatigue failure. In particular, it is important to understand how the mean drag coefficient for the traffic sign varies with the sign aspect ratio and the clearance to the ground. These drag coefficients can then be compared with those given in AASHTO 2015 to see if the current procedures are too conservative or, on the contrary, they underestimate the wind loads on traffic signs.

The second objective is to investigate stresses and the resulting damage induced during the transportation of highway sign support trusses from fabricator to the site where the truss and DMS cabinet will be deployed. To address the second objective, a short term monitoring and a finite element investigation is conducted. As part of the field investigation, one span of a four-chord overhead sign support structure is instrumented to perform short-term structural health monitoring. In addition, detailed finite element simulations are carried out to obtain an in-depth understanding of the potential modes of damage under vibrations induced by the road profile. The outcome of this study is the assessment of structural vulnerability of DMS-support structures during transportation.

The third objective is to evaluate damage induced by large diurnal temperature fluctuations. To address this objective, two overhead DMS support structures located in Iowa were selected for instrumentation and long-term monitoring. The case-study structures are unique because while they are close to each other and experience similar environmental conditions, one is in the north-south and the other is in the east-west direction. This helps to investigate sunlight as a factor contributing to potential damage. Through a comprehensive instrumentation plan, several vibrating-wire sensors are installed on these two support structures to understand the effects of diurnal temperature changes. In addition to field tests, detailed finite element simulations are conducted to obtain an in-depth understanding of the potential modes of damage and failure.

Finally, recommendations are made for inclusion in the specifications for design of highway sign support structures with respect to the main findings of the three components of the study.

### **1.3. Main components of the study**

The analysis of the wind forces acting on traffic signs and on the members of the trusses supporting these traffic signs was conducted at the University of Iowa. Chapter 2 discusses the latest findings related to estimation of the drag coefficients for traffic signs based on laboratory experiments and points toward some inconsistencies between the values recommended by the present AASHTO 2015 standard and those obtained experimentally. It then describes the numerical methodology adopted in the present study to accurately calculate the wind loads acting on traffic signs, and in particular on DMS cabinets. The chapter includes results of a detailed study on how the mean (time-averaged) drag coefficient of DMS cabinets and thin rectangular signs varies with the distance from the ground and the sign aspect ratio. These values are obtained based on time-accurate highly-resolved three dimensional (3-D) simulations using a detached eddy simulation model that resolves the large-scale turbulent eddies and in particular the vortex shedding in the wake of the traffic sign. The chapter also includes results of steady Reynolds-Averaged Navier-Stokes (RANS) simulations performed for a DMS cabinet attached to a truss. These results are used to propose a simple way to estimate wind loads on the individual members of structures supporting highway signs. Recommendations are developed on how to split the support structure into different regions and give values of the drag coefficients to be used for the unshielded and shielded members within these regions.

The studies related to the damage induced during transportation of trusses supporting traffic signs and that induced by the change of temperature in the regions that experience large diurnal temperature fluctuations were conducted at Iowa State University. Chapter 3 reports a comprehensive short-term monitoring field study paired with detailed numerical simulations conducted on a four-chord sign support structure during transportation from the fabricator to the installation site. The distributions of strains and stresses within the entire truss members are obtained from a finite element model analysis. The effects of road roughness on the potential of experiencing fatigue-induced damage due to vibrations transferred to the truss structure are also discussed. The same chapter also reports results of a fatigue analysis that was conducted using both the field data and simulation results. Chapter 4 reports results of a comprehensive field study and of numerical simulations that were conducted for two overhead DMS support structures located in Iowa. The main purpose of the field and numerical work is to investigate sunlight as a factor contributing to potential damage of the truss members and the potential thermally-induced damage of the truss supporting the DMS cabinet. The chapter reports results of a detailed fatigue life analysis conducted for steel overhead DMS support structures using field data and results of finite element analysis. It also compares the fatigue performance of the steel overhead DMS support structure with that of an aluminum overhead DMS support structure. Finally, the chapter compares two different cycle counting methods (rainflow method and daily cycle counting method) to estimate fatigue life of the DMS support structure.

Chapter 5 summarizes the main conclusions and offers suggestions for future work.

## **2. Estimation of wind forces acting on traffic signs and members of the trusses supporting these traffic signs**

### **2.1. Problem statement and present state of knowledge**

With increased traffic, multi-lane highways, and complex highway interchanges, highway signs play an important role in safe operation of the nation's transportation network. In the past it was fairly common to see a single large sign supported by a truss structure. The same types of truss structures are now called upon to support a variety of signs of various sizes, aspect ratios, and weights. They include DMS cabinets that are typically much heavier, and have different depths and aspect ratios than typical highway signs. As a result, state agencies tasked with design and construction of highway signs use a variety of ad-hoc procedures that include arbitrary limits on the number and sizes of signs that can be placed on a given truss.

A first requirement to properly design the sign support structures is to accurately estimate mean (time-averaged) wind loads on the highway signs and the members of their support structure. For this, one needs to provide the correct mean value of the drag coefficient for the sign panel and the members of supporting trusses. In particular, the present study focuses on estimating the drag coefficients for DMS cabinets. The truss members may also be subject to fairly significant direct wind loads. Accurate determination of these wind loads requires being able to provide estimates of the drag coefficients for different members of the truss. This is not an easy task given that some of these members are situated in regions where the 'incoming' air flow velocity is very different from that of the approaching wind velocity away from the support structure. The current procedures to estimate wind loads on the members of the supporting structures are based on many simplifying assumptions and are not straightforward to apply for practical cases (e.g., as described in NCHRP Project 17-10(2), NCHRP Report 494, Fouad et al., 2002). For example, these procedures neglect that the air speed is greater than the approaching wind velocity for the unshielded members situated in the vicinity of the sign panel due to the air flow acceleration as it passes the sign. This results in an underestimation of the drag coefficient for such members.

An additional phenomenon that is often overlooked during design is the effect of unsteady oscillations on the signs and on their support trusses (see also Iowa DOT TR-612 study). It is well known that structural supports for traffic signs can exhibit large-amplitude vibrations under wind excitation (Texas DOT RiP Project 27756). These oscillations develop even under steady wind conditions due to the unsteady vortex shedding which takes place in the air wake of the flow past the signs. A resonance condition (galloping effect), causing large amplitude relatively steady vibrations of the support trusses can occur if the frequency of shedding coincides with a natural vibration frequency of the traffic sign. Vortex-shedding can occur at relatively low wind speeds and thus, even if the structure has enough strength, such large oscillations may contribute to stress cycles which can lead to the development of fatigue cracks at the weld toes of truss members supporting heavy

traffic signs. This is because the dominant shedding frequency past obstacles similar to large traffic signs is approximately proportional to the approaching speed. Currently, AASHTO 2015 does not contain any recommendations on how to estimate these variables characterizing the level of unsteadiness of the wind loads on the traffic sign. To conduct a correct structural analysis of the truss supporting the traffic sign, one needs data not only on the mean pressure drag force, but also on the dominant frequencies and amplitude/energy of the unsteady pressure force oscillations cause by vortex shedding.

Most of the current guidelines for wind design of highway structures are based on wind tunnel studies with some limited field investigation. The wind tunnel studies provide valuable insight but, besides being expensive, they have obvious limitations because of the differences between the laboratory and field conditions. In the past there was essentially no other alternative. However recent advances in computational fluid dynamics (CFD) have made tools available that allow realistic fully three-dimensional simulations of actual field conditions at a fraction of the cost of wind tunnel studies. For example, Constantinescu et al. (2007, 2008) used steady 3-D RANS simulations with an advanced  $k-\omega$  shear stress transport (SST) turbulence model ( $k$  determines the energy in the turbulence and  $\omega$  determines the scale of turbulence) to determine drag coefficients of rectangular thin signs and DMS cabinets. Even more accurate estimations of the mean drag coefficient on traffic signs can be obtained using time accurate simulations that resolve the large scale turbulence in the airflow around the traffic sign (Rodi et al., 2013). Such time accurate simulations also have the advantage that they capture the time variations of the drag coefficient associated with the presence of turbulent eddies and in particular with the vortex shedding behind the traffic sign. This is the approach adopted in the present study to determine the temporal and mean values of the drag coefficient for traffic signs. This information is needed to perform structural analyses to investigate if vibrations induced by vortex shedding behind the sign can be a main contributor to fatigue failure. The computational approach is explained in Section 2.3.

## 2.2 Literature review

There is substantial evidence that the present AASHTO 2015 standard underestimates the recommended values of the drag coefficient by a rather significant margin. This situation is not limited to rectangular thin signs. Similar underestimation of the drag coefficients is reported for other type of structures. For example, FHWA/TX-90 (1990) sponsored by the Texas State Department of Highways and Public Transportation found that drag coefficient values for octagonal shape luminaire supports were about 25% higher than the ones currently specified in the corresponding AASHTO standard. Meanwhile, the ASCE/SEI 7-10 recommendations for the design of aluminum sign structures recommend the use of even higher values (1.7-1.8). For the same cases, the drag coefficient calculated based on the AASHTO standard ranges between 1.14 and 1.19, which appears to be too low. In fact, the Illinois DOT-FHWA Research Report 153 (2006) recommended that Illinois DOT use larger drag coefficients than specified by AASHTO for thin sign panels on support trusses.

The study of Letchford (2001) is also very relevant because it provides a systematic analysis of the variation of the drag coefficient on rectangular thin signs placed in an incoming turbulent boundary layer with the sign aspect ratio, ground clearance ratio, angle

of attack of the incoming wind relative to the plate, and porosity. The study found that the drag coefficient increases for smaller ground clearance ratios (i.e., bigger gap between the ground and the sign), while decreases for bigger clearance ratios (i.e., smaller gaps). Other relevant wind tunnel studies for rectangular thin plates of finite width were conducted by Sakamoto and Arie (1983). In another series of wind tunnel experiments, Zuo et al. (2012) not only considered single-plate rectangular signs, but also back-to-back rectangular signs with parallel and non-parallel (V-shaped) faces and box signs of a given thickness. The later configuration is directly relevant for DMS cabinets. Their study found that drag coefficients for box signs were about 10% lower than those on a thin rectangular sign with the same cross-section. A main conclusion of their study was that the geometric configuration of the signs has significant influence on the loading on the structure, which means that sophisticated experimental and/or numerical studies are required to accurately determine the drag coefficient as a function of the main geometric parameters for each type of sign. Single and back-to-back rectangular (billboard) panels with parallel and non-parallel faces were also analyzed via wind-tunnel experiments by Warnitchai et al. (2009). Their study determined the drag coefficient variation as a function of the panel aspect ratio, ground clearance ratio and incoming wind angle of attack. They found that the drag coefficient is about constant for angles of attack of less than  $40^\circ$  before starting to monotonically decay with increasing angle of attack. Full-scale experimental studies to determine drag coefficient for rectangular, finite-width obstructions appear to be available only for the case when the obstruction is attached to the ground (free-standing walls perpendicular to the ground).

Current AASHTO procedures to determine drag forces on the members of the support structures (e.g., cylindrical truss members) are based on the assumption that the drag coefficient of the unshielded member is that of a long cylinder placed in an incoming uniform flow. All interactions with the boundaries and neighboring members are neglected and the flow past the isolated cylinder is assumed to be in the quadratic-drag regime. Typical values of the drag coefficient are close to 1.2. The drag coefficient of the shielded cylinders are assumed to be negligible. Existing methodologies like the one described in NCHRP Project 17-10(2) propose a set of rules to help decide when a member of a support truss structure can be considered to be shielded. These methodologies make many simplifying assumptions.

Martin et al. (1987) were among the first to take into consideration the possibility of resonance due to vortex shedding in the wake of highway signs mounted on supports. They compared field measurements with analytical results, including the possibility of resonance due to cyclic loads induced by vortex shedding. Analytical studies predicted resonance tendencies at several lower wind speeds. Resonance behavior was not observed due to the inherent damping of the structures (monotube highway sign supports) used in their field test. However, this is highly probable for other types of support sign structures.

### 2.3. Numerical methodology used to estimate wind loads and drag coefficients

Most predictions of engineering flows are obtained using the so-called RANS approach in which the effect of most of the scales (eddies, vortices, etc.) on the mean flow is accounted via a RANS turbulence model. RANS simulations were successfully used in the past to estimate time averaged wind loads on traffic signs (Constantinescu et al., 2007, 2008). This approach is used in the present study for the more complex cases when the truss is part of the computational domain and the pressure distribution is used to calculate the drag forces on all individual members of the truss.

Given that a major objective of the present study is to accurately capture the mean pressure force and also to obtain the main frequency of the unsteady drag force oscillations, a more accurate numerical approach is used in computations of flow past isolated DMS cabinets or past thin traffic signs situated at a certain distance from the ground. DES calculations are used for such cases. DES is a non-zonal technique that can be applied at high Reynolds numbers as can RANS models, but also resolves the dynamically important large scale turbulent eddies similar to large eddy simulation (LES). In particular, DES was shown to successfully capture the vortex shedding past bluff bodies (Rodi et al., 2013), which is essential for this part of the present study. DES reduces to RANS close to solid boundaries and to a Smagorinsky-type subgrid-scale model away from the solid boundaries (Spalart 2009). There is no artificial transition between the RANS and LES regions, which is a major advantage of this approach compared to classical zonal models. Compared to time accurate RANS, DES is computationally more expensive as the time step is generally smaller compared to unsteady RANS of the same flow and the grid in some regions of the computational domain needs to be refined to accurately capture the dynamically important eddies in the flow. However the overall increase is generally less than one order of magnitude (Rodi et al., 2013).

The steady RANS and time-accurate DES numerical simulations were performed using STARCCM+, a commercial CFD software developed by CD-Adapco for modeling fluid flow and heat transfer in complex geometries. STAR-CCM+ can use a wide range of turbulence models with both wall functions and near-wall treatment to simulate turbulent flows. STAR-CCM+ contains a very powerful meshing capability in which an initial geometry can be imported, smoothed in such a way to improve computational efficiency and to obtain better results without loss of information. Once the geometry has been processed, a volume mesh is created with the desired meshing model in order to obtain a mesh which is acceptable to STAR-CCM+ requirements. Some meshing models include tetrahedral, hexahedral and polyhedral models with mesh refinement near boundaries. Additional refinement can be included near boundaries by producing high-aspect ratio, highly skewed cells named prism layers.

The governing Navier-Stokes equations are:

$$\frac{\partial}{\partial x_i}(\rho u_i) = 0$$

$$\frac{\partial}{\partial t}(\rho u_i) + \frac{\partial}{\partial x_i}(\rho u_i u_k) = -\frac{\partial p}{\partial x_i} + \frac{\partial}{\partial x_j} \left[ (\mu + \mu_t) \left( \frac{\partial u_i}{\partial x_j} + \frac{\partial u_j}{\partial x_i} \right) \right] \quad (2.1)$$

where  $u_i$  is the Cartesian velocity component along the  $i$  direction,  $p$  is the pressure,  $\rho$  is the density and  $\mu$  and  $\mu_t$  are the dynamic and turbulent viscosity, respectively.

The steady RANS simulations were conducted using the two-layer  $k$ - $\varepsilon$  model. The two-layer  $k$ - $\varepsilon$  turbulence model ( $k$  is the turbulence kinetic energy and  $\varepsilon$  is the turbulent dissipation rate) is used to estimate the eddy viscosity in equation (2.1):

$$\mu_T = \rho C_\mu \frac{k^2}{\varepsilon} \quad (2.2)$$

The transport equations used to calculate  $k$  and  $\varepsilon$  are:

$$\begin{aligned} \frac{\partial}{\partial t}(k) + \frac{\partial}{\partial x_i}(u_i k) &= \frac{\partial}{\partial x_j} \left[ \frac{1}{\rho} (\mu + \frac{\mu_t}{\sigma_k}) \left( \frac{\partial k}{\partial x_j} \right) \right] + G - \varepsilon \\ \frac{\partial}{\partial t}(\varepsilon) + \frac{\partial}{\partial x_i}(u_i \varepsilon) &= \frac{\partial}{\partial x_j} \left[ \frac{1}{\rho} (\mu + \frac{\mu_t}{\sigma_\varepsilon}) \left( \frac{\partial \varepsilon}{\partial x_j} \right) \right] + C_{\varepsilon 1} \frac{\varepsilon}{k} - C_{\varepsilon 2} \frac{\varepsilon^2}{k} \end{aligned} \quad (2.3)$$

where  $G$  is the turbulence production term and the model coefficients have the following values:

$$\sigma_k = 1.0 \quad \sigma_\varepsilon = 1.3 \quad C_{\varepsilon 1} = 1.44 \quad C_{\varepsilon 2} = 1.92 \quad C_\mu = 0.09 \quad (2.4)$$

The mesh was sufficiently fine to resolve the flow within the viscous sublayer. The flow domain is divided into two regions: an inner layer where a one-equation turbulence model is used and an outer layer where the above (high-Reynolds-number) version of the  $k$ - $\varepsilon$  model is used. The inner-layer model solves only the  $k$ -equation while the  $\varepsilon$  equation is replaced by

$$\varepsilon = \frac{k^{3/2}}{l_\varepsilon} \quad (2.5)$$

The eddy viscosity is obtained from

$$\mu_T = \rho C_\mu \sqrt{k} l_\mu \quad (2.6)$$

instead of equation (2.2). Here  $l_\varepsilon$  and  $l_\mu$  are length scales which are a function of the turbulence Reynolds number,  $R_T = \frac{\sqrt{k} n}{\nu}$ . Their expressions are:

$$\begin{aligned}
l_\mu &= C_1 n \left[ 1 - \exp\left(-\frac{R_T}{A_\mu}\right) \right] \\
l_\varepsilon &= C_1 n \left[ 1 - \exp\left(-\frac{R_T}{A_\varepsilon}\right) \right]
\end{aligned} \tag{2.7}$$

where  $n$  is the normal distance from the (nearest) wall,  $C_1 = \kappa C_\mu^{-3/4}$  so as to obtain a smooth eddy-viscosity distribution between the inner and the outer layers,  $\kappa = 0.42$  is the von Karman constant,  $A_\varepsilon = 2C_1$  and  $A_\mu = 70$ . Besides its robustness, an advantage of the two-layer model is that it does not require a boundary condition for  $\varepsilon$  at the wall.

For DES simulations, the eddy viscosity in equation (2.1) is obtained using a modified version of the Spalart-Allmaras (SA) RANS model. The SA linear, eddy-viscosity model is based on a transport equation for the modified eddy viscosity  $\tilde{\nu}$  (Spalart 2009, Rodi et al., 2013). The model incorporates the distance to the nearest wall,  $d$ , as the turbulence length scale. The transport equation for  $\tilde{\nu}$  is:

$$\frac{\partial \tilde{\nu}}{\partial t} + V^j \frac{\partial \tilde{\nu}}{\partial \xi^j} = c_{b1} \tilde{S} \tilde{\nu} + \frac{1}{\sigma} \left[ \nabla \cdot ((\nu + \tilde{\nu}) \nabla \tilde{\nu}) + c_{b2} (\nabla \tilde{\nu})^2 \right] - c_{w1} f_w \left[ \frac{\tilde{\nu}}{d} \right]^2 \tag{2.8}$$

where  $S$  is the magnitude of the vorticity vector. The other variables are:

$$\begin{aligned}
\tilde{S} &\equiv S + (\tilde{\nu}/\kappa^2 d^2) f_{v2} \\
f_{v2} &= 1 - \tilde{\nu}/(\nu + \tilde{\nu} f_{v1}) \\
f_{v1} &= \chi^3 / (\chi^3 + C_{v1}^3) \\
\chi &= \frac{\tilde{\nu}}{\nu} + 0.5 \frac{\kappa_s}{d} \\
f_w &= g \left[ \frac{1 + C_{w3}^6}{g^6 + C_{w3}^6} \right]^{1/6} \\
g &= r + C_{w2} (r^6 - r) \\
r &\equiv \frac{\tilde{\nu}}{S \kappa^2 d^2}
\end{aligned}$$

The molecular eddy viscosity  $\nu_t$  is obtained from  $\nu_t = \tilde{\nu} f_{v1}$ . Finally,  $\mu_t = \rho \nu_t$  is used in equation (2.1). The model constants in the above equations are  $C_{b1} = 0.135$ ,  $C_{b2} = 0.622$ ,  $\sigma = 0.67$ ,  $\kappa = 0.41$ ,  $C_{v1} = 7.1$ ,  $C_{w2} = 0.3$ ,  $C_{w3} = 2.0$  and  $C_{w1} = C_{b1}/\kappa^2 + (1 + C_{b2})/\sigma$ .

DES is based on a modification of the length scale in the destruction term of the transport equation for the modified eddy viscosity in the SA RANS model. The SA version of DES is obtained by replacing the turbulence length scale  $d$  (distance to the nearest wall) in the destruction (dissipation-like) term of the transport equation for  $\tilde{\nu}$  with a new length scale  $d_{DES} = \min(d, C_{DES} \Delta)$ , where the model parameter  $C_{DES}$  is equal to 0.65 and  $\Delta$  is a measure of the local grid size. When the production and destruction terms in the transport equation for  $\tilde{\nu}$  (equation 2.8) are balanced, the length scale in the LES regions  $d_{DES} = C_{DES} \Delta$  becomes proportional to the local grid size and yields an eddy viscosity proportional to the mean rate of strain and  $\Delta^2$  as in LES with a Smagorinsky model (Rodi et al., 2013). The

redefined length scale away from the solid boundaries increases the magnitude of the destruction term in the SA model. This method allows a cascade of energy down to grid size. The governing equations are integrated through the viscous sub-layer and no wall functions are used. Additional discussion of the model and implementation details can be found in Spalart (2009) and Rodi et al. (2013).

The parallel pressure-based Navier-Stokes solver in STARCCM+ was employed to conduct the simulations. The RANS equations are solved based on a finite volume representation. The advective terms are discretised using a second-order accurate in space upwinding scheme, while the transient term was second-order accurate based on an implicit representation. The diffusive term is discretised using a second-order central difference scheme. The pressure gradient term is discretised using a second order accurate central difference scheme. The pressure-coupling algorithm chosen was the SIMPLE algorithm. In the SIMPLE algorithm, the RANS equations are solved and an intermediate velocity is obtained which does not satisfy the continuity or mass conservation equation. A pressure correction algorithm is employed to modify the pressure field and in turn modify the mass fluxes and velocity fields in order to satisfy mass conservation.

A pressure outlet boundary was used at the exit section in all simulations. The lateral boundaries were placed at a large distance from the panel and symmetry boundary conditions were used. The traffic sign/DMS cabinet surfaces were treated as no slip surfaces. The flow in the stream-wise direction was fully-developed in the inflow section that was placed at a considerable distance upstream of the traffic sign such that the distance between the inflow and the sign does not affect the predicted flow field around the sign and the wind forces acting on the sign. The velocity and the profiles of the turbulence quantities in the inflow section were obtained from preliminary RANS or DES simulations. In the simulations in which the ground surface was present, a no-slip wall-surface boundary was used at the bottom of the computational domain. The same was true for the surface of the truss members in the RANS simulation containing the truss and the DMS cabinet. Grid dependency studies were conducted to insure that the level of mesh refinement is sufficient so that the predicted values of the main flow variables (e.g., mean drag force on the traffic sign) are independent of the grid. In the case of DES simulations, the mean value of the different variable is obtained by time-averaging the instantaneous flow fields over a sufficient time interval after the solution became statistically steady. Statistics were checked for convergence.

#### **2.4. Validation: Flow past a wide thin plate with perpendicular incoming wind**

Several preliminary simulations were performed for air flow past isolated, infinitively wide thin plates placed perpendicular to the wind direction. This was needed because RANS and DES simulations showed that the drag coefficient is a function of the flow blockage due to the presence of the plate (traffic sign). Moreover, this is the only test case for which very reliable experimental predictions of the drag coefficient  $C_d$  are available.

The height of the computational domain was increased gradually in the RANS and DES simulations until the value of  $C_d$  became independent of the height of the computational

domain. That happened when the height of the computational domain was about  $16s$ , or equivalently the blockage ratio became less than 0.06. RANS and DES simulations conducted with a plate of height  $s=2.5\text{ m}=8.2\text{ ft}$  and  $U=40\text{ m/s}=131.2\text{ ft/s}$  predicted  $C_d=2.67$  and  $C_d=1.99$ , respectively. The thickness of the plate was  $0.003h$ . For high Reynolds number flows ( $Re=Us/\nu>10^4$ , where  $U$  is the mean incoming flow/wind velocity,  $s$  is the height of the plate and  $\nu$  is the molecular viscosity), the experimentally determined value of  $C_d$  is close to 2.0. One can see that the mean DES solution predicts a value of  $C_d$  very close to the mean experimental value, while RANS prediction overestimates  $C_d$  by about 30%. This gives confidence in the accuracy of DES predictions of wind loads for flow past traffic signs.

Another important thing to check is that  $C_d$  becomes independent of the Reynolds number for sufficiently large Reynolds numbers. To investigate if the numerical solution can correctly capture this behavior, a second simulation was conducted in a domain of larger height  $s=5.8\text{ m}=26.24\text{ ft}$ . The incoming wind velocity was kept constant. The predicted values of the drag coefficient given by the new RANS ( $C_d=2.68$ ) and DES ( $C_d=2.02$ ) were very close to the values predicted in the simulation with  $s=2.5\text{ m}=8.2\text{ ft}$ .

Additional RANS simulations were performed with the  $k-\omega$  SST model. The  $C_d$  values predicted by the SST model were very close to the ones predicted by the 2-layer  $k-\epsilon$  model. All the other simulations conducted as part of the present study were conducted using the former RANS model.

In the case where the sign is of finite width and placed at a certain distance from the ground, the main geometrical length scales are the sign width,  $B$ , the sign height  $s$  and the distance between the ground and the top of the sign called the ground clearance height,  $h$  (see also sketch in Fig. 2.1). Based on the results obtained in this subsection, all the RANS and DES simulations of flow past traffic signs positioned at a certain distance above the ground were conducted in a computational domain whose top boundary was placed at least  $8s$  above the top of the traffic sign. This insured the drag force predictions are independent of the size of the computational domain for this type of configurations.

## **2.5. Estimation of drag coefficient for an isolated DMS cabinet with varying incoming wind direction**

A series of five DES simulations was performed for airflow past the DMS cabinet in the presence of the ground for different wind directions (90 degrees to 30 degrees). These simulations are labelled  $a1$  to  $a5$  in Table 1 and were performed with a DMS cabinet (Case  $a$  configuration) of the dimensions shown in Fig. 2.2. The DMS cabinet was situated at a given height above the ground ( $h=5.18\text{ m}=17\text{ ft}$ ). The dimensions of the DMS cabinet for Case  $a$  configuration were  $B=9\text{ m}=29.25\text{ ft}$ ,  $s=2.5\text{ m}=7.833\text{ ft}$ . The simulations took into account the fact that one of the faces of the DMS cabinet was slightly tapered with respect to the vertical (frontal face is slightly inclined toward traffic as shown in Fig. 2.2). The wind speed was 90 mph (40.2 m/s) in all five cases. The only parameter that was varied was the free stream wind direction in the horizontal plane. The length of the computational domain was about 120 m (393.7 ft) and its height was close to 25 m (82 ft). The center of

the DMS cabinet was situated at a distance of about 26 m (85 ft) from the inlet. A mesh with close to 5 million cells was used. The mesh was refined near all no-slip surfaces (ground, faces of the DMS cabinet) and in the wake of the DMS cabinet to resolve the energetic turbulent eddies in the separated shear layer, the wake and the attached boundary layers.

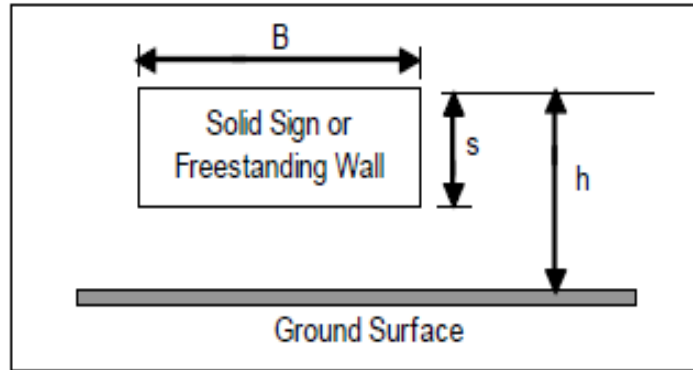


Figure 2.1 Sketch showing the main relevant length scale for a traffic sign placed above the ground surface. Reproduced from Foutch et al. (2006).

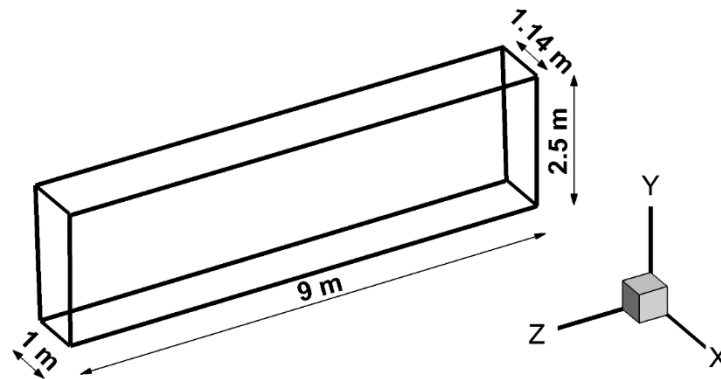


Figure 2.2 Sketch showing main dimensions of DMS cabinet for Case *a*

Table 2.1 summarizes calculated values of the mean drag coefficient and its root mean square fluctuations. The inclination angle denotes the angle between the wind direction and the normal direction to the face of the DMS cabinet. A zero inclination angle (Case *a1*) corresponds to the case when the wind direction is perpendicular to the DMS cabinet. As expected, there is a monotonic decrease in the values of  $C_d$  with increasing inclination angle. This decrease is mainly due to the fact that the incoming airflow is deflected in a milder way with increasing inclination angle. This decreases the pressure induced on the upwind side of the traffic sign.

An additional simulation was performed for a larger DMS cabinet with  $B=12.2$  m=40 ft and  $h=2.6$  m=8.5 ft (Case *b* configuration in Table 2.1) for a zero inclination angle to investigate the dependence of  $C_d$  with the size of the DMS cabinet. The floor clearance ratio was the same as that for the Case *a1* simulations. Comparison of Cases *a1* and *b* in

Table 2.1 shows that the drag coefficient for the larger DMS cabinet ( $C_d=1.37$ ) is larger than the one for the smaller cabinet ( $C_d=1.30$ ) but the difference is only about 5%.

Figure 2.3 shows the time histories of the drag coefficient obtained from the six simulations. As expected, the turbulence and in particular the large scale vortex shedding induce low and high frequency oscillations of the drag coefficient. The amplitude of the low frequency oscillations decreases with increasing inclination angle. At higher inclination angles, it is the higher frequency oscillations that are the most energetic, which may signify the large scale vortex shedding is very weak or absent. This is expected given that at high inclination angles, the degree of bluntness of the obstacle (DMS cabinet) is very much reduced. The strength of these oscillations can be characterized in a more quantitative way by calculating the root-mean square (rms) of the mean drag coefficient fluctuations. These values are also given in Table 2.1. Even for a zero inclination angle, where energetic low frequency oscillations are present, the maximum and minimum values of  $C_d$  are within 5% of the mean value. So, in terms of the value used for design, one can safely use the mean value of the drag coefficient or 1.05 times that value. The time series of  $C_d$  in Fig. 2.3 contain the information required to perform a dynamic structural analysis. The dominant frequencies and their energy can readily be extracted from the time series and used as input for structural analysis.

Table 2.1 Variation of the mean drag coefficient and of the rms of the drag coefficient fluctuations for a DMS cabinet placed above the ground. Also given in the Table are the dimensions of the DMS cabinet and the inclination angle.

Case	Dimensions (Bxs)	Inclination angle	$C_d$	rms $C_d$
<i>a1</i>		0 <sup>0</sup>	1.30	0.026
<i>a2</i>		15 <sup>0</sup>	1.26	0.022
<i>a3</i>	9mx2.5m	30 <sup>0</sup>	1.22	0.021
<i>a4</i>		45 <sup>0</sup>	1.10	0.016
<i>a5</i>		60 <sup>0</sup>	0.81	0.007
<i>b</i>	12.2mx2.6m	0 <sup>0</sup>	1.37	0.022

It is also relevant to mention that RANS simulations of Cases *a1* and *b* also predicted values of  $C_d$  higher by about 20% compared to the corresponding DES simulations. This result is consistent with that obtained for infinitely wide plates ( $B/s \gg 1$ ). However, RANS underestimates  $C_d$  compared to DES in the cases with a high inclination angle. Another very important observation is that the present results show that the drag coefficient of finite aspect ratio signs is less than that of infinitely wide signs of same height and same clearance

height (see results in Section 2.4). The effect of decreasing the aspect ratio on  $C_d$  will further be investigated in Section 2.7.0.

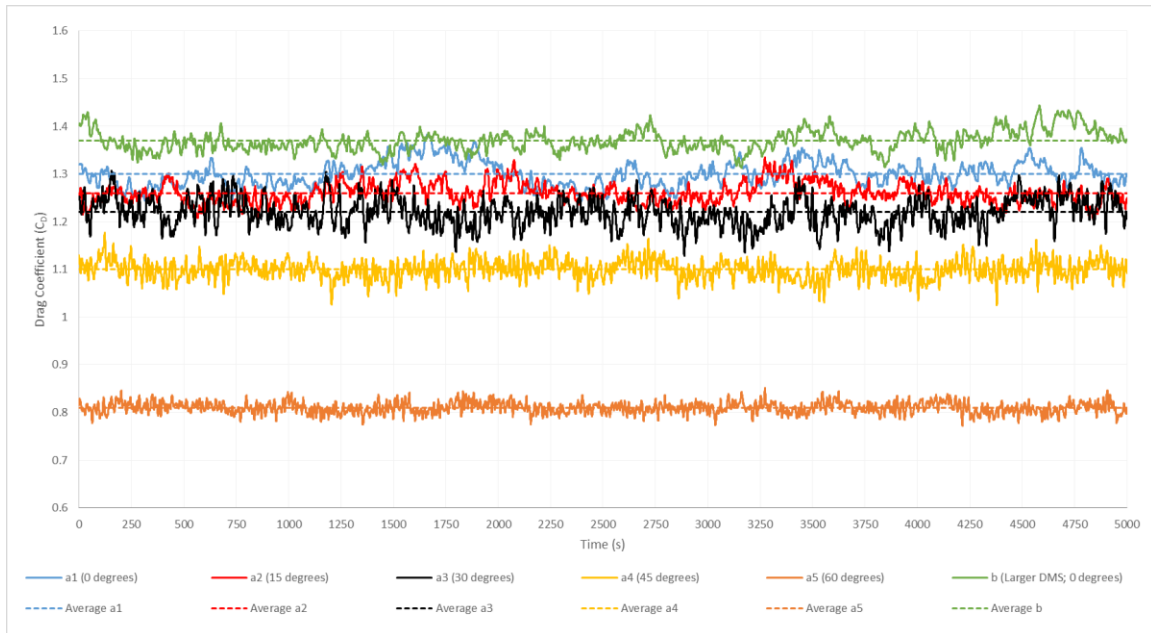


Figure 2.3 Time history of the drag coefficient predicted by the DES simulations for the Case *a* and Case *b* DMS configurations. Also shown are the mean values of  $C_d$ .

Given that these estimations of the drag coefficient were obtained from DES simulations, it is relevant to discuss some main features observed in the mean and instantaneous flow fields. In the interest of brevity only the solution for Case *a1* with an inclination angle of  $0^\circ$  is analyzed. Figure 2.4 shows the mean flow in a stream-wise vertical section cutting the DMS cabinet at mid width. This section is a symmetry plane for this case. As expected the flow is accelerated on the sides of the DMS cabinet, a recirculation region of negative streamwise velocity containing two bubbles forms at the back of the DMS cabinet and the pressure increases sharply on the upstream face of the DMS cabinet (see streamwise velocity and pressure contours plot in Fig. 2.4). Due to the mean streamwise velocity gradient between the accelerated flow passing the DMS cabinet and the slowly moving flow inside the recirculation bubble at the back of the DMS cabinet, strong separated shear layers develop on the two sides of the DMS cabinet, as observed in the span-wise vorticity contour plot in Fig. 2.4. The presence of the ground surface does not induce large asymmetries in the distributions of the vorticity and stream-wise velocity on the two sides of the DMS cabinet. That would not be the case if the clearance distance between the ground and the DMS cabinet would be reduced significantly. The eddy diffusivity distribution in Fig. 2.4 shows a large amplification in the region where the separated shear layers interact and wake billows. As expected, the eddy diffusivity is also amplified on the attached boundary layer forming on the ground surface.

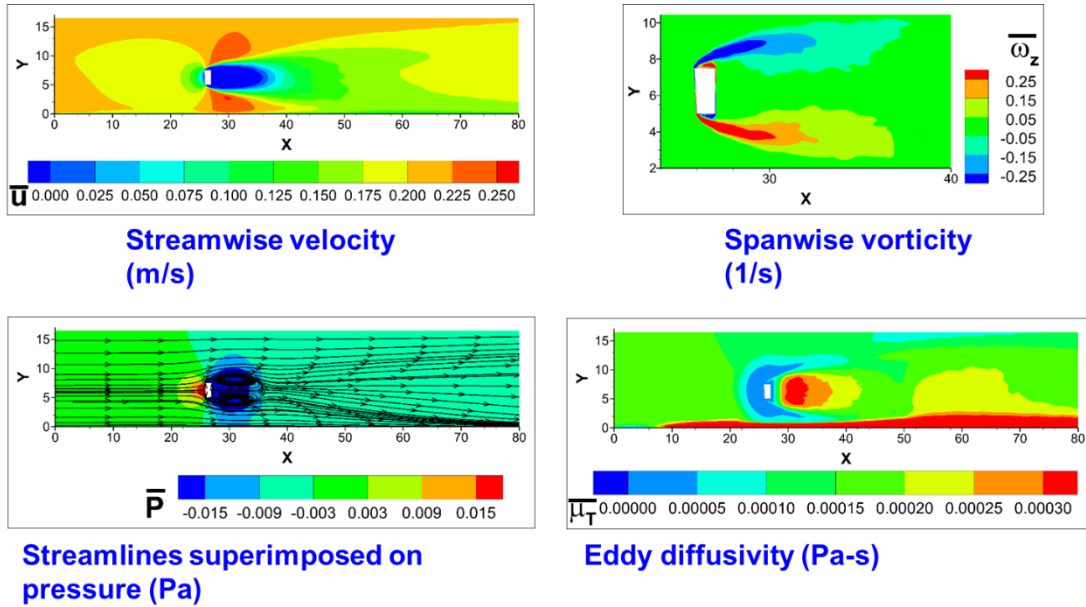


Figure 2.4 Visualization of the mean flow (Case *a1*) in the  $z=13.5$  m=44.3 ft streamwise vertical section cutting the DMS cabinet at mid width. The four frames show the streamwise velocity, spanwise vorticity, pressure and eddy diffusivity.

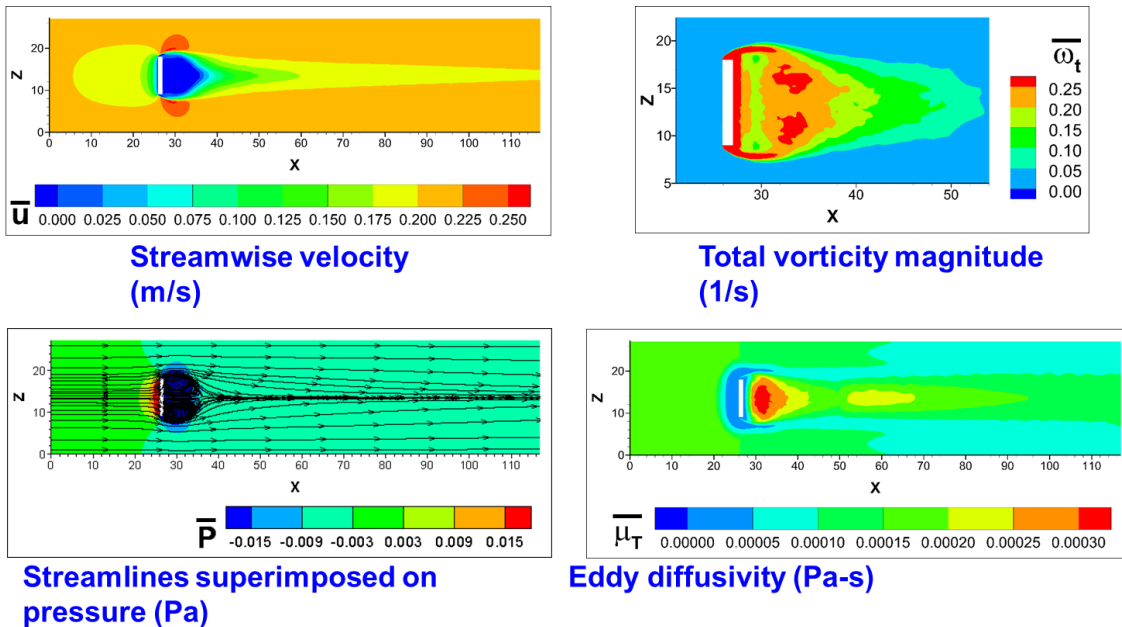


Figure 2.5 Visualization of the mean flow (Case *a1*) in the  $y=6.25$  m=20.5 ft spanwise vertical section cutting the DMS cabinet at mid height. The four frames show the streamwise velocity, spanwise vorticity, pressure and eddy diffusivity.

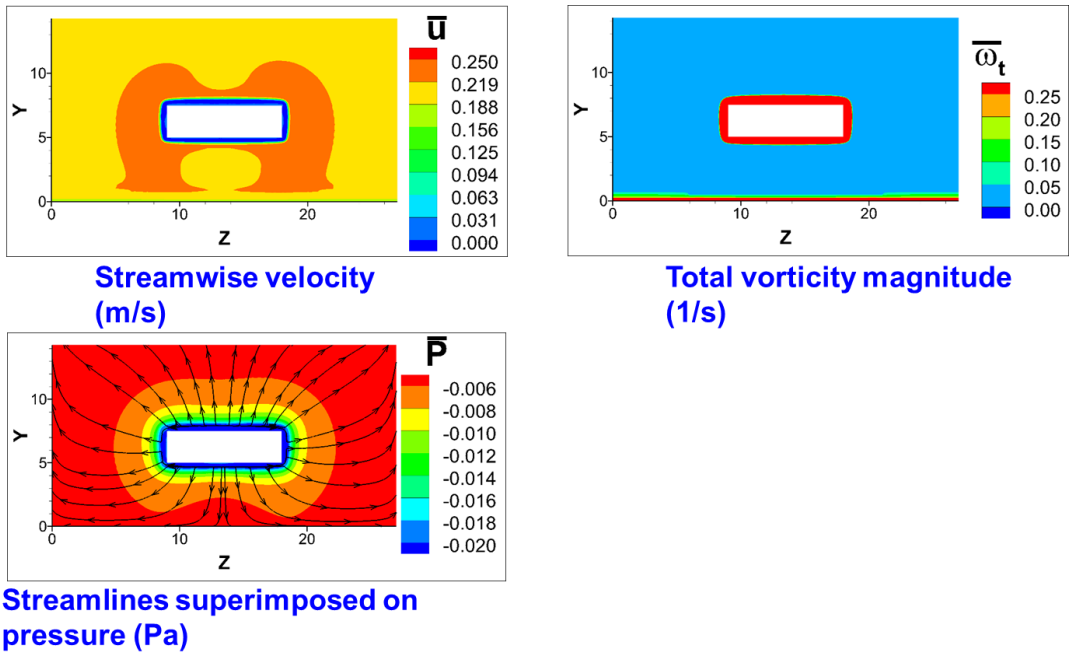


Figure 2.6 Visualization of the mean flow (Case *a1*) in the  $x=26.5$   $m=87$  ft cross-flow section cutting the DMS cabinet at mid thickness. The three frames show the streamwise velocity, spanwise vorticity and pressure.

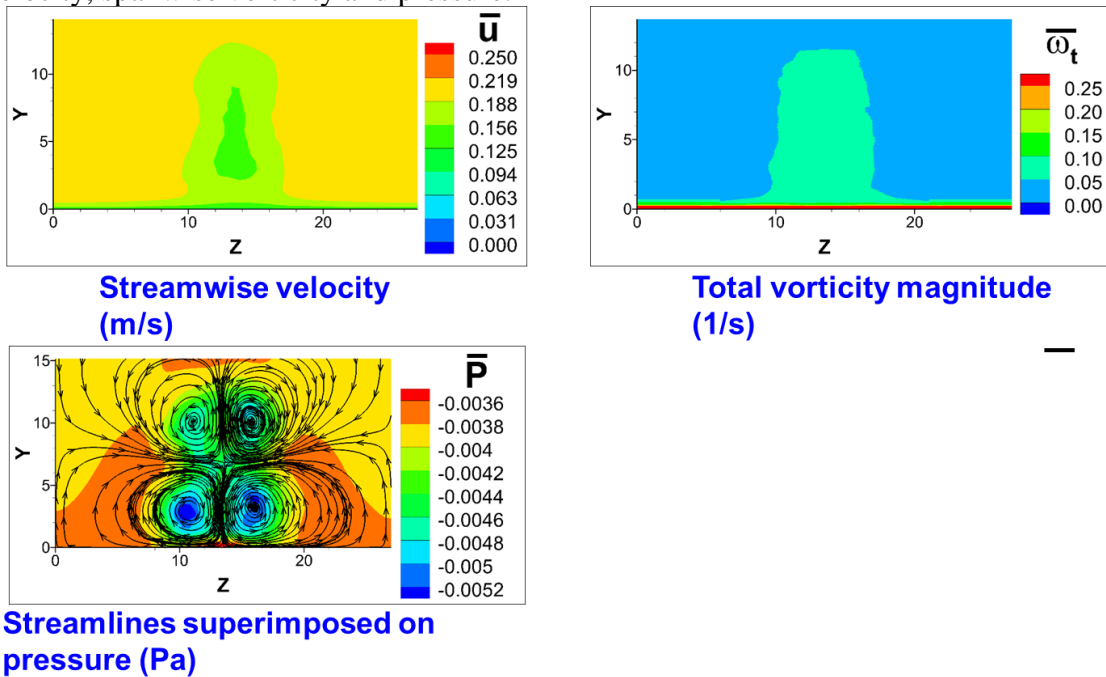


Figure 2.7 Visualization of the mean flow (Case *a1*) in the  $x=50$   $m=164$  ft cross-flow section cutting the wake of the DMS cabinet. The three frames show the streamwise velocity, spanwise vorticity and pressure.

Figure 2.5 visualizes the mean flow solution in a horizontal plane cutting the DMS cabinet at mid height. The mean solution is symmetrical with respect to the middle of the DMS cabinet. The main features of the solution are qualitatively similar to those observed in the

vertical symmetry plane in Fig. 2.4. Two bubbles are also observed inside the recirculation region at the back of the DMS cabinet in the horizontal plane solution. The total vorticity magnitude contours in Fig. 2.5 show that the separated shear layers are shorter in the horizontal symmetry plane. The high values of the total vorticity magnitude in the near wake are due to vorticity associated with the shedding of wake billow vortices whose oscillations are primarily taking place along the vertical direction.

Figures 2.7 and 2.8 visualize the solution in vertical planes parallel to the DMS cabinet cutting at mid thickness of the DMS cabinet and through the wake of the DMS cabinet respectively. The solution in the plane cutting through the DMS cabinet basically shows the attached boundary layers forming on the four lateral faces of the DMS cabinet and on the ground surface. More interestingly, it shows the shape of the region where the flow accelerates as it passes the DMS. Notice the asymmetry of the shape of this region above and below the DMS cabinet (stream-wise velocity contour plot in Fig. 2.6) which is due to the presence of the ground surface. As expected the secondary flow shows that flow particles are diverted away from the DMS cabinet in this plane. This is simply due to the lateral velocity component acquires by the incoming flow toward the upstream face of the DMS cabinet as it passes the DMS cabinet.

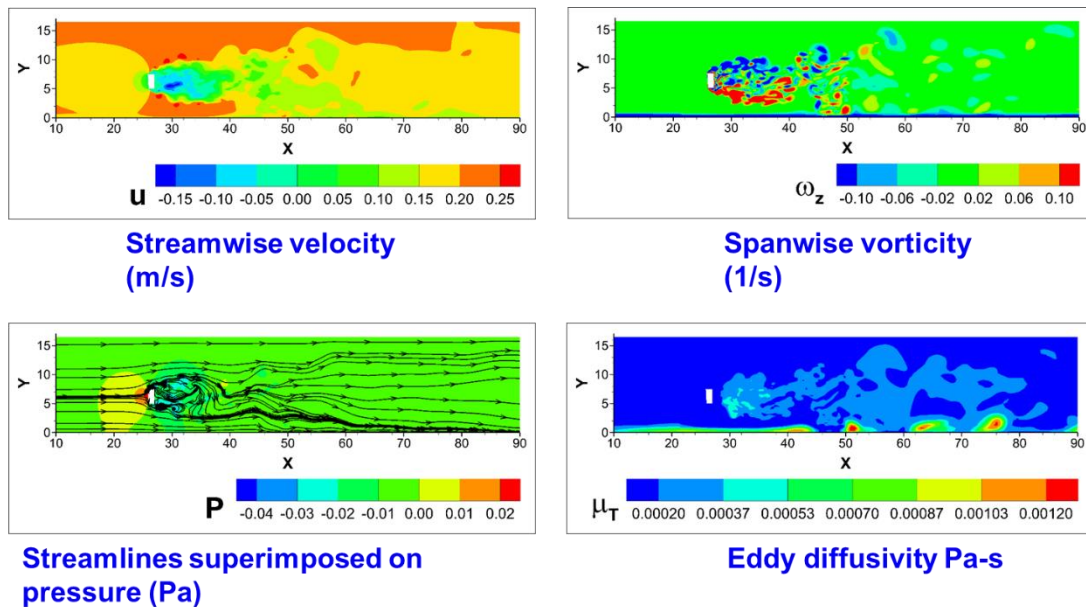


Figure 2.8 Visualization of the instantaneous flow (Case *a1*) in the  $z=13.5$  m= $44.3$  ft streamwise-vertical section cutting the DMS cabinet at mid width. The four frames show the streamwise velocity, spanwise vorticity, pressure and eddy diffusivity.

Figure 2.8 shows some interesting features of the wake behind a DMS cabinet positioned some distance from the ground. The wake identified as the region of stream-wise velocity deficit and/or high vorticity magnitude has a higher height compared to its width. This may look surprising as the width of the DMS cabinet is much larger than its height (Fig. 2.6). The reason is that the stronger oscillations associated with the separated shear layers and the shedding of wake billows occur in vertical planes. As these wake billows get away from the back of the DMS cabinet they tend to move away from the symmetry axis of the

DMS cabinet. Of course, the lateral movement is constraint on the lower side of the domain by the presence of the ground surface. By contrast, the wake width is comparable to the width of the DMS cabinet (negligible growth). The other interesting feature of the solution in this plane is the formation of four secondary flow vortices. Notice that the reduction of the pressure in the cores of these four vortices is significant. These vortices are symmetrically positions with respect to the center of the downstream face of the DMS cabinet.

As already discusses, the present numerical simulations resolve the large scale turbulence including the formation of Kelvin Helmholtz (KH) vortex tubes in the downstream part of the separated shear layers and the larger-scale wake vortices that result from the interaction of the downstream ends of the separated shear layers and merging of successive KH vortices into a larger wake vortex. Figures 2.8 and 2.9 visualize the instantaneous flow solution in the vertical and horizontal symmetry planes for which the mean flow solution was visualized in Figs. 2.4 and 2.5, respectively. As expected, the velocity and vorticity instantaneous flow fields are not symmetric. Very strong vortex tubes are observed in the separated shear layers in Fig. 2.8, much more coherent (higher vorticity magnitude inside the well-defined cores of these vortices) than the corresponding ones in Fig. 2.9. The region of high vorticity magnitude behind the DMS in Fig. 2.9 has a width comparable to that of the DMS cabinet even at large distance behind the DMS cabinet. This confirms that the growth of the wake in horizontal planes is negligible. By contrast, patches of high vorticity magnitude are observed at large distances away from the symmetry plane of the DMS cabinet in Fig. 2.8. These patches start interacting with the ground surface at around  $x=45$  m=147.6 ft, so the wake penetrates until the ground for  $x>45$  m (147.6 ft). Above the DMS cabinet, the wake height increases with the distance from the DMS cabinet. The interaction of eddies generated in the wake of the DMS cabinet with the bottom boundary layer is visualized in the vorticity and eddy diffusivity contour plots in Fig. 2.8. One can see that the attached boundary layer on the ground is strongly disturbed by these interactions and ejection of patches of vorticity from the ground surface boundary layer occur when eddies from the wake penetrate close to the ground surface. Finally, while the recirculation eddy behind the DMS cabinet is fairly stable and contains two bubbles of comparable dimensions at most times in the horizontal symmetry plane, the flow inside the recirculation eddy is much more irregular in time in the vertical symmetry plane. This is consistent with the fact that the primary antisymmetric shedding takes place in stream-wise vertical planes rather than stream-wise horizontal planes, similar to the case of a very wide obstacle oriented along the span-wise direction. This result is somewhat expected taking into account that the width of the DMS cabinet is couple of times larger than its height. The shedding pattern and the growth of the wake behind the plate can be very different for plates with smaller aspect ratios. The larger-scale (lower-frequency) oscillations of the drag coefficient in Fig. 2.3 are induced by the (antisymmetric) shedding of wake billows in vertical planes. As opposed to the case of very wide plates, these oscillations are less regular mainly because of the effects of the oscillations of lateral separated shear layers on the wake billows and the presence of the ground surface. The higher frequency oscillations are mainly due to the larger scale turbulence inside the separated shear layers (e.g., KH vortex tubes) and the recirculation bubble.

Figure 2.10 visualizes the wake behind the DMS cabinet in a cross-section  $x=50$  m=164 ft, the same in which the mean flow solution was visualized in Fig. 2.7. The four symmetric stream-wise oriented vortices observed in the mean flow are not present in the instantaneous flow solution that contains a wide range of highly 3-D eddies. Some of the strongest eddies in this cross section have their axes oriented along or close to the stream-wise direction. The lateral (spanwise) extent of the region populated by the 3-D eddies is comparable to that occupied by the DMS cabinet.

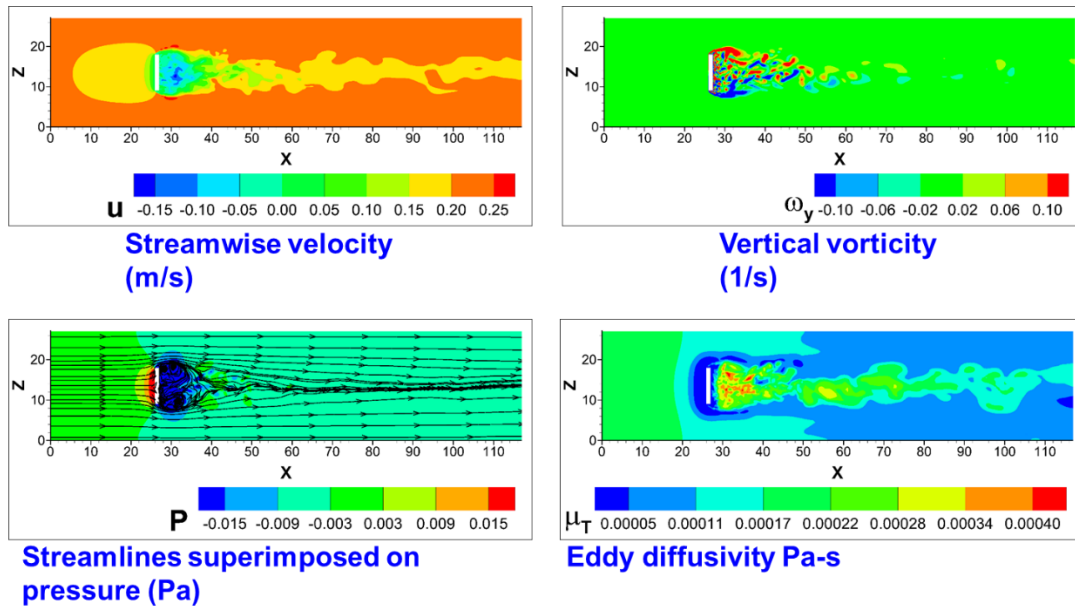


Figure 2.9 Visualization of the instantaneous flow (Case *a1*) in the  $y=6.25$  m=20.5 ft spanwise vertical section cutting the DMS cabinet at mid height. The four frames show the streamwise velocity, spanwise vorticity, pressure and eddy diffusivity.

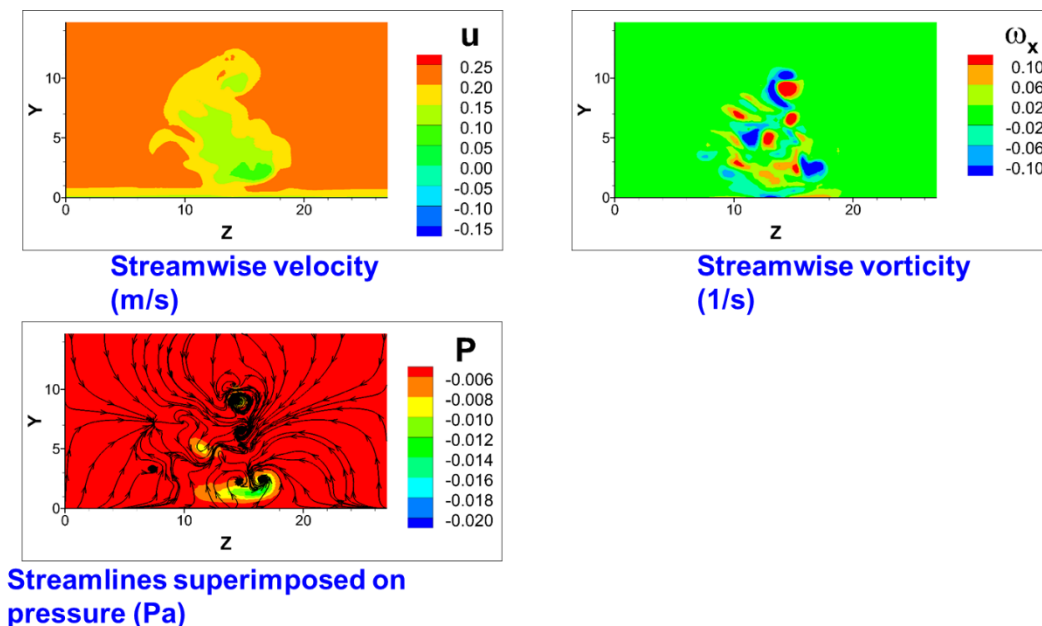


Figure 2.10 Visualization of the instantaneous flow (Case *a1*) in the  $x=50$  m=164 ft cross-flow section cutting the wake of the DMS cabinet. The three frames show the streamwise velocity, spanwise vorticity and pressure.

## 2.6. Estimation of drag coefficient for traffic signs with perpendicular incoming wind

The same type of numerical simulations and analysis was conducted to determine the mean drag coefficient for a series of plates with different geometries. The results are summarized in Table 2.2. In all these simulations the ground clearance distance was kept constant.

Table 2.2 Mean drag coefficient for traffic signs with perpendicular incoming wind

Case	Cd
thin plate a1 (0°, original geometry)	1.28
45' x 10' x 4' (L x H x D) cabinet	1.31
45' x 13' x 4' (L x H x D) cabinet	1.32
50' x 19' x 0.167' (L x H x D) thin plate	1.32
25' x 19' x 0.167' (L x H x D) 2 thin plates 1' gap in between	1.33

The first question is whether or not the thickness of the DMS cabinet has a significant effect on the value of  $C_d$ . To investigate this, an additional simulation was conducted for a thin plate of same vertical and lateral dimensions and ground clearance as the DMS cabinet in Case *a1*. Results in Table 2.2 show that the drag coefficient for the thin plate case ( $C_d=1.28$ ) is only slightly smaller than the value predicted for the DMS cabinet ( $C_d=1.3$ , see Table 2.1).

Simulations were also conducted for DMS cabinets of different sizes and in particular of different heights. Results in Table 2.2 show that there is a negligible increase in the drag coefficient with increasing height of the DMS cabinet. But in all cases the predicted values of  $C_d$  were between 1.3 and 1.32.

Finally, simulations were conducted for 2 thin plates positioned side by side with a small gap of one foot in between them. The purpose of this simulation was to check if the gap between the thin plates has a large effect on the drag coefficient. To investigate this, an additional simulation was conducted for a thin plate whose width (15.25 m or 50 ft) was equal to the total width of the two smaller plates (7.62 m or 25 ft each). Results in Table 2.2 show that the small gap between the plates had a negligible effect on the total drag coefficient ( $C_d=1.32$  vs. 1.33 in the two simulations).

## 2.7. Effect of clearance ratio and sign aspect ratio on drag coefficient for a traffic sign with perpendicular incoming wind

In this section the effects of varying the ground clearance ratio,  $s/h$ , and aspect ratio,  $B/s$ , is investigated for a thin rectangular traffic sign with a height  $s=5.8$  m=19 ft. All simulations were conducted for the case in which the wind direction is perpendicular to the traffic sign. The base case corresponds to  $B/s=2$  and  $s/h=0.3$ . With respect to the base case  $B/s$  was varied between 1 and 20 (very wide panel) and  $s/h$  was varied between 0.3 and 0.5, which is the typical range observed in the field for most traffic signs, including DMS cabinets. We choose to conduct this parametric study for a thin sign because of the availability of experimental data to compare our predictions of the drag coefficient. Results in Table 2.3 show that varying  $s/h$  between 0.3 and 0.5 has a negligible influence on the values of the drag coefficient. Meanwhile, it is found that  $C_d$  increases monotonically with increasing  $B/s$  and this increase is significant (e.g., from  $C_d=1.21$  for  $B/s=1$  to  $C_d=1.72$  for  $B/s=20$ , which is a 40% increase).

A similar parametric study was also conducted for a sign of smaller height ( $s=2.5$  m=8.2 ft) and a constant ground clearance ratio,  $s/h=0.3$ . Results are reported in Table 2.4 along with values predicted based on laboratory experiments.

Table 2.3 gives mean drag coefficient for a thin rectangular traffic sign ( $s=5.8$  m=19 ft) placed above the ground. The table shows the effect of varying the aspect ratio,  $B/s$ , and the ground clearance ratio,  $s/h$ , on  $C_d$ . Table 2.4 summarized the predicted value of the drag coefficient for the sign of smaller height ( $s=2.5$  m=8.2 ft). The table includes experimental results reported by Letchford (2001), Newberry and Eaton (1974) and the ASCE-7 (1995) standard. Figure 2.11 compares the numerical predictions of  $C_d$  for the signs with  $s=5.8$  m=19 ft and  $s=2.5$  m=8.2 ft with those of Letchford (2001), Newberry and Eaton (1974) and the ASCE-7 (1995) standard. Overall the present predictions for the  $s=2.5$  m panel are very close to those given by Newberry and Eaton (1974) and the ASCE-7 (1995) standard. Latchford (2001) predicts larger values of  $C_d$  for  $B/s < 10$ . Increasing the height of the traffic sign results in an increase of  $C_d$  for all  $B/s$  values. Still, the predicted values of  $C_d$  are fairly close to those given by Newberry and Eaton (1974).

Table 2.3 Mean drag coefficient for a thin rectangular traffic sign ( $s=5.8$  m=19 ft) placed above the ground

$B/s$	$s/h$				
	0.3	0.35	0.4	0.45	0.5
1	1.21				
2	1.23	1.22	1.22	1.22	1.23
5	1.36				
10	1.56				
15	1.64				
20	1.72				

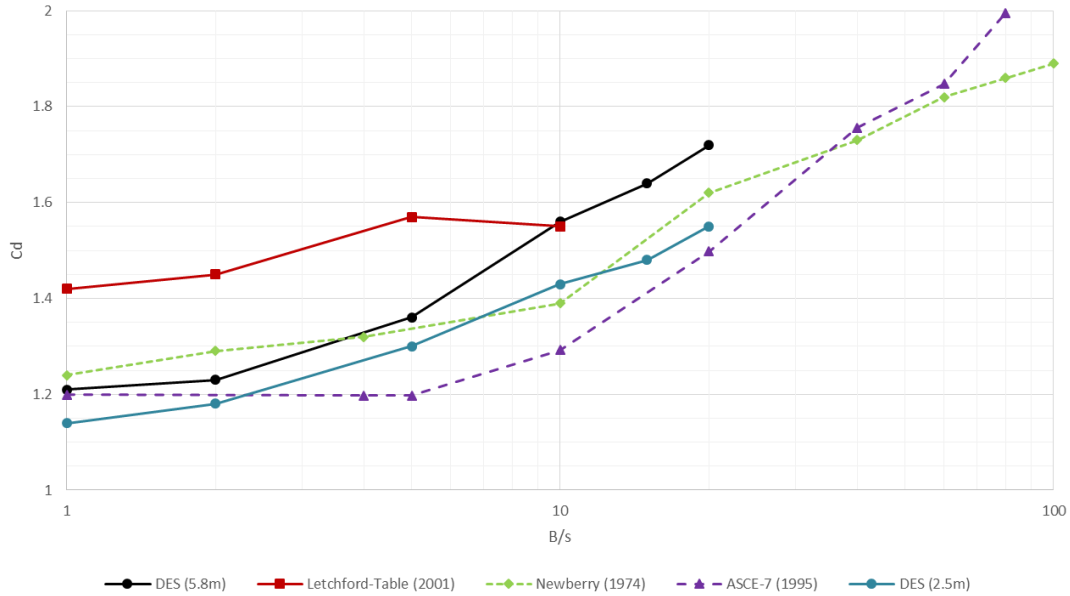


Figure 2.11 Effect of sign aspect ratio on the mean drag coefficient for a fixed clearance ratio. The figures shows present DES results for the rectangular sign with  $s=5.8\text{ m}=19\text{ ft}$  together with experimental results reported by Letchford (2001), Newberry and Eaton (1974) and the ASCE-7 (1995) standard.

Table 2.4 Mean drag coefficient for a thin rectangular traffic sign ( $s=2.5\text{ m}=8.2\text{ ft}$ ) placed above the ground.

B/s	Drag coefficient			
	DES ( $s=2.5\text{ m}$ )	Letchford (2001)	Newberry (1974)	ASCE-7 (1995)
1	1.14	1.42	1.24	1.2
2	1.18	1.45	1.29	
5	1.30	1.57		1.21
10	1.43	1.55	1.39	1.29
15	1.48			
20	1.55		1.62	1.50

## 2.8. Estimation of drag coefficients for the members of the truss supporting a DMS cabinet

In the previous subsection the DMS cabinet was positioned above the ground but the truss was not included in the calculation. The inclusion of the truss on which the DMS is attached may slightly change the flow field around the DMS cabinet because of the additional obstruction of the flow around the DMS cabinet induced by the truss members. Figure 2.12 shows a sketch of the truss used in a RANS calculation in which the flow past a DMS cabinet fixed on a truss was simulated. The truss geometry is based on the specifications

provided by the Iowa DOT. One should mention that the model truss used in the CFD model does not have the truss members for the uprights. This is an acceptable approximation for the CFD.

The effect of attaching the DMS cabinet on the truss is to modify the forces acting on the truss members that are shielded by the DMS cabinet compared to the forces induced on the same members placed in a uniform flow of same speed. Most of the members for which the values of the forces are significantly modified are situated in the recirculating flow region induced by the DMS cabinet. The stream-wise forces on the truss members not shielded by the DMS cabinet but situated close to it are expected to slightly increase with respect to the case when no DMS cabinet is attached on the truss. This happens because the incoming flow approaching the DMS cabinet is accelerated as it passes the DMS cabinet.

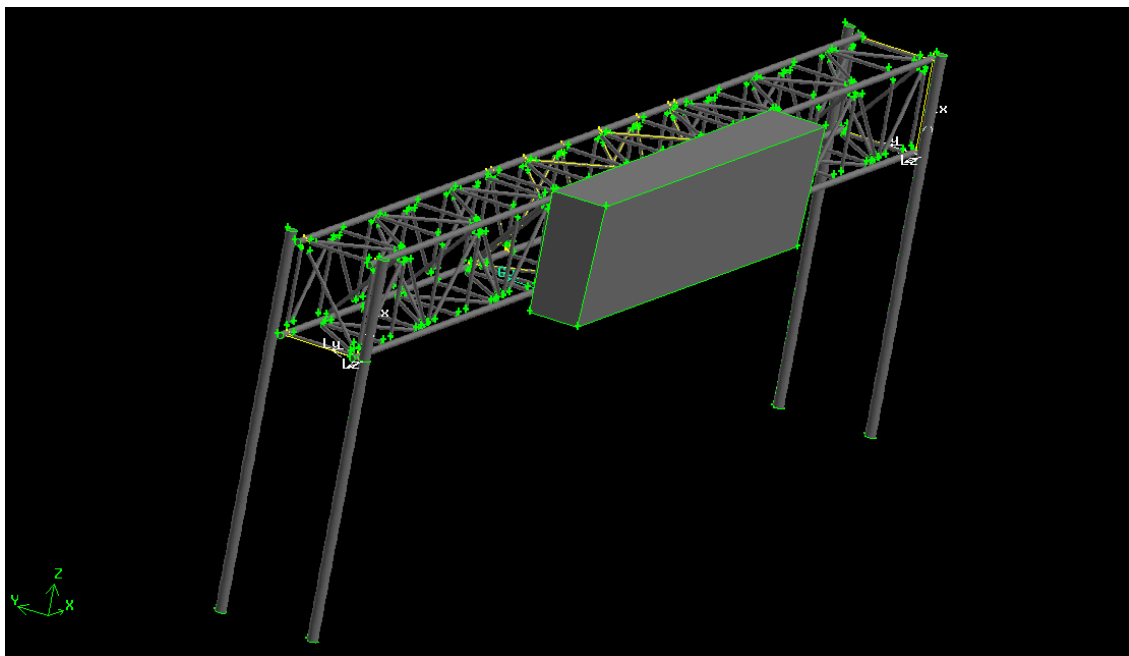


Figure 2.12 Sketch showing the truss on which the DMS cabinet is attached

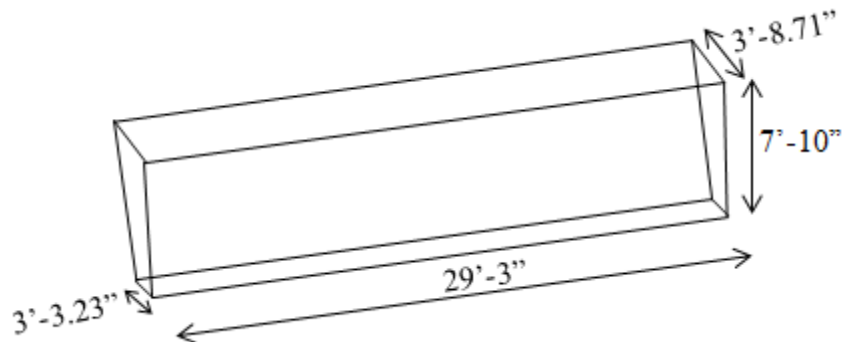


Figure 2.13 Sketch of the DMS cabinet used in the simulation of the flow past a DMS cabinet attached to a truss. The main dimensions of the DMS cabinet are shown.

In the RANS simulation, the wind velocity was constant and equal to 90 mph (40 m/s). The wind direction was perpendicular to the DMS cabinet and the truss. The size of the DMS cabinet is specified in Fig. 2.13. The DMS was situated at 5.2 m (17 ft) above the ground. The truss was situated behind the DMS cabinet with respect to the wind direction. The mesh contained close to 6 million cells needed to obtain a sufficiently fine mesh around the individual members of the truss. The truss members and its poles are labeled in Fig. 2.14 such that one can easily infer the relative position of the member inside the truss and with respect to the DMS cabinet. Figure 2.15 visualizes the computational domain around the truss.

Detailed information on the forces acting on the truss members is of interest for a more detailed structural analysis that accounts not only for the forces induced on the truss by the wind loads acting on the DMS cabinet but also for the wind loads acting on the individual members of the truss. CFD provides the resultant wind force acting in each of the three directions on the individual truss members. The force is simply obtained via integration of the pressure field on the surface. In the present analysis we focus on the stream-wise forces which are the dominant ones.

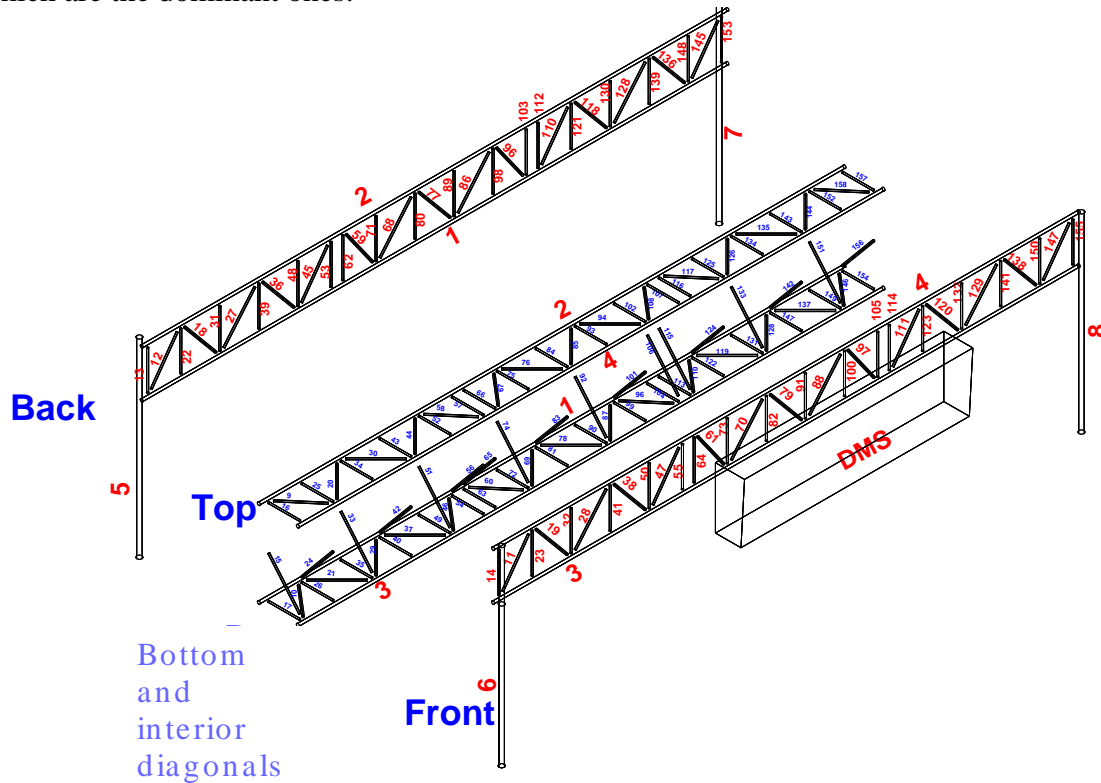


Figure 2.14 Sketch showing the convention used to identify the individual members of the truss and its poles. The numerical simulation provides the resultant wind force acting in each of the three directions on the individual truss members.

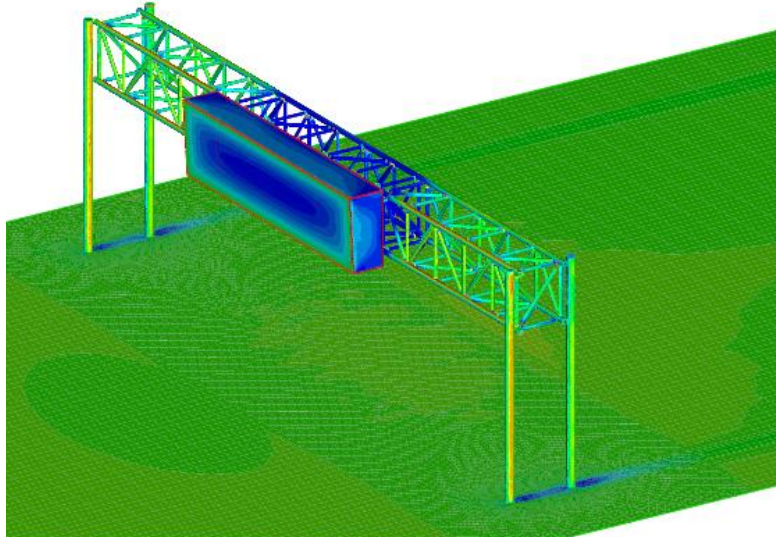


Figure 2.15 View of the computational domain.

Table 2.5 Drag coefficient members predicted for some of the truss members

Member #	$C_d$
41	1.3
23	1.11
28	1.11
50	1.73
39	0.78
22	0.72
27	0.83
48	0.71
70	-0.030
73	-0.017
91	-0.023
68	-0.086
71	-0.066
80	-0.093
21	0.26
37	0.33
33	0.34
15	0.28

The  $C_d$  values of the members situated away from the DMS cabinet (e.g., members 41, 23, 28), directly exposed to the incoming flow and situated in a plane perpendicular to the wind

are close to 1.1-1.3 (Table). These values are close to the standard value  $C_d=1.2$  recommended by the procedures used by IDOT to determine forces on truss members. The  $C_d$  value for member 50 is larger ( $C_d=1.73$ ). This is because member 50 is situated in the flow acceleration region on one side of the DMS cabinet. One should mention that the  $C_d$  calculated with the mean velocity in the flow acceleration region is close to 1.15. However, without access to data generated from numerical simulations, the ratio between the mean velocity in the flow acceleration region and the incoming flow velocity is unknown, so for design purposes one should consider that all members are subject to the same incoming flow velocity and rather specify an appropriate (increased) value of  $C_d$  defined with the incoming flow velocity.

Another category of truss members is those subject of shielding. First we consider several members situated away from DMS cabinet but behind those directly exposed to incoming wind (e.g., members 39, 22, 27 and 48 in Table 2.5). The predicted values of  $C_d$  range between 0.7 and 0.83. So the reduction of the drag coefficient with respect to the unshielded members directly exposed to the incoming flow can be as high as 45%. The other category of members subject to shielding effects is for the members situated in the wake of the DMS cabinet. As expected, the forces acting on the shielded members part of the upstream face of the truss are negligible (e.g.,  $|C_d|<0.03$  for members 70, 73 and 91 in Table 2.5). These members are situated very close to the downstream face of the DMS cabinet inside the recirculation bubble containing slowly moving flow. The drag coefficient values are slightly larger for the shielded members, part of the downstream face of the truss (e.g., members 68, 71 and 80 in Table 2.5). Still the magnitude of the drag coefficient remains below 0.1 for these members. So, one can safely assume  $C_d=0$  for all members shielded by the DMS cabinet. The same is true for the members connecting the front and back faces of the truss situated outside of the wake of the DMS cabinet and for the members parallel to the flow (e.g., members 35 and 40).

The members connecting the front and back faces of the truss and situated in a horizontal plane are shielded by members 3 and 4. For these members the reduction of  $C_d$  is of the order of 75% compared to the values observed for the case the member is directly exposed to the incoming flow (e.g., see predicted  $C_d$  values for members 21 and 37 in Table 2.5). Finally, a similar reduction of the order of 75% is observed for the inclined members connecting the top and bottom faces of the truss. These members are also shielded by corresponding vertical elements part of front face of the truss. These results can be used to propose criteria to approximate the values of the drag coefficient of the truss members based on the relative position of the truss member relative to the DMS and to other members of the truss.

### **3. Vulnerability assessment of sign support structures during transportation**

#### **3.1 Literature review**

A review of the existing literature indicates that Barle et al. (2011) investigated the truss joints by modeling the stress fields under static and dynamic loads. This study was able to estimate the fatigue life of the structure and make suggestions for design improvements. Roy et al. (2010) examined the weld geometry at the joints and evaluated crack modes through experimental fatigue tests. In a study not limited to the joints, Rice et al. (2012) combined numerical simulations with field measurements to better understand the fatigue characteristics of sign structures. Sanz-Andrés et al. (2003) provided a qualitative explanation of the main characteristics that capture the evolution of vehicle force causing fatigue damage. Huckelbridge and Metzger (2007) conducted a fatigue analysis of a sign structure under the vibration of truck passage. Different types of overhead truss structures were studied by Fouad et al. (2003) to understand the influence of natural wind gusts. In a separate effort, Kacin et al. (2012) conducted a fatigue life analysis for an overhead sign-support structure. They utilized the ANSYS package to model the structure and identify the critical members in both pristine and damaged conditions. Wind-induced fatigue analysis of high-mast light poles was conducted by Chang et al. (2009 and 2010) using long-term field monitoring data. In a later study, Chang et al. (2014) investigated the effects of thermal loads on the aluminum DMS-support structures.

Despite the contribution of the former studies, they are found to be primarily focused on the loads that the structure experiences during the service life, disregarding the potential contribution of stresses induced during transportation from the fabrication site to the location of installation. As a result, the potential damage that this important category of structures may sustain during transportation is largely unknown. To investigate this aspect, a comprehensive field test and numerical study is conducted in the current study. For this purpose, one span of a four-chord, overhead sign-support structure is instrumented with strain gauges. The main objective of this short-term monitoring is to capture the strains induced in the truss members because of the excitations caused by the road profile.

#### **3.2. Field study**

To evaluate the effects of road-induced excitations on DMS-support truss structures during transportation, a field study has been conducted on one of the three blocks of a truss structure, which was shipped from the State of Kansas to Iowa for installation. The truss under consideration was transported for a distance of approximately 110 miles (1 mile = 1.609 km). The average speed of truck was in the range of 40-50 miles per hour. During monitoring, twelve one-axial strain gauges were mounted on the truss and the strain data were recorded in 33 data sets for a period of three hours with the frequency of 100 Hz, Arabi et al. (2017). Figure 3.1 shows the transported truss and the position of some of the mounted strain gauges. Figure 3.2 provides the identification number of all the strain gauges used for instrumentation and Fig. 3.3 illustrates the strain time histories recorded by the Sensor S1 and S12 over 120 seconds for the 3rd and the 30th data sets as two examples. A review of the data collected from all the 12 strain gauges indicates that the strain time histories follow a similar pattern overall and there is no abnormal strain in the

recorded time histories. Figure 3.3a clearly shows that there are peaks in the strain time histories, which occur at the same time in all the data sets (see for example the strain at the 10th and 115th second). This trend can be related to the road profile. The similarity observed in the time histories, as well as the absence of any major outliers, highlight that the collected data have an acceptable quality. To obtain a more in-depth understanding of the range of strains, the collected data have been processed and the maximum and minimum strain values for each sensor in each of the 33 recorded data sets are summarized in Fig. 3.4. As it can be seen in this figure, the strains are mostly in the range of -20 to +20 micro-strain, although there are some data points which exceed this range. Table 3.1 summarizes the maximum and minimum strain values for each sensor. Since the data have been recorded in separate time intervals during transportation, the average of maximum and minimum values obtained for each time interval has also been included in Table 3.1. This table provides an envelope with a peak and average value for each sensor, which reflect the range of strains that each truss member may experience. This range is also used to evaluate the accuracy of predictions obtained from the FE model generated for this study. As failure due to fatigue is the most critical mode of failure in sign-support structures, a detailed fatigue analysis is conducted using the data collected from the field. The goal of this analysis is to evaluate the potential contribution of road-induced excitations to the fatigue-induced damage. For this purpose, the rainflow cycle counting method is utilized to count the number of cycles for various stress ranges that the structure has experienced during transportation. The Miner's rule is used in the current study to determine if any fatigue-induced damage occurs during transportation (Miner, 1945). To conduct the fatigue analysis, the strain time histories are first converted to the stress time histories using the well-known Hook's Law. Although this direct conversion may involve some approximation (due to shear and/or bending moment), the percentage of error is deemed negligible because the truss consists of long and hollow members, mainly under a uniaxial loading condition.

Based on the stress time-histories obtained along the length of truss members, the stress time histories at the joints can be predicted. Despite the similarities between the patterns of stress time histories at the middle and end of a truss member, it is known that the stresses are magnified at the joints due to strain concentration effects. The strain concentration factor (SCF) is reported in the AASHTO Standard Specifications for Structural Supports for Highway Signs, Luminaires, and Traffic Signals (hereafter referred to as AASHTO Specifications) based on the type of connection (AASHTO Specifications, 2015). Using the magnified stress time histories, the number of cycles for various stress ranges are obtained for the fatigue analysis. Figure 3.5 presents the histograms of stress ranges and their respective number of cycles for 6 sensor/joint locations. The histograms are plotted in a logarithmic scale to depict the number of cycles clearly. A review of the developed histograms shows that all of the cycles are below the constant amplitude fatigue threshold (CAFT), which is 4500 psi (1 psi = 6895 Pa) for the slotted tube to gusset plate connections (AASHTO Specifications, 2015). This eliminates the concern about experiencing a high level of fatigue-induced damage during transportation.

### 3.3. Numerical study

In addition to the field investigation, a detailed FE model of the instrumented truss structure has been generated in the ABAQUS package to obtain a comprehensive assessment of the structural response of individual truss members further to their potential modes of damage and failure. To model the joints with necessary details, shell elements are used for the truss members and connecting gusset plates. This approach allows for the determination of stress distribution within the thickness of each truss member. Figure 3.6 shows an overview of the FE model together with a close view of connection details. Mesh patterns reflect a fine mesh at critical joint locations, while a coarse mesh has been used for the rest of the elements. The FE simulations conducted in the current study pursue three key objectives: (1) To determine the effect of road profile on the range and number of cycles of stress, which can lead to fatigue-induced damage; (2) To identify the most vulnerable members of the truss and their connecting joints during transportation; and (3) To evaluate the extent of stress magnification from the middle to the end of individual truss members. To achieve the listed objectives, the road-induced excitations are applied to the truss model. This requires modeling of the road profile and the truck's suspension system following the procedure discussed in the next sections.

#### 3.3.1. Road profiles

There are several studies devoted to the generation of road profiles and related subjects. Among all the procedures available for road roughness generation, Power Spectral Density (PDS)-based procedures have received a great attention, for instance Dodds and Robson (1973), Andren (2006), Elson and Bennet (1995) and Tyan et al. (2009). In this study, artificial road profiles are generated based on the PSD-based procedure introduced by ISO 8608 (1995). This involves using the following formula to generate the road profile,  $h(x)$ , for different road surface classes:

$$h(x) = \sum_i \sqrt{\Delta n} \cdot 2^k \cdot 10^{-3} \cdot \left(\frac{n_0}{n_i}\right) \cdot \cos(2\pi n_i x + \varphi_i) \quad (3.1)$$

where  $\Delta n$  is the frequency band,  $k$  is the constant value determined based on the road profile class,  $n_i$  is the spatial frequency,  $n_0 = 0.1$  cycle/meter, and  $\varphi_i$  is the random phase angle distributed uniformly from 0 to  $2\pi$ . According to ISO 8608, the road surface will degrade by increasing the value of  $k$ . The  $k$  values for different road classes from good to poor have been tabulated in Table 3.2. A detailed explanation on the generation of reliable artificial road profiles has been provided by Agostinacchio et al (2014). It must be noted that Equation 1 does not capture the unexpected road bumps and potholes. This, however, is expected not to influence the predictions in any significant way, as the number of cycles associated with bumps and potholes in the recorded strain time histories was found to be negligible. Road profiles generated for a sample of 250 meters are shown in Fig. 3.7. After generating the necessary road profiles, the next step is to model a suspension system capable of transferring the excitation induced by the road roughness to the truss structure that is being shipped by the truck.

#### 3.3.2. Suspension system

There are different types of car models available in the literature for different purposes. While the quarter car model is utilized for spectral analysis, the full car model is used for

advanced control and comfort studies (Barbosa, 2011). Many researchers have conducted studies on suspension system modeling. Among them, Shpetim (2012) presents a mathematical model of a quarter car suspension system to study its performance of active, semi-active and passive systems. In that study, Simulink was utilized for solving the differential equation of suspension system. Meanwhile, Chavan et al. (2016) took the nonlinearity of parameter values of suspension system into account to design a more realistic and precise suspension model. Moreover, Sharma et al. (2013) conducted a study aimed at preventing the vibration induced by the road roughness from being transferred to a driver. A quarter car model with two degrees of freedom was used in this study. Also, Alexandru and Alexandru (2011) compared the ride and handling of passive and semi active suspension system. They found out that the acceleration of body mass is lower for the semi active suspension system for a specific road profile. Similar studies of suspension systems with a more detailed look at suspension system parameters can be found in Iyer et al. (2007) and Prabhakar and Arunachalam (2015).

In this study, the quarter car model is used to capture the response of a passive suspension system and the consequent excitation transferred to the truss structure during transportation. The suspension diagram shown in Fig. 3.8a is a quarter car system, in which  $m_s$  is the sprung mass,  $m_{us}$  is the unsprung mass,  $k_s$  is the stiffness coefficient of the suspension system,  $k_{us}$  is the stiffness of the tire,  $c_s$  is the damping coefficient of the suspension system,  $Z_s$  is the displacement of sprung mass,  $Z_{us}$  is the displacement of unsprung mass, and  $Z_r$  is the excitation from the road roughness. Since the primary focus of this study is on the vertical excitation that the truss structure experiences, only vertical mass movements are modeled and the movements in the other directions of the vehicle are disregarded. It must be noted that the accuracy of the generated road-induced excitations could be further improved if further details regarding the tire-road contact, the truck dynamic, and its suspension system, were available to be included in the developed model.

Equations of motion can be introduced using the Newton's second law for each mass and Newton's third law for their interactions.

$$m_s \frac{d^2 Z_s}{dt^2} + c_s \left( \frac{dZ_s}{dt} - \frac{dZ_{us}}{dt} \right) + k_s (Z_s - Z_{us}) = 0 \quad (3.2)$$

$$m_{us} \frac{d^2 Z_{us}}{dt^2} + c_s \left( \frac{dZ_{us}}{dt} - \frac{dZ_s}{dt} \right) + k_s (Z_{us} - Z_s) + k_{us} (Z_{us} - Z_r) = 0 \quad (3.3)$$

Since solving the equations above is nontrivial, the Simulink package is used. Fig. 3.8b depicts the Simulink model for solving the coupled differential equations of the suspension system. There are some suggested values for suspension system parameter in the literature for a car, bus, and heavy truck. However, to the best of author's knowledge, there are not any parameter values for the trucks which were used for the trusses transportation. Hence, the car suspension system parameter values were utilized to solve the differential equation of suspension system, because those values are the closest one to the truck in comparison with the bus and heavy truck. The values were selected from Agostinacchio et al. (2014). It should be mentioned that the parameter values were adjusted to consider the weight of the truss. The selected parameters were tabulated in Table 3.3. It was assumed that the tires

do not lose contact with the pavement during transportation. The input file of the Simulink model includes road roughness values, which are an array of equally spaced data points. Three road classes with  $k = 3, 4,$  and  $5$  are investigated in the current study. Figure 3.8c shows the Simulink results for the sprung mass, unsprung mass and road profile for 40 seconds for various values of  $k$ . The body displacement obtained at this stage is used as an input to the FE model of the truss structure for the purpose of capturing the road roughness effects.

### *3.3.3. Validation of FE model*

To validate the multi-step procedure developed to investigate the structural response of truss structures through numerical simulations, the strain time histories obtained from the FE model for the individual truss members are compared with the envelope of strain time histories obtained from the field study (i.e., Fig. 3.4). Two strain time histories extracted from the FE model for  $k = 3$  and  $5$  are shown in Fig. 3.9, respectively. The strain time histories are recorded at the exact location of the strain gauges mounted on the actual truss. All the strains obtained from the field study fall in the envelope provided by the FE simulation results with  $k$  in the range of 3 to 5. This highlights that the developed FE model can successfully capture the strains that the truss members experience during transportation.

## **3.4. Results and discussions**

### *3.4.1. Stress concentration factor*

Stress Concentrations Factor (SCF) is an essential factor for both fatigue design and analysis of sign-support structures. As it is proven that a higher SCF leads to a lower fatigue life, an accurate estimate of the SCF is expected to be critical to obtain an efficient and economic structural design and configuration. In addition, from an analysis point of view, the fatigue life of a structure can be predicted with the least underestimation or overestimation if an accurate SCF is utilized. Following the procedure provided by the AASHTO Specifications for fatigue analysis, the stresses must be calculated based on the net cross-sectional area of the truss members and then magnified by a prescribed constant value of 4.0. The SCF, however, is known to be influenced by the direction of applied loads and the position of individual truss members, in addition to their boundary conditions. In this study, the direction of loads applied to the truss structure during transportation is completely different from the direction of loads that the structure is expected to experience after installation in the field. As a result, for the fatigue analysis of the structure during transportation, a revised set of SCFs must be obtained. To achieve this goal, the developed FE model is utilized and the SCFs are derived with the following steps: (1) The most critical element at the end of each truss member is identified by comparing the suspected critical elements at each joint; (2) The stress time history is derived at the middle of the truss members, where the sensors were mounted during transportation; and (3) The SCFs are estimated by comparing the stress time histories obtained for the middle and end of each truss member.

Based on the AASHTO Specifications (2015), the stress time history intended to be used for fatigue analysis must be derived from the areas adjacent to the welded parts. Therefore,

a comprehensive procedure is implemented to select the most critical element for each truss member. Following is the procedure used for this purpose: All the elements located on one weld line are selected. The stress time histories are then obtained for the selected elements and comparisons are made to identify the elements that constantly experience the highest stress values. Figure 3.10 shows the elements selected for deriving the stress time histories, as well as the stress time histories derived from the numerical simulations.

The outcome of this investigation highlights that the elements with the highest stress are those closest to the hole of the truss members. This criterion leads to four elements at each end of the truss member. There are eight elements in each tubular member adjacent to the hole, which directly experience the welding effects. Figure 3.10 depicts four of those eight elements at one end of a member. The stress time histories for the eight elements are illustrated in Fig. 3.10. The element with the highest value of stress in this figure is the most critical element of the member. For example, Element 322 is the most critical element in the member that carries Sensor S1. The next step is to examine the stress time history at the middle of the member. In reality, a sensor can be mounted anywhere on the perimeter of the truss member. Thus, the effect of the sensor's mounting location must be considered as well. To address this aspect, all the elements at the middle of the truss member are selected in one cross section for deriving the averaged stress time histories. Since the truss members normally experience pure compression or tension, averaging the stress in the cross section is expected not to introduce a major approximation. Figure 3.11 shows how the stress time histories obtained for the middle of the member are compared with the one recorded at the most critical element at the end of the same member.

For deriving the ratio of stress in the critical element to the stress at the middle of the member, a MATLAB code has been generated to pick the highest value in each peak and valley. This is an important step to avoid the outliers that may appear if the stress values are close to zero. This ratio has been shown in Figure 3.12 for Sensor S1 and S2. Table 3.4 summarizes the SCFs obtained from the numerical simulations for various members of the truss. Although the fillet welds have not been explicitly included in the FE model, the calculated SCFs can be below or above 4.0, which is the SCF recommended by the AASHTO Specifications (2015).

#### 3.4.2. Fatigue damage analysis

The stress life method has been utilized in the current study for the fatigue analysis of the truss structure. The basis of this method is the S-N curves, which represent the stress ranges versus the number of cycles. Following is the equation of each S-N curve.

$$N_i = \frac{A}{S_i^3} \quad (3.4)$$

where  $A$  is a constant value given by AASHTO Specifications (2015) based on the connection category,  $N_i$  is the number of cycles needed to cause failure at the  $i$ -th stress range, and  $S_i$  is the corresponding stress range. The AASHTO Specifications (2015) provide a table including various types of sign support structure connections, such as groove welded and fillet welded connections. The connection categories are A, B, B', C, D, E, E', ET and K2. In this study, the type of connection is a slotted tube to gusset plate

connection with the coped hole, which falls in the E stress category. Figure 3.13 shows the connection of interest in the current study which has been presented by AASHTO specifications (2015). Based on the AASHTO specifications (2015), the highlighted parts in red, being near the weld, are the most critical area prone to fatigue crack propagation and failure.

To investigate probabilistic considerations in the fatigue life analysis, a set of S-N curves are developed for different confidence percentiles. This reflects the fact that the samples that were subjected to fatigue tests provided a distribution of stress ranges under a given number of cycles. Using the statistical properties reported by Moses et al. (1987) for the S-N curves of connections in the E Category, Figure 3.14 shows the S-N curves for the mean ( $\mu$ ) and mean plus various standard deviations, i.e.,  $\mu + \sigma$ ,  $\mu + 2\sigma$ , and  $\mu + 3\sigma$ , representing 50, 84.1, 97.7, and 99.9 percentiles, respectively. For comparison purposes, the S-N curve provided by the AASHTO Specifications (2015) (equivalent to 94 percentile) is included in this figure as well. The AASHTO recommended curve has been used for the fatigue analysis presented in this section.

Based on the Miner's rule, the damage resulted from a specific stress range is a linear function of the number of cycles occurred at that stress range. The Miner's rule formula can be expressed as:

$$D_i = \frac{n_i}{N_i} \quad (3.5)$$

where  $N_i$  is the number of cycles needed to cause failure at the  $i$ -th stress range and  $n_i$  is the number of cycles of the stress range  $S_i$ . The value of  $N_i$  can be calculated by using Equation (3.4) and the value of  $n_i$  can be found by applying the rainflow cycle counting method on the stress time histories. Once the damage for each specific stress range  $S_i$  is found, the total damage  $D$  can be found using the following equation.

$$D = \sum_i D_i \quad (3.6)$$

According to the Miner's rule, the failure will occur if the total damage,  $D$ , becomes equal to 1.0. It must be noted that the Miner's rule disregards the mean stress correction. This, however, has been shown to have negligible effects on the fatigue analysis of overhead sign-support structures Ginal (2013), Rice et al. (2012) and Kacin et al. (2010).

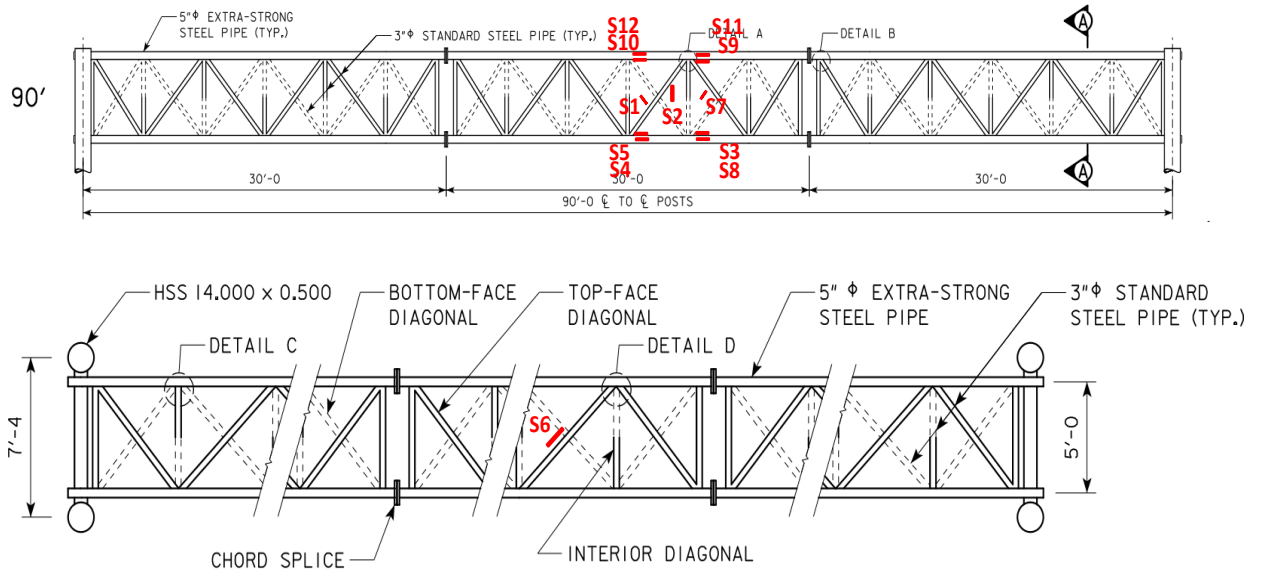
In the current study, fatigue analysis has been conducted on: (1) the data collected from the field; and (2) the results obtained from FE simulations. Based on the stress ranges and cycles obtained from the field data (as illustrated in Fig. 3.6), the percentage of fatigue damage is calculated for all the truss members that were instrumented with a strain gauge. The outcome of the fatigue analysis on the field data is shown in Fig. 3.15. The most critical member of the truss has experienced 0.01% of failure damage during transportation.

The fatigue analysis has been conducted on the numerical simulation results as well. This includes three road classes A, B and C. The three most critical members have been identified for fatigue analysis. The first member is the lower chord of the truss adjacent to the point where the truss is sitting on the truck. The second member is one of the interior diagonals and the third member is one of the vertical diagonals. Figure 3.16 shows the

results of the rainflow cycle counting analysis of the identified critical member for different road classes. The outcome of the fatigue analysis has been summarized in Fig. 3.17, which depicts the percentage of fatigue damage for each of the critical members under the three road classes. Moreover, Fig. 3.17 depicts the percentage of the fatigue damage for each of these members for different road classes. According to this figure, the percentage of fatigue damage for the most critical member of the structure is approximately 0.002% of failure damage for the road class A ( $k=3$ ) and 0.03% of failure damage for the road class B ( $k=4$ ). This values are in a close agreement with the fatigue damage percentage derived from the field data. The location of the highest fatigue damage in the FE model is consistent with the findings from the field investigation, which identified the lower chord of the truss as the most vulnerable member. It should be noted that the fatigue damage to the structure can increase to approximately 0.1% of failure damage if the truss is transported in road class C ( $k=5$ ).



Figure 3.1 Preparation of transported truss for short-term monitoring.



### PART TOP VIEW

Figure 3.2 Geometry and details of the truss further to the instrumentation layout. This truss was transported in three separate parts. The middle part is the subject of the current study.

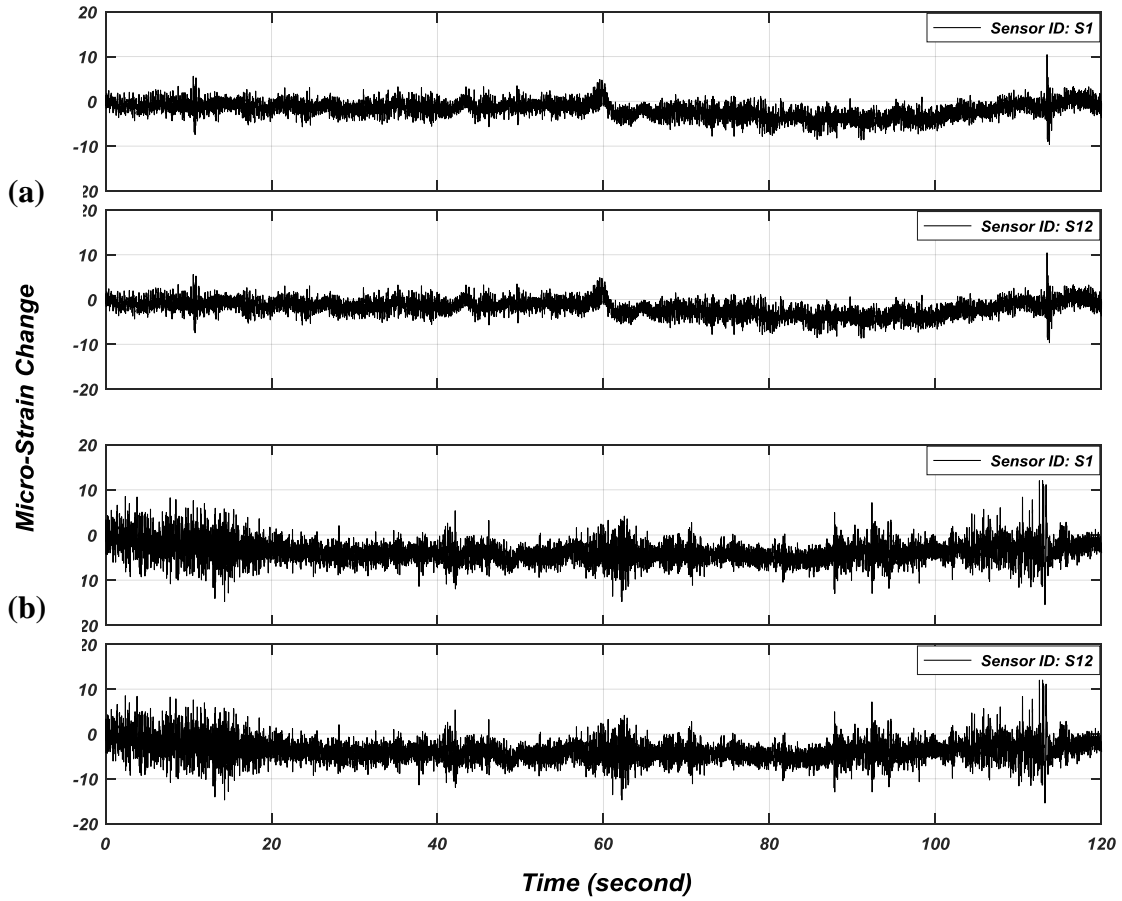


Figure 3.3 Strain time histories derived from Sensors S1 and S12 for two data sets: (a) 3<sup>rd</sup> data set, and (b) 30<sup>rd</sup> data set.

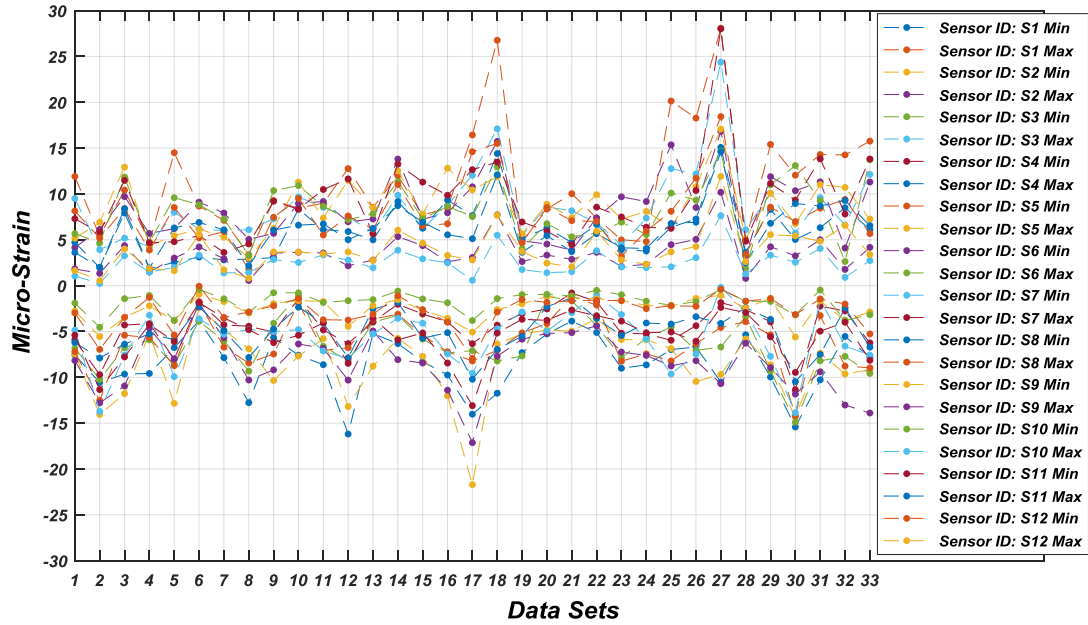


Figure 3.4 Maximum and minimum strain values recorded by strain gauges in each data sets.

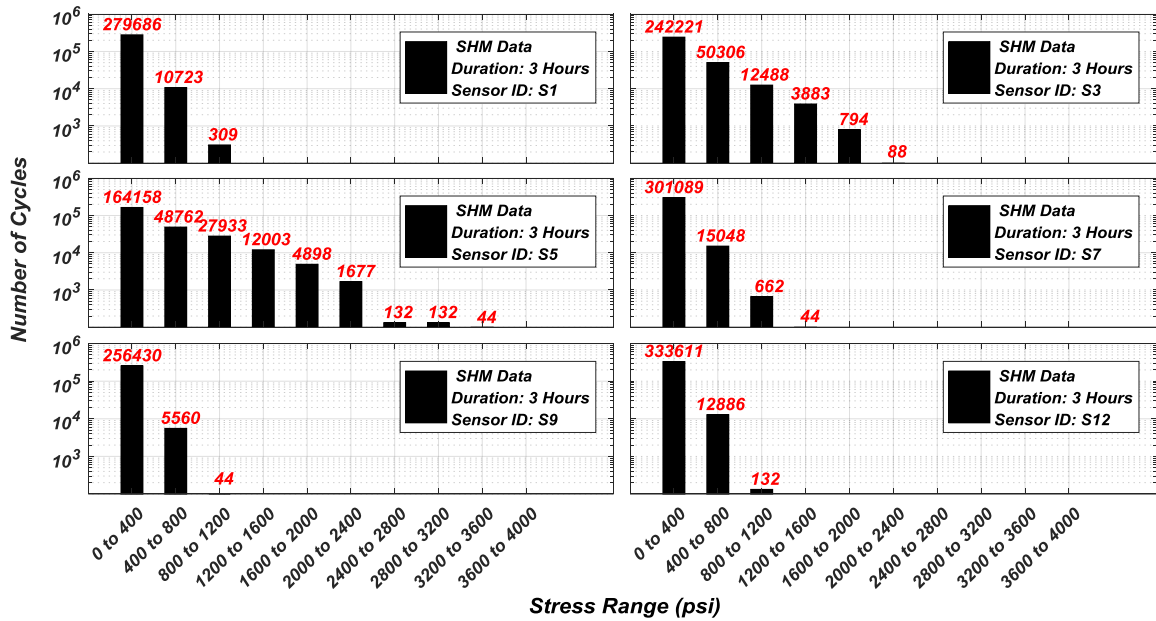


Figure 3.5 Stress ranges and their respective cycles for the truss members instrumented during transportation.

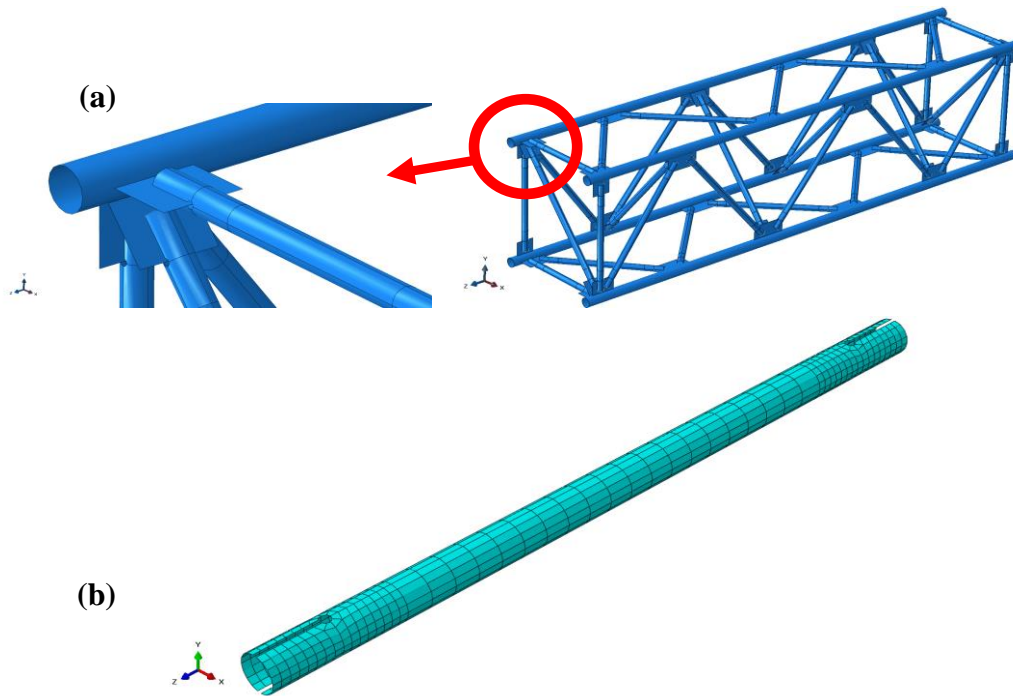


Figure 3.6 Finite element model: (a) big picture of finite element model and close view of connection, and (b) mesh pattern of members.

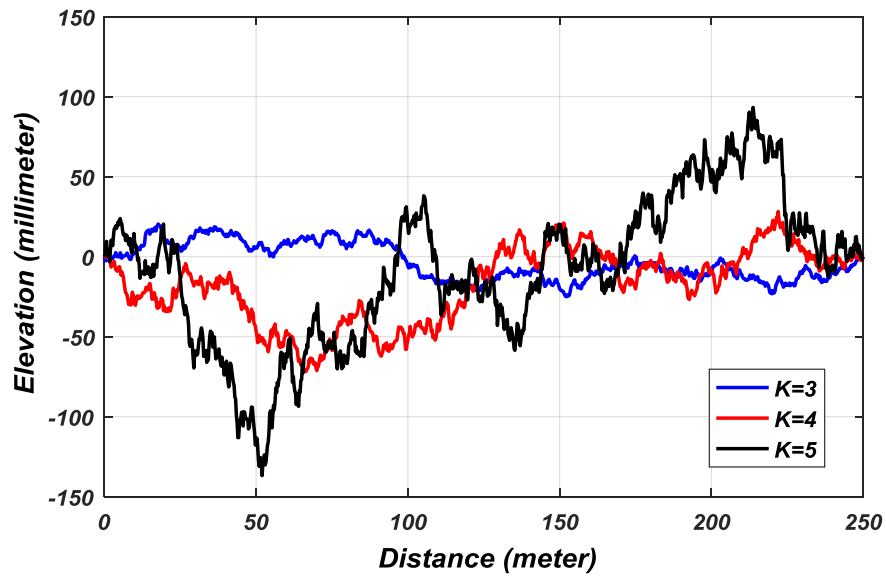


Figure 3.7 Artificial road profiles under three different road classes for a sample of 250.

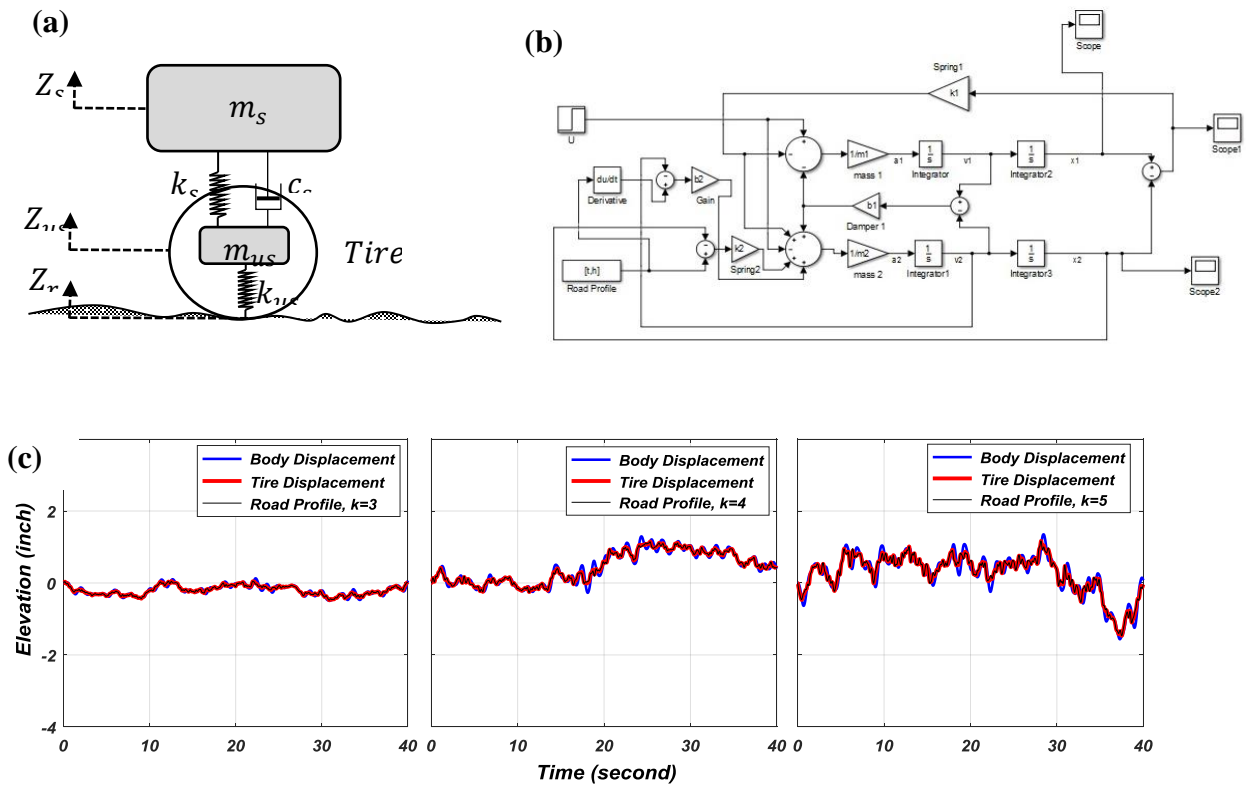


Figure 3.8 Suspension system simulation procedure: (a) schematic representation of truck suspension system, (b) Simulink model used for solving the suspension system equations, (c) response of suspension system for three road classes.

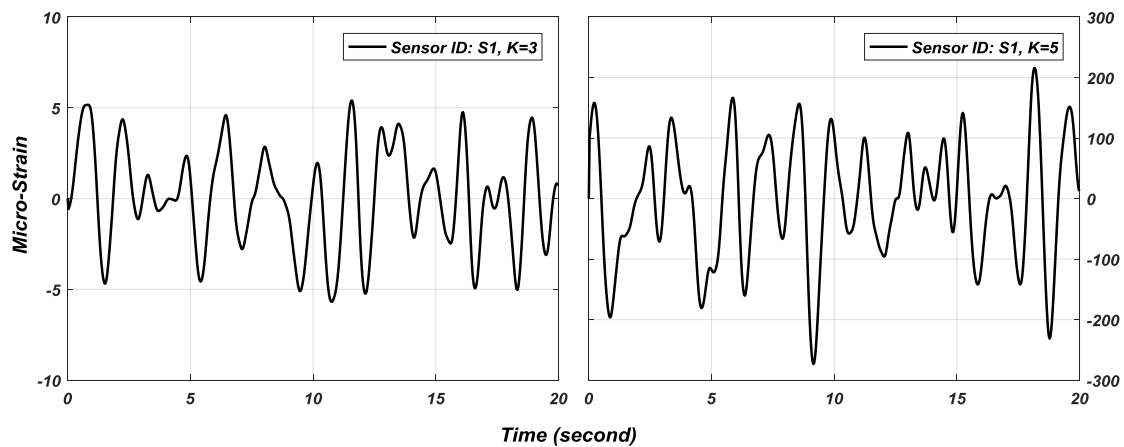


Figure 3.9 Strain time history derived from the FE model road profile A (left) and C (right).

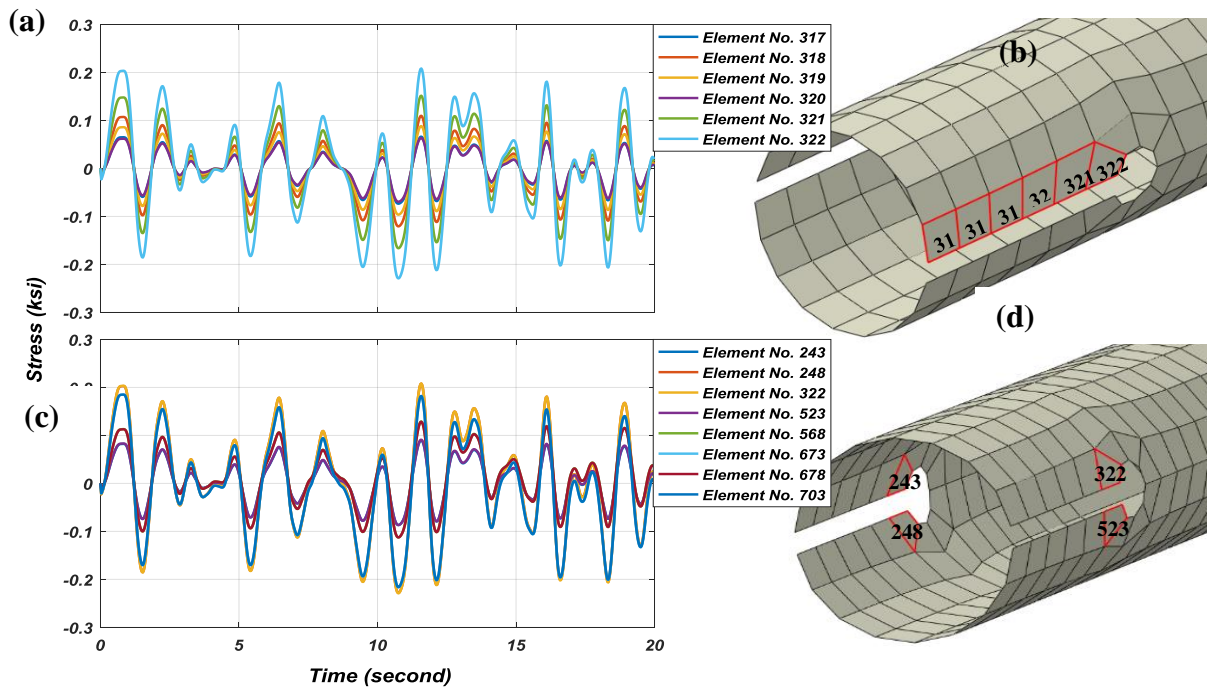


Figure 3.10 Procedure of finding the most critical element of a member: (a) stress time histories of all the elements located on one weld line, (b) elements location on one weld line, (c) stress time histories of eight elements adjacent to the hole, and (d) elements location adjacent to the hole.

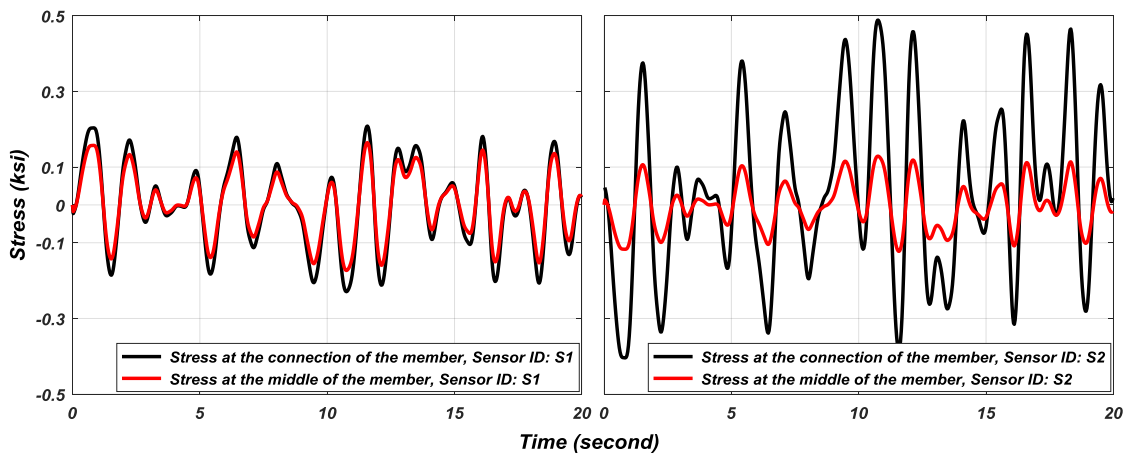


Figure 3.11 Stress time histories at the middle and the connection of two truss members obtained from FE simulations.

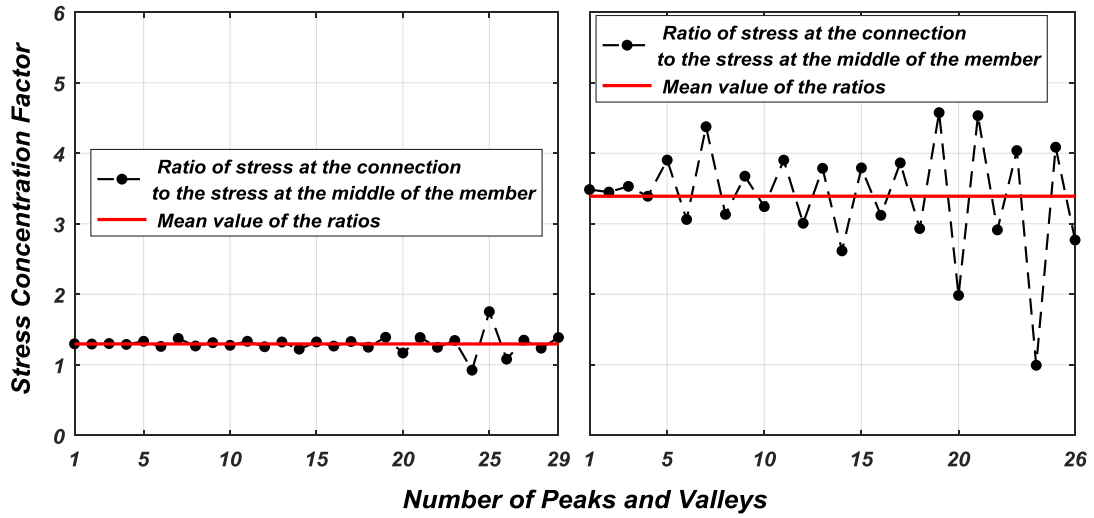


Figure 3.12 SCF changes and the corresponding mean value for Sensors S1 (left) and S2 (right).

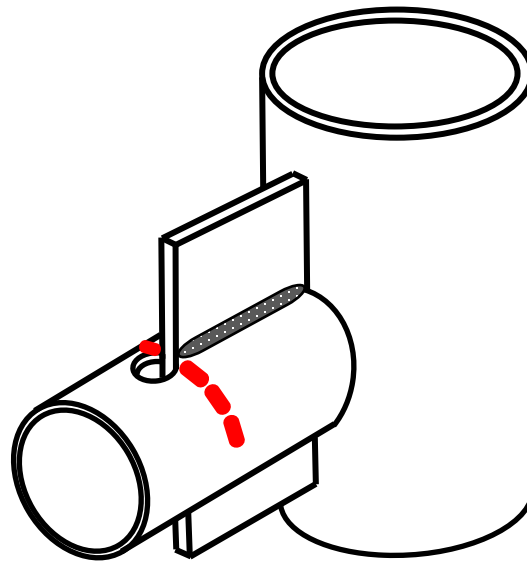


Figure 3.13 Connection detail investigated in the current study

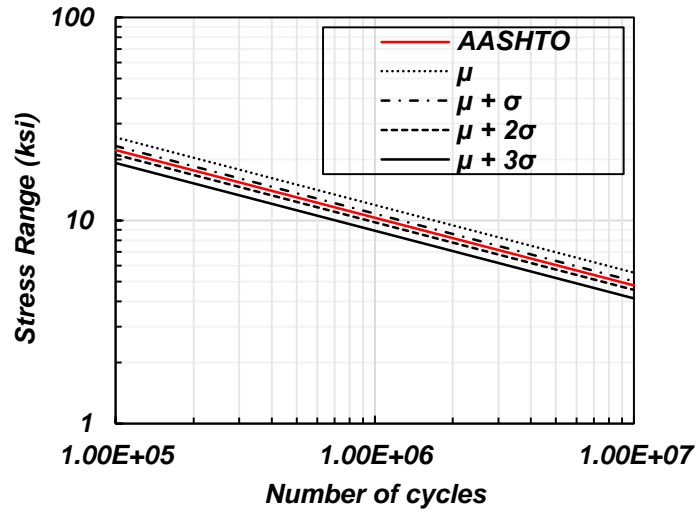


Figure 3.14. Developed S-N curves considering various confidence percentiles (1 ksi = 6.895 MPa).

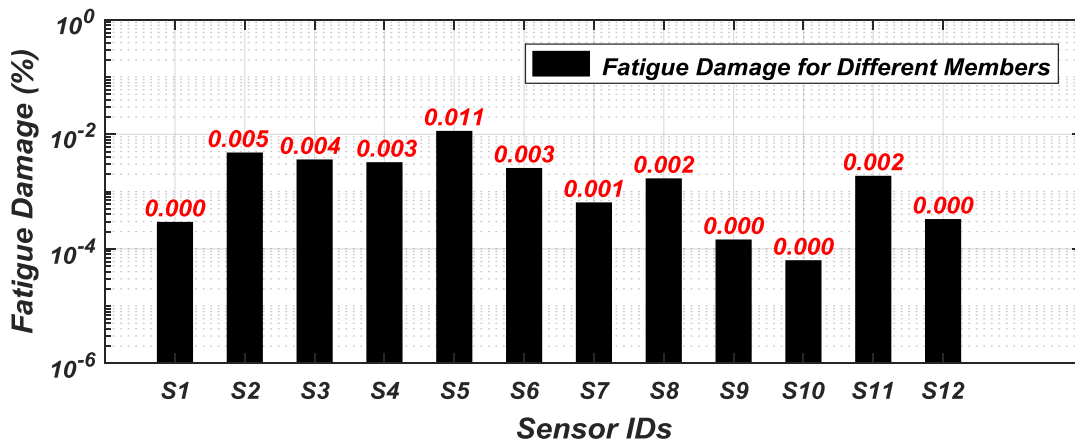


Figure 3.15 Fatigue damage estimated for the truss members instrumented during transportation.

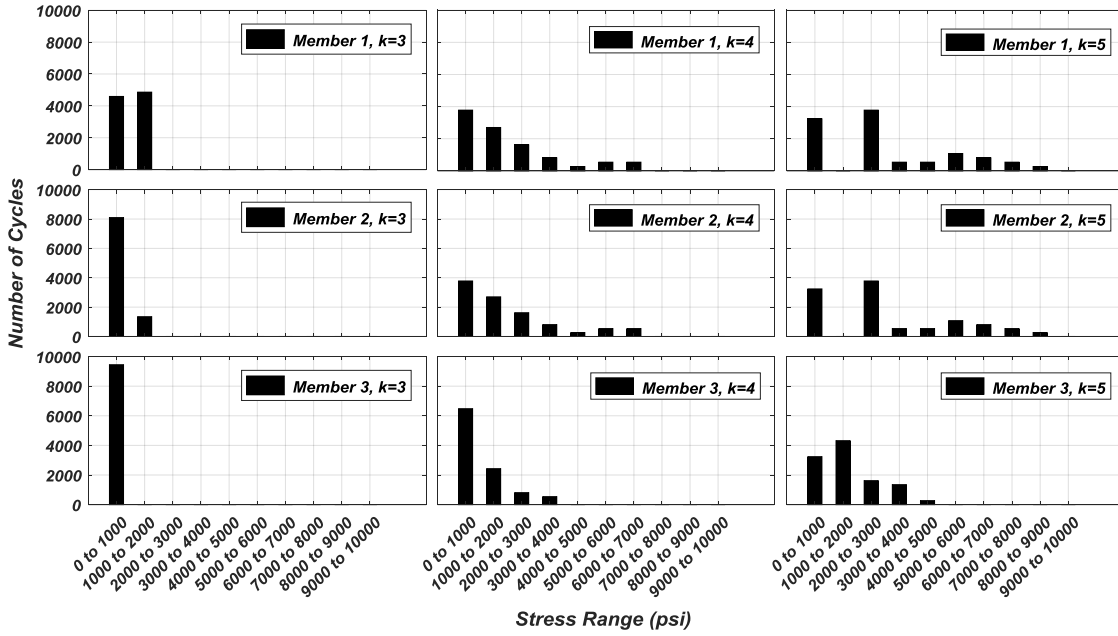


Figure 3.16 Stress ranges and their respective cycles for the most vulnerable truss members obtained from the numerical simulations under three different road classes.

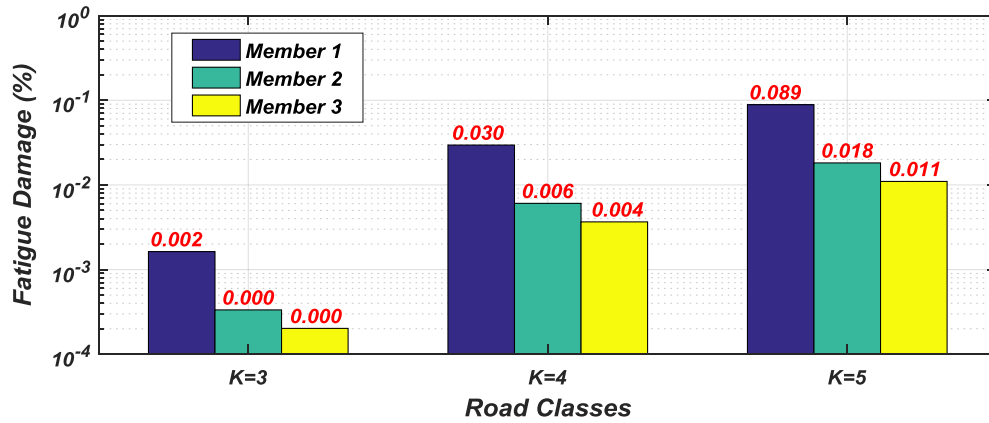


Figure 3.17 Fatigue damage in the most critical truss members based on numerical simulations.

Table 3.1 The range of strain values recorded by the strain gauges during transportation.

Sensor ID	Max. Value (Micro-strain)	Min. Value (Micro-strain)	Avg. of Max. Values (Micro-strain)	Avg. of Min. Values (Micro-strain)
S1	28.1	-16.2	11.2	-8.5
S2	16.8	-21.7	8.5	-8.4
S3	24.4	-14.9	8.6	-6.5
S4	15.1	-11.4	6.1	-4.4
S5	17.1	-14.2	8.5	-6.3
S6	14.7	-17.1	8.1	-8.5
S7	28	-13.9	9.1	-5.8
S8	18.4	-10.5	7.7	-5
S9	10.2	-5.6	3.5	-2.5
S10	7.6	-4.6	2.5	-1.8
S11	14.6	-13.1	6.2	-5.5
S12	11.9	-8	3.8	-2.7

Table 3.2 Values of k for ISO road profiles.

Road Class	A	B	C	D	E	F	G
K	3	4	5	6	7	8	9

Table 3.3 Selected values of parameters for the quarter car suspension system.

Parameter	Value
Sprung mass $m_s$ [Kg]	800
Unsprung mass $m_{us}$ [Kg]	40
Suspension stiffness $k_s$ [N/m]	21000
Suspension dumping $c_s$ [N·s/m]	1500
Tire stiffness $k_{us}$ [N/m]	150000

Table 3.4 A comparison between the SCFs obtained from the numerical simulations and the constant value recommended by the AASHTO Specifications.

<b>Sensor ID</b>	<b>Location of the member in the truss</b>	<b>SCF derived from numerical simulations</b>	<b>Difference with AASHTO recommendation</b>
S1	Vertical diagonal	1.30	-68%
S2	Interior diagonal	3.39	-15%
S6	Horizontal diagonal	3.03	-24%
S7	Vertical diagonal	1.91	-52%
S3, S8	Lower chord	3.72	-7%
S4, S5	Lower chord	5.70	+43%

## **4. Vulnerability assessment of Dynamic Message Sign support structures under environmental stressors**

### **4.1. Field investigation and monitoring**

#### *4.1.1. DMS-support truss structures*

A long-term field monitoring program has been established for two representative steel DMS-support structures in Des Moines, Iowa to obtain an in-depth understating of their vulnerability to the fatigue induced by diurnal temperature changes. Figure 4.1 shows the location of the two DMS-support structures (labeled as Truss A and B) on the map. Since the selected structures are relatively close to each other, they are expected to experience comparable weather conditions. This helps the current study evaluate the patterns of structural response and extend the findings to other similar structures. The long-term monitoring of the structures includes the main truss panels and two support posts. Each truss panel consists of four main chords and several internal members. All the internal members, i.e., vertical, horizontal, and interior diagonal, are made of standard steel pipes with an outer diameter of 3 in. (1 in. = 0.0254 m). The main chords consist of extra-strong steel pipes with an outer diameter of 5 in. The post supports are 31 ft. (1 ft. = 0.3048 m) tall and made of HSS pipes with an outer diameter of 14 in. and a thickness of 0.5 in. The side panel trusses are made of extra strong steel pipes with an outer diameter of 3 in. The main horizontal truss consists of three prefabricated trusses, which are 25, 30, and 25 ft. (total 80 ft.) long for Truss A and 30, 30, and 30 ft. (total 90 ft.) long for Truss B, respectively. The entire horizontal truss is supported with a saddle assembly placed on W10×45 beams at two ends. The top truss ends are connected to the support posts by using stainless U-bolts. The support posts are welded to the base plates. A bolted connection is used to attach the base plates to the foundation.

#### *4.1.2. Monitoring system setup*

Campbell Scientific CR1000 has been used to record data from vibrating-wire gauges. The sampling rate of the recording system is one every hour. A total of 18 vibrating-wire gauges are used for the instrumentation of each truss. Among them, seven sensors have been installed on the middle truss panel, seven sensors have been installed on the side truss panel close to the highway shoulder, and four sensors have been installed at the bottom of the post supports. Figure 4.2 shows the instrumentation layout for both Truss A and B. Similar members have been selected from both trusses for instrumentation to make a direct comparison possible. In each panel, four out of seven sensors have been attached to the horizontal chord members (one for each chord) and the remaining three sensors have been attached to the diagonal members.

#### *4.1.3. Findings from long-term data*

One of the primary objectives of this study is to investigate the effect of diurnal temperature changes on the fatigue life of steel DMS-support structures. In order to evaluate such effects, the two structures have been monitored for close to one year to capture both hot and cold seasons. Figures 4.3 and 4.4 provide the strain and temperature time histories recorded by Sensor ID 3, 10, 5, and 12 for both structures in a hot and a cold month. A review of the data collected from all the installed sensors indicates that the strain time

histories follow a pattern similar to the temperature time histories and there is no abnormal value in the recorded values. For a detailed fatigue analysis of the two DMS-support structures under consideration, the temperature-induced strain time histories are first converted to the stress time histories using the Hook's law. Even though this direct conversion can carry some approximation, the percentage of error is negligible since the truss consists of long and hollow members with a small thickness. The rainflow cycle counting method is then utilized to count the number of stress range cycles. Finally, the Miner's rule (1945) is used for the calculation of the fatigue life of the two structures. With a special focus on the truss joints, the stress time histories obtained along the length of the truss members are used to derive the stress time histories at the joints. This is achieved by using a magnification factor to take into consideration the stress concentration effects. Based on the type of connection, the AASHTO Standard Specifications for Structural Supports for Highway Signs, Luminaires, and Traffic Signals (2015). reports the stress concentration factor (SCF). This factor is found to be 4.0 for the joints of the two case-study trusses (2015). Using the magnified stress time histories, the number of cycles for various stress ranges are obtained for the fatigue analysis of the truss joints. Figure 4.5 presents the histograms of the stress ranges and their respective number of cycles for four sensor/joint locations selected from each structure. As it is illustrated in the developed histograms, some of the cycles are higher than constant amplitude fatigue threshold (CAFT), which is 4500 psi for the slotted tube to gusset plate connection (2015). This indicates that the concern of experiencing a high level of fatigue-induced damage from diurnal temperature changes exists for this category of structures.

In addition to the strain time histories, the temperature time histories must be investigated to further correlate the effects of diurnal temperature changes to the strains and stresses induced in the two structures. Figure 4.6 provides an overview of the maximum, minimum, and averaged temperature time histories for one hot and one cold month. Based on the recorded data, a temperature range between 20 °F and 110 °F is experienced by each of the two trusses. Based on the data collected from the field, Figure 4.7 provides detailed information about the correlation of strain, temperature, and time of the year for Truss A and B. This figure confirms the correlation between the strain change and temperature.

#### **4.2. Numerical modeling**

In addition to the field study, detailed FE models of the DMS-support structures have been generated in the Abaqus software package to extend the scope of investigations beyond what can be captured in the field. The numerical simulations are conducted, particularly to obtain an in-depth understanding of the response of this category of structures under temperature-induced stresses and predict their potential vulnerability to fatigue-induced damage. In the developed FE models, shell elements are used for the truss members and gusset plates. This provides the details necessary to capture stress concentrations at the joints. Figure 4.8 demonstrates the orthogonal projection of the FE model of Truss A together with a close view of a typical truss member. After an extended sensitivity analysis, the mesh size and pattern have been decided in such a way that the connection details are captured, while the overall efficiency of the FE simulations is maintained. Since the main objective of this numerical study is to identify the truss members (and their joints) most vulnerable to temperature-induced stresses, a temperature change is applied to the FE

model in 10 F increments. The strains and stresses at the most critical locations are then obtained for a fatigue analysis.

To validate the FE models developed to investigate the structural response of the DMS-support trusses, the temperature time histories averaged from the temperature time histories obtained from the individual sensors are applied to the FE models. A coupled thermal-stress analysis is performed to calculate the strains and stresses in the truss members under the temperature profiles similar to what they experience in the field. Figure 4.9 compares the strain time histories obtained during the field study (from March 15th to March 31st) with the ones extracted from the FE model of Truss A. The members in the same location are selected from both middle and side truss panels to evaluate the consistency of results. Based on Fig. 4.9, the strain time histories derived from the FE model follow a trend very close to the temperature time histories recorded at the corresponding sensor locations in the field. Considering that temperature time histories are input to the FE models, it is observed that the generated models can simulate the overall structural response well. This, however, does not necessarily include all the details of the strain time histories recorded by the sensors. This can be attributed to the data collection strategy used in the field monitoring program to avoid unnecessary large data files. The sample rate of data collection has been set to one every hour, mainly because no drastic change in the temperature is normally anticipated within one hour. In addition, it must be noted that there can be other sources of excitation, which cause low-cycle noises. Such noises are, however, believed not to have a major influence on the fatigue life of the structures, as they produce low-cycle stress ranges. Considering that the number of cycles for each stress range is needed for a fatigue analysis, it is essential that the FE simulations deliver the cycles of strain and stress similar to the actual cycles that the DMS-support structures experience in the field. Figure 4.10 illustrates the results of rainflow cycle counting for the simulation and actual strain time histories. A review of the results shows that the number of cycles associated with the first strain range is not fully consistent between the simulation and field data. This was expected because the high-cycle, low-range noises are not captured in the numerical simulations. For the other strain ranges, however, there is a close agreement between the numbers of cycles. This indicates that the generated FE model can successfully simulate both range and number of cycles of strain and stress, which are critical for fatigue analysis.

### 4.3. Fatigue analysis

For the fatigue analysis of the DMS-support structures under diurnal temperature changes, the stress life method has been utilized in the current study. This method is based on the  $S-N$  curves, which represent the relation between the stress range and the number of cycles. The general equation of  $S-N$  curves can be expressed as:

$$\log N_i = \log A - 3 \log S_i \quad (4.1)$$

where  $N_i$  is the number of cycles needed to cause failure at the  $i$ -th stress range,  $S_i$  is the corresponding stress range, and  $A$  is a constant value determined based on the connection details. The AASHTO Specifications (2015) provides a table that includes the  $A$  value for various types of connections used in sign-support structures. In the current study, the type

of connection used in the two trusses is a slotted tube to gusset plate connection with the coped hole, which falls in the *E* category. Based on the AASHTO Specifications (2015), the connection zone, particularly the areas close to the weld between the pipe and the gusset plate, are the most critical parts prone to fatigue-induced cracks.

Based on the Miner's rule, the damage resulted from a specific stress range can be expressed as:

$$D_i = \frac{n_i}{N_i} \quad (4.2)$$

where  $D_i$  is the fatigue damage caused by the stress range  $S_i$ ,  $n_i$  is the number of cycles of the stress range  $S_i$ , and  $N_i$  is the number of cycles needed to cause failure at the  $i$ -th stress range. The  $N_i$  is obtained from Equation 1. On the other hand,  $n_i$  is determined from the rainflow cycle counting of the stress time histories. Once the damage for each specific stress range, i.e.,  $S_i$ , is found, the total damage,  $D$ , can be estimated using  $D = \sum D_i$ . Based on the Miner's rule, if the total damage,  $D$ , becomes equal to 1.0, failure is expected to occur.

The fatigue analysis has been conducted on the data collected from the field, as well as the ones obtained from the numerical simulations. Using the stress ranges and cycles obtained from the field data (as illustrated in Fig. 4.5), the fatigue life of all the instrumented truss members is found to be infinite. A similar procedure is used for the fatigue life calculation using the FE models, which provide the flexibility of going beyond the instrumented truss members. There are two alternatives for calculating the fatigue life based on the result of the numerical simulations: The first alternative is to apply the actual temperature time history to the FE model and find the stress time histories at critical locations by conducting a coupled thermal-stress analysis. This procedure, however, is computationally expensive because of the duration of the temperature time history that needs to be applied to the structure step-by-step. The second alternative, which has been employed in the current study, includes the following steps for calculating the fatigue life: (1) The rainflow cycle counting is performed on the averaged temperature time histories and the number of cycles for each temperature range is derived, (2) The derived temperature ranges are applied to the FE model and a coupled thermal-stress analysis is conducted, and (3) The stresses generated in the truss elements due to each temperature range are obtained and then further employed for the fatigue life calculations. Further to computational efficiency, the second alternative is believed to provide acceptable results considering that the stress ranges have the same number of cycles as the temperature ranges.

Figure 4.11 shows the total number of cycles for the entire duration of monitoring for both Truss A and B. Based on this figure, the number of cycles in each temperature range is consistent for both trusses, which confirms that both of them experience similar weather conditions. A review of the recorded cycles indicates that more than 97% of them are associated with the temperature ranges less than 50 °F, which is known to be representative of the expected diurnal changes in most of the United States. The outcome of the fatigue analysis using the results obtained from the numerical simulations for Truss A has been

summarized in Table 4.1. This table shows that the fatigue life of Truss A is  $\frac{1}{7.27E-04} = 1375$  years, which can be deemed equivalent to infinite.

#### 4.4 Comparison of steel and aluminum DMS-support structures

Considering the recent transition from aluminum to steel DMS-support structures, the current study provides a unique opportunity to investigate the role of materials in the fatigue life of this category of structures under temperature-induced stresses. For this purpose, the two steel DMS-support structures under consideration are compared with an aluminum DMS-support structure, which has been in service in the same geographic area. The fatigue life assessment of the aluminum DMS-support structure has been performed by Chang et al (2014). For comparison purposes, an analytical approach is employed to find the fatigue life of a representative truss element with steel and aluminum materials. To complete the calculations, the following assumptions have been made: (1) Both structures experience the same diurnal temperature changes; and (2) The fatigue is induced by only diurnal temperature changes and other sources of excitation are neglected.

Using the Hook's law, the thermal stress can be found from  $\Delta\sigma = E\alpha\Delta T$ , where  $\Delta\sigma$  is the stress change,  $E$  is the modulus of elasticity,  $\alpha$  is the linear coefficient of thermal expansion, and  $\Delta T$  is the temperature change. Using this equation, the ratio of the stress change in an aluminum with respect to a steel truss element can be stated as:

$$\frac{\Delta\sigma_{AL}}{\Delta\sigma_{ST}} = \frac{E_{AL}\alpha_{AL}}{E_{ST}\alpha_{ST}} \quad (4.3)$$

where  $\Delta\sigma_{AL}$  and  $\Delta\sigma_{ST}$  are the stress range of the aluminum and steel structure,  $E_{AL}$  and  $E_{ST}$  are the modulus of elasticity of aluminum and steel, and  $\alpha_{AL}$  and  $\alpha_{ST}$  are the coefficient of thermal expansion of the aluminum and steel structure, respectively. Since the ratios of  $\frac{E_{AL}}{E_{ST}}$  and  $\frac{\alpha_{AL}}{\alpha_{ST}}$  can be assumed equal to  $\frac{10^7 \text{ psi}}{2.9 \times 10^7 \text{ psi}} = 0.34$  and  $\frac{24 \times 10^{-6} (1/K)}{12 \times 10^{-6} (1/K)} = 2$ , respectively, the ratio of the stress change in Equation 3 is found to be 0.69. It must be noted that this ratio is in fact equivalent to  $\frac{S_{AL}}{S_{ST}}$ , which is needed for fatigue life assessment in Equation 1.

Based on the AASHTO Specifications (2015), the ratio of the constant value of  $A$  for the connections of an aluminum with respect to a steel truss element is equal to 0.2. This is because of the tube to tube connections used in the aluminum and the slotted tube to gusset plate connection in the steel DMS-support structures. Using the  $S-N$  curves, the ratio of the cycles needed to cause a fatigue-induced failure for an aluminum with respect to a steel structure can be obtained from:

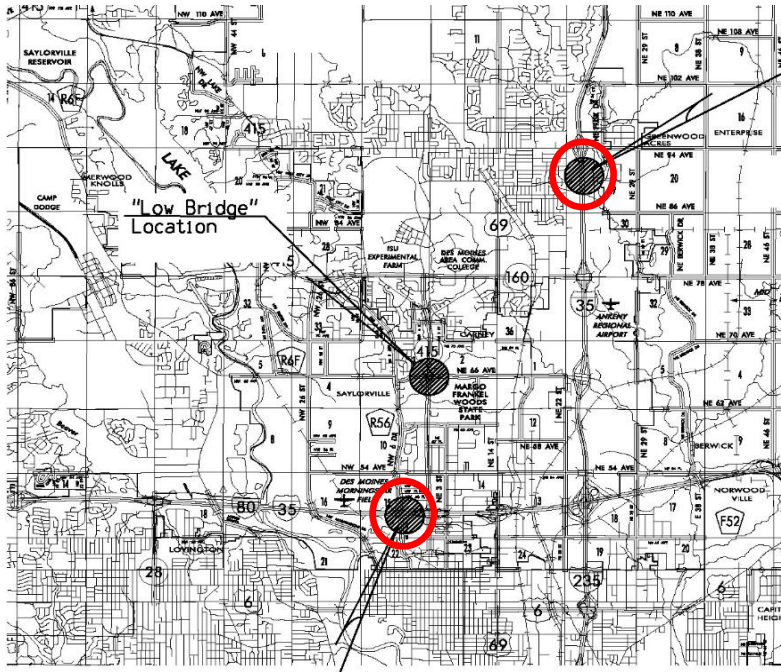
$$\frac{N_{AL}}{N_{ST}} = \left(\frac{S_{ST}}{S_{AL}}\right)^3 \left(\frac{A_{AL}}{A_{ST}}\right) = \left(\frac{1}{0.69}\right)^3 (0.2) = 0.61 \quad (4.4)$$

The ratio of the fatigue-induced damage in an aluminum with respect to a steel structure can be derived using the following equation:

$$\frac{D_{AL}}{D_{ST}} = \left( \frac{N_{ST}}{N_{AL}} \right) \left( \frac{n_{AL}}{n_{ST}} \right) \quad (4.5)$$

where  $\frac{n_{AL}}{n_{ST}}$  is the ratio of the number of the stress range cycles of an aluminum with respect to a steel structure. In this case, the number of stress range cycles is equal to the number of temperature range cycles. As it is assumed that both structures are in similar weather conditions, they experience the same number of temperature (and as a result stress) range cycles. Thus,  $\frac{n_{AL}}{n_{ST}}$  is equal to 1.0, and the ratio of the fatigue-induced damage is found to be 1.64 in Equation 5. This demonstrates that the expected damage to the new steel DMS-support structures with a slotted tube to gusset plate connection detail is 64% less than that of existing aluminum DMS-support structures with a tube to tube connection detail.

Further to the fatigue performance assessment of individual aluminum and steel truss elements, the fatigue life comparison can be extended to the entire structure. The correlation between the temperature and stress ranges derived from the FE models of the aluminum and steel structures is shown in Figure 4.12. Using this figure, the stress ranges for the most critical truss joints are obtained for fatigue analysis. The outcome of fatigue life analysis on the most critical joint of the aluminum DMS-support structure has been provided in Table 4.2. Consistent with Chang et al. (2014), the fatigue life of  $\frac{1}{2.30E-02} = 44$  years is obtained from this analysis. A direct comparison between the two materials shows that the fatigue life of the aluminum structure is significantly less than that of the steel structure, despite the fact that the stresses that the steel structure experiences are consistently higher than those experienced by the aluminum structure. This is completely in line with the findings from the analytical study performed on both materials.



*DMS "1st street"  
I-35 NB (Truss*

*DMS "2nd Ave."  
10 WB (Truss A)*

Figure 4.1. Location of two steel DMS-support structures under consideration through a long-term field monitoring program.

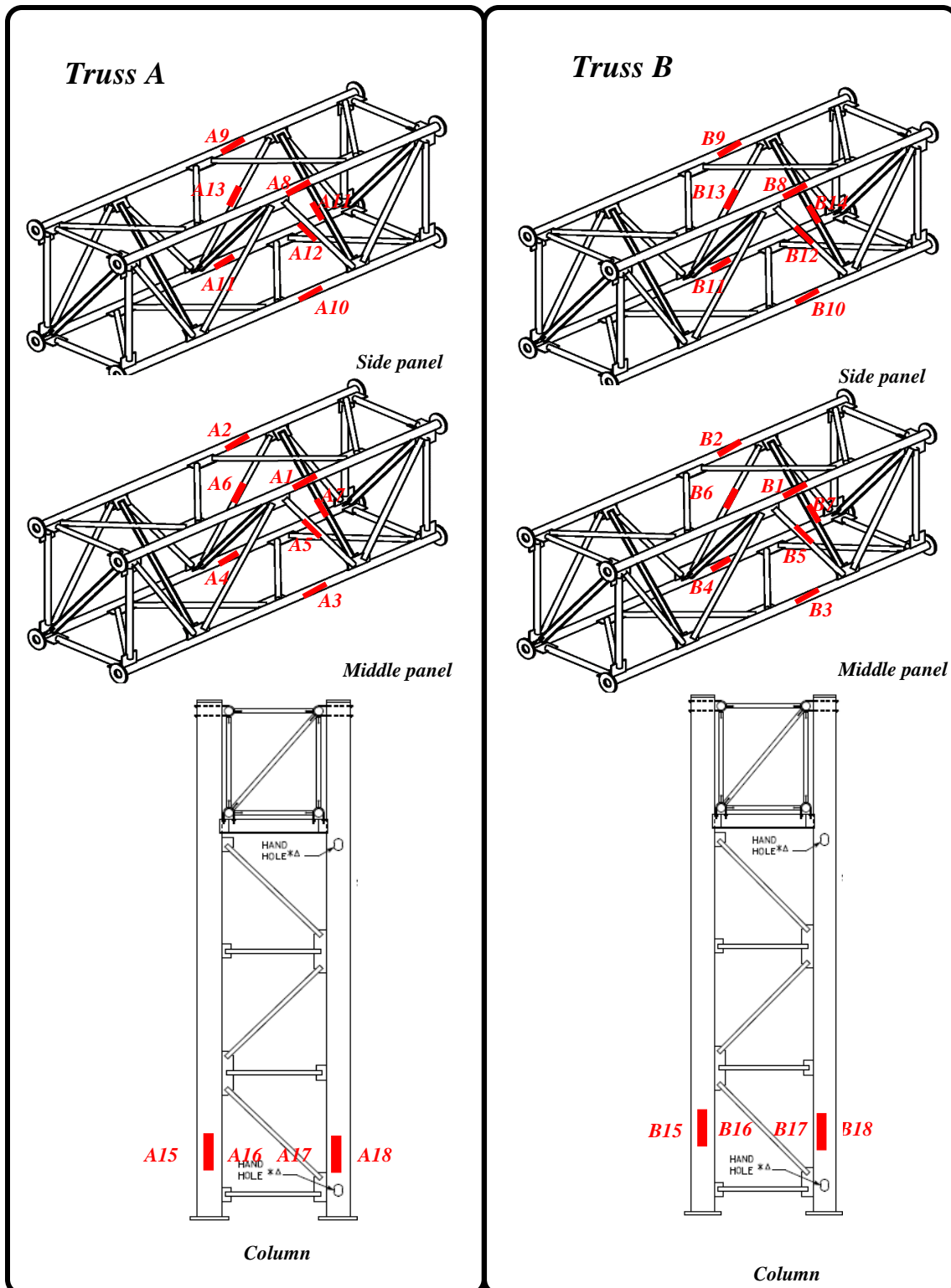


Figure 4.2. Instrumentation layout used for Truss A and B.

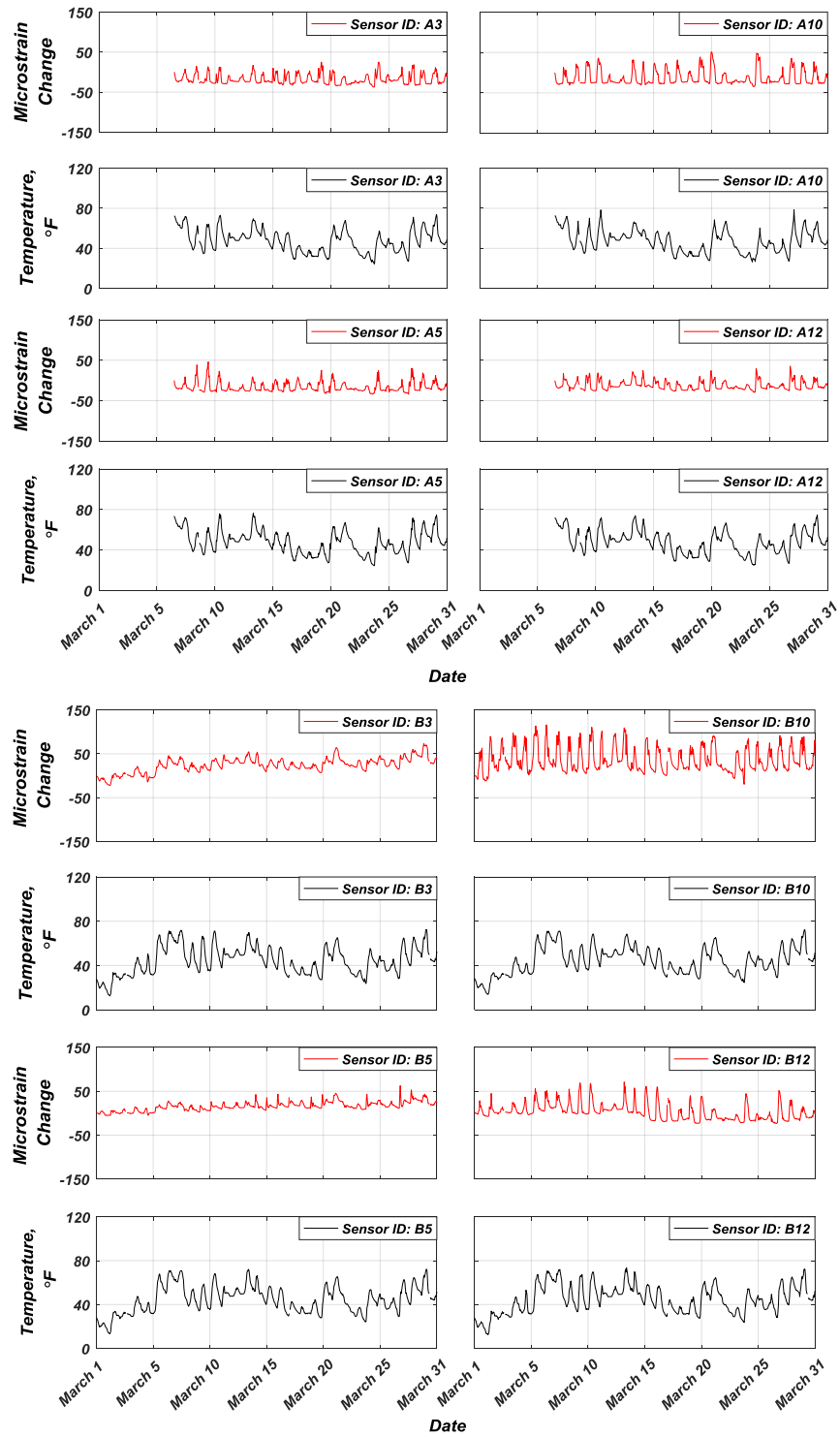


Figure 4.3. Strain and temperature time histories obtained from Truss A and B during a cold month.

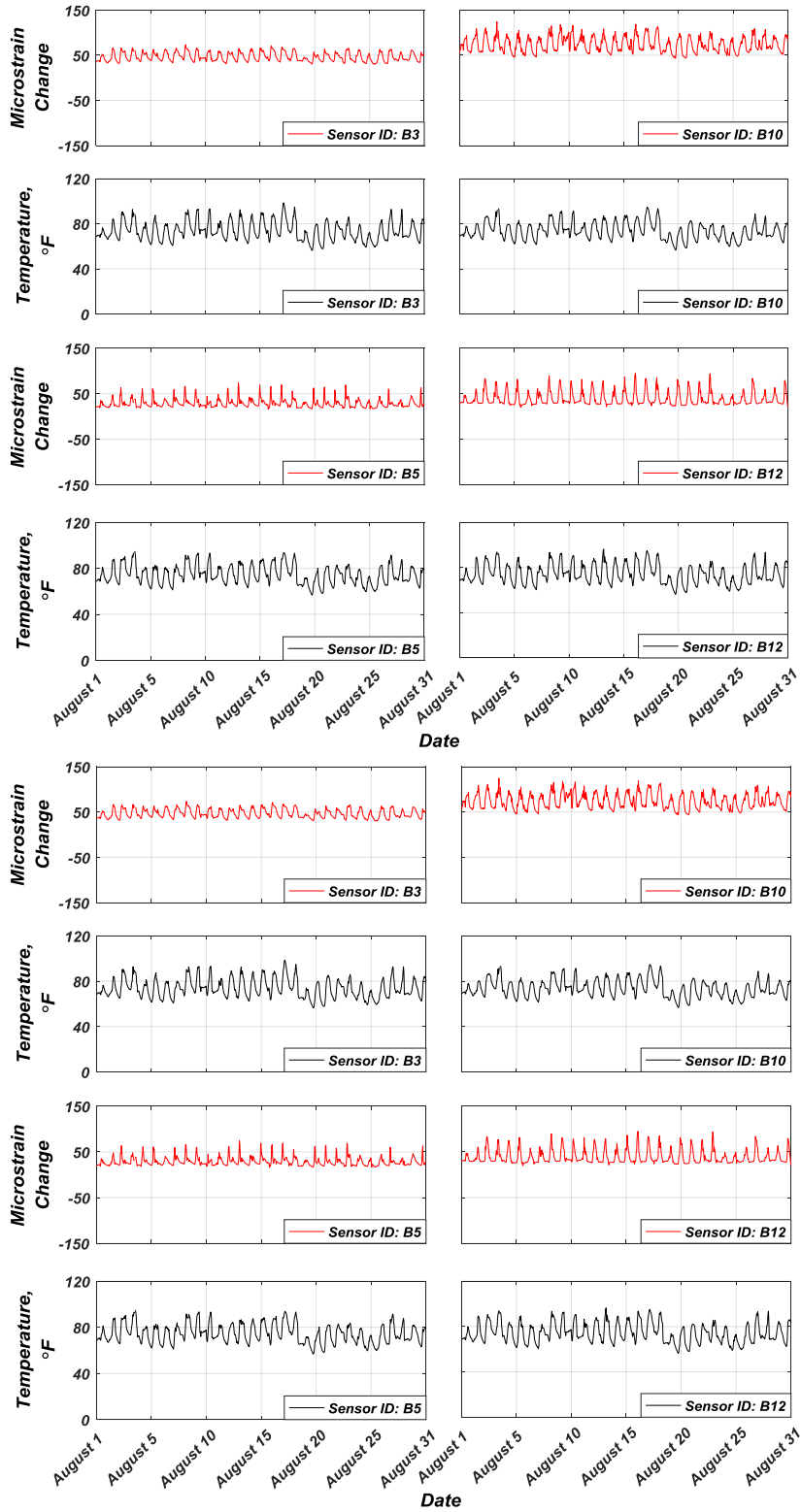


Figure 4.4. Strain and temperature time histories obtained from Truss A and B during a hot month.

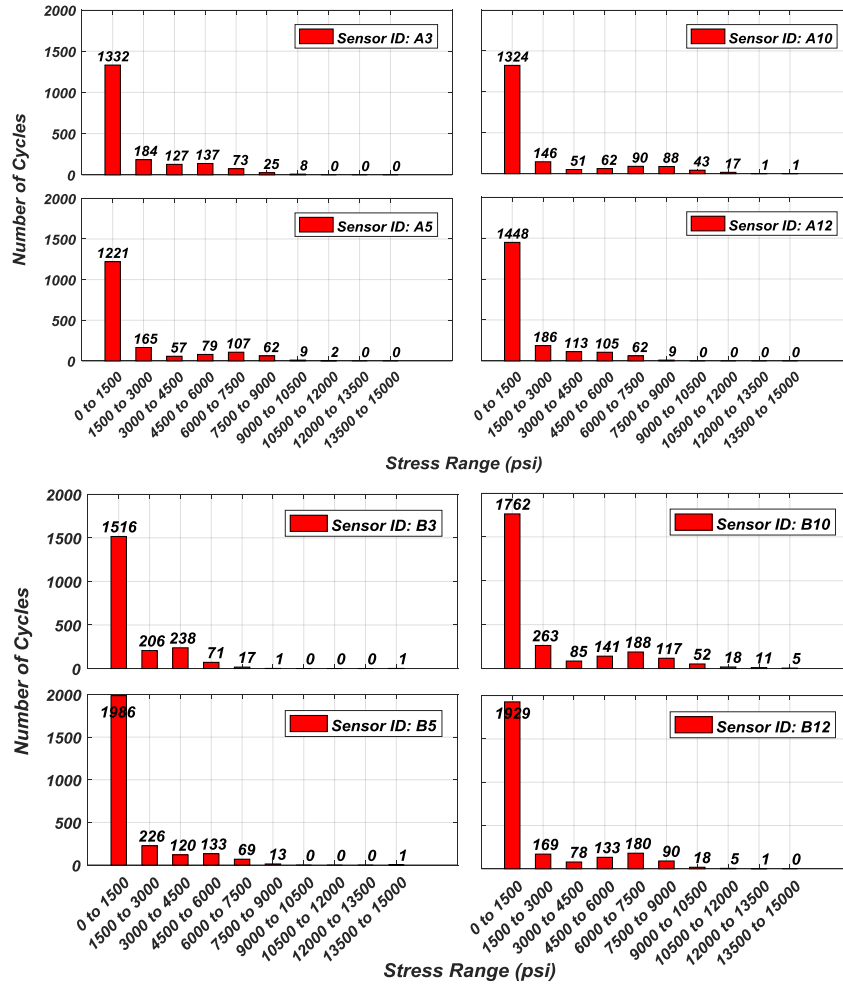


Figure 4.5. Stress ranges and their respective cycles for a set of sensor locations from Truss A and B.

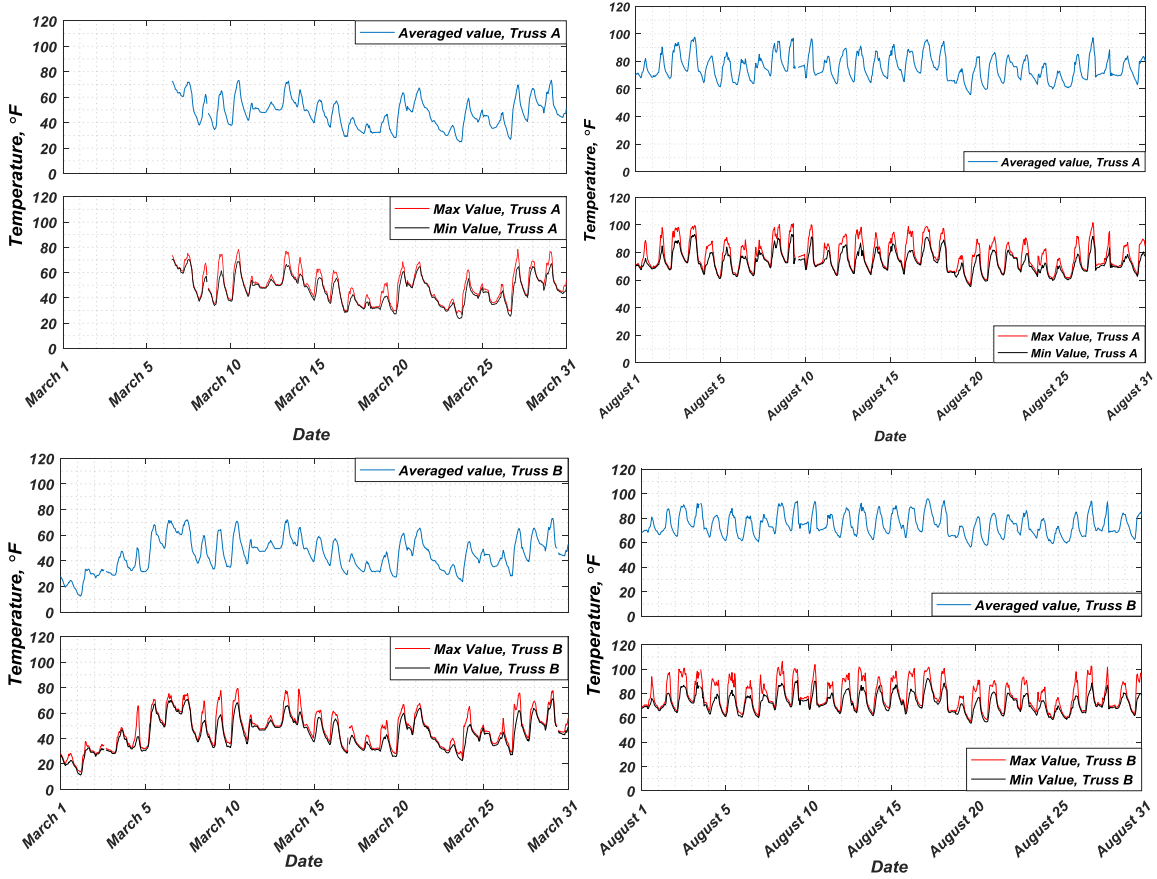


Figure 4.6. Averaged, maximum, and minimum value of temperature time histories recorded in each truss structure during a one-year period.

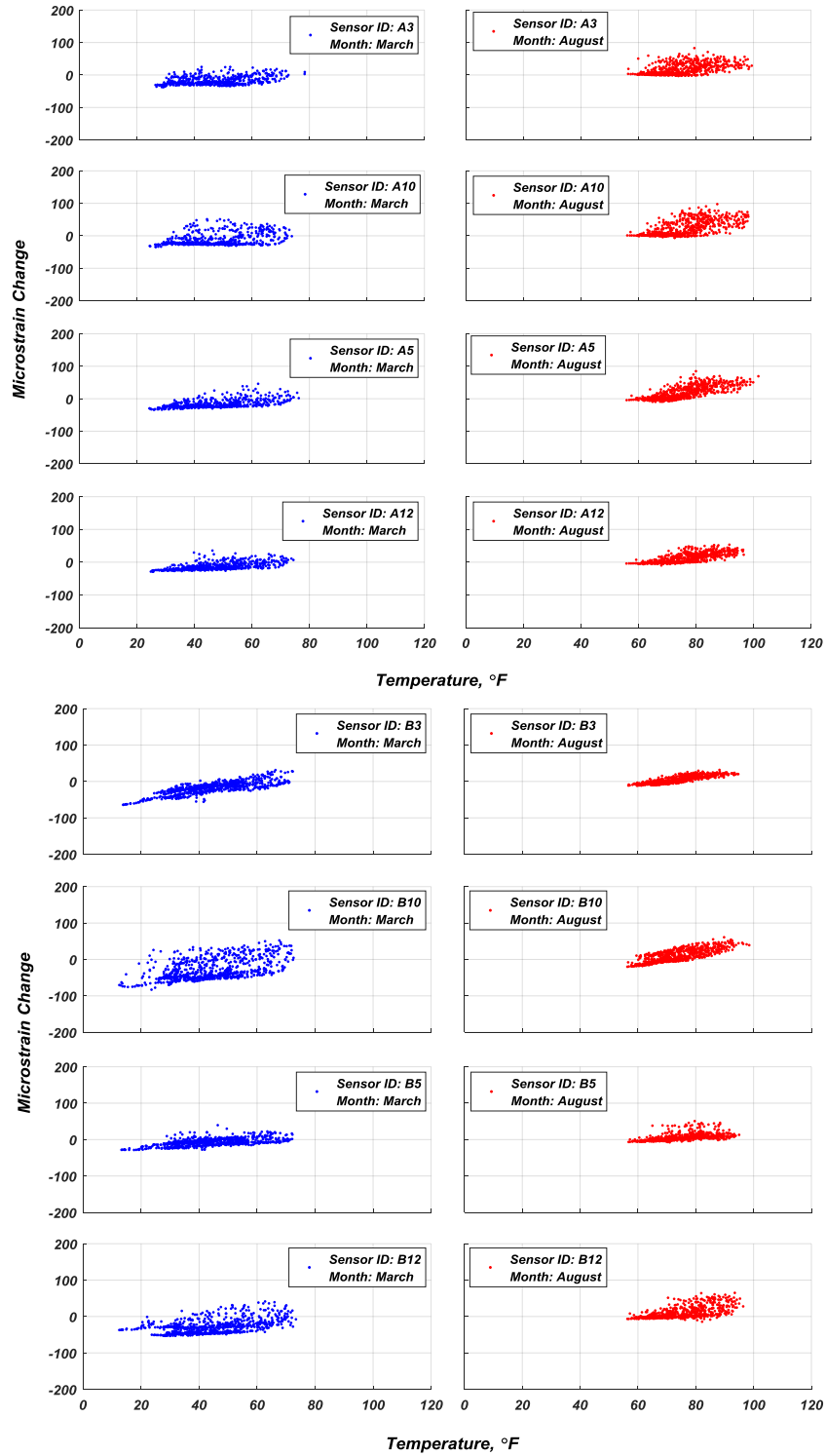


Figure 4.7. Correlation of strain change, temperature, and time of data collection for selected sensors from Truss A and B.

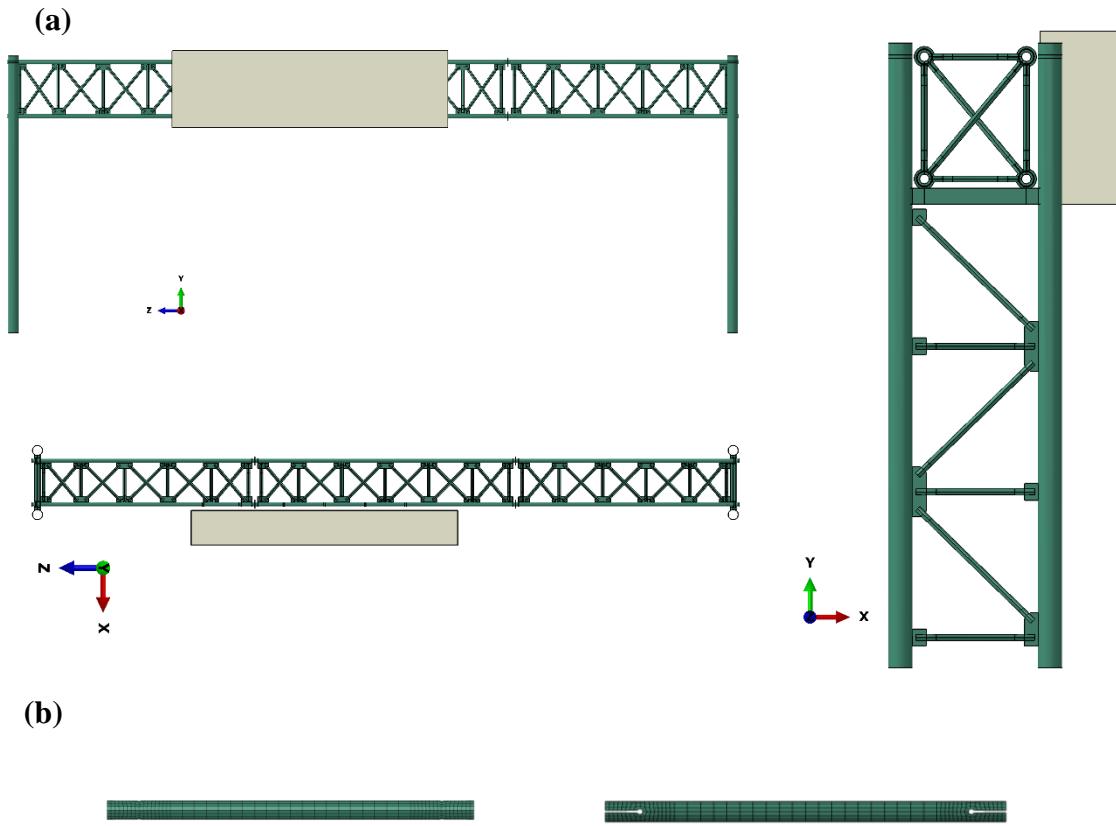


Figure 4.8. Details of the FE models of the sign-support structures generated for numerical simulations.

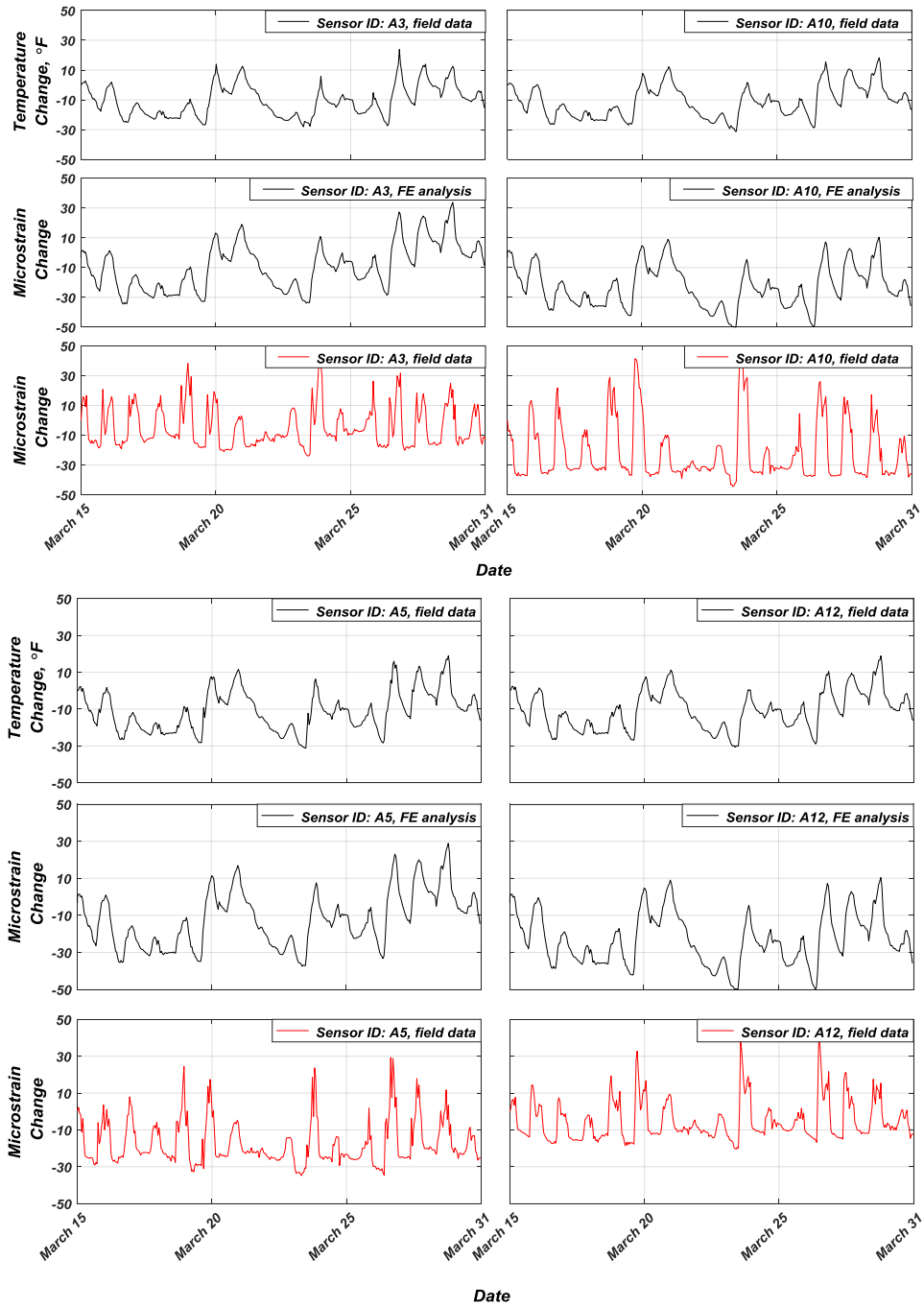


Figure 4.9. Comparison of strain time histories obtained from the FE model and during the field study.

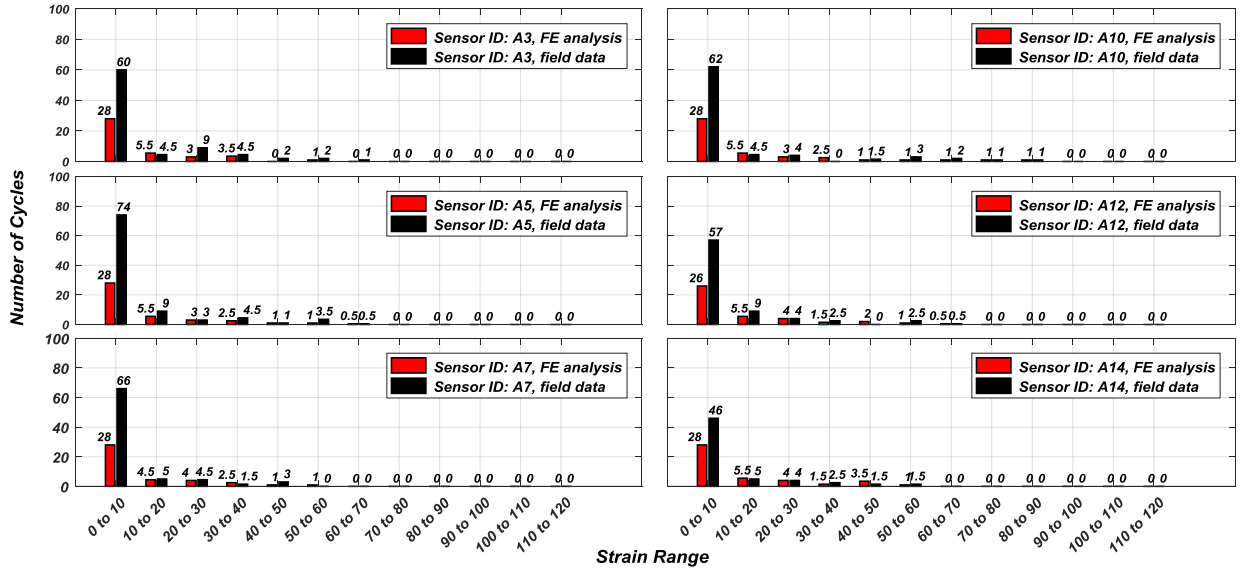


Figure 4.10. Rainflow cycle counting of actual and finite element model simulated strain time histories.

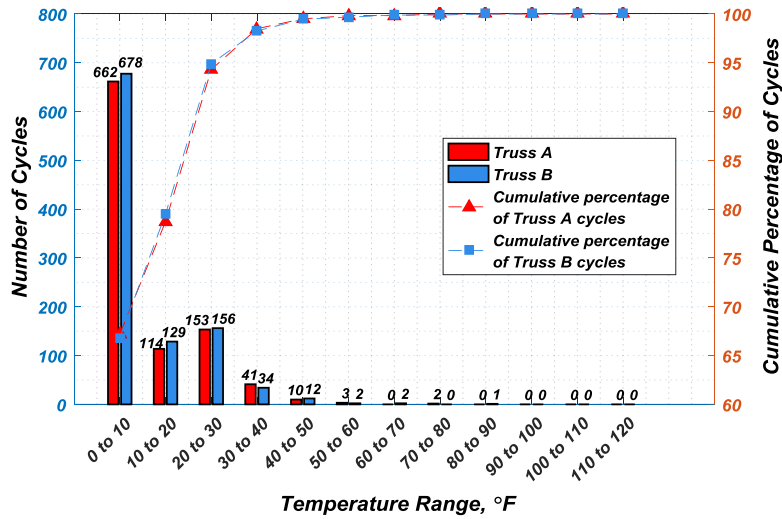


Figure 4.11. Summary of rainflow cycle counting results.

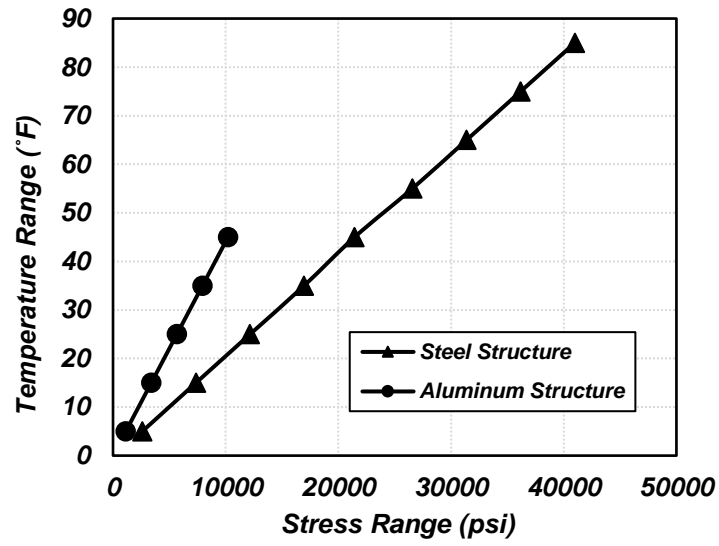


Figure 4.12. Correlation between temperature range and the stress range derived from the FE models of steel and aluminum DMS-support structures.

Table 4.1. Fatigue analysis results of Truss A.

Temperature range (F)	No. of cycles	Stress range (ksi)	$N_f$	$D$
5	662	2.6	6258534 4	1.06E-05
15	114	7.4	2714548	4.20E-05
25	153	12.3	591122	2.59E-04
35	41	17.1	219991	1.86E-04
45	10	21.5	110682	9.03E-05
55	3	26.7	57791	5.19E-05
65	0	31.5	35193	0
75	2	36.3	22997	8.70E-05
85	0	41.0	15960	0
sum = 985				Sum = 7.27E- 04

Table 4.2. Fatigue analysis results of the aluminum DMS-support structure.

Temperature range (F)	No. of cycles	Stress range (ksi)	$N_f$	$D$
5	6	1.1	773456 6	7.76E-07
10	6	2.3	791053	7.58E-06
15	27	3.4	208429	1.30E-04
20	42	4.5	80905	5.19E-04
25	51	5.7	38832	1.31E-03
30	87	6.8	21317	4.08E-03
35	78	7.9	12838	6.08E-03
40	33	9.1	8275	3.99E-03
45	30	10.2	5617	5.34E-03
50	6	11.3	3972	1.51E-03
Sum = 366				Sum = 2.30E- 02

## 5. Summary, conclusions and recommendations for future work

Dynamic Message Signs (DMS) have been increasingly used on freeways, expressways, and major arterials to better manage the traffic flow by providing accurate and timely information to motorists. Overhead truss support structures are typically employed to support those DMS cabinets allowing the DMS cabinets to provide wider display to further lanes. The structural performance assessment of the overhead truss structures that support such DMSs has become a subject of interest for those working on the design and maintenance of transportation infrastructure components. There are a few studies available in the literature related to this type of structures. In order to predict the behavior of a highway overhead truss structure, detailed understanding of the wind loads on the traffic sign and the truss structure supporting it and the response of the structure are necessary. Moreover, most existing efforts neglect the potential contribution of thermal stresses that can cause damage to the truss structures, particularly at their joints. It is well known that a large temperature range may generate unexpected high (thermal) stresses on the structures, especially where stress concentration occurs due to geometric discontinuities. Several *National Cooperative Highway Research Program* (NCHRP) studies have been focused on fatigue failure of truss structures but few truss structures were tested to understand the thermal response. In addition, contribution of stresses induced during transportation from the fabricator to the site is also largely unknown. Fabrication may play an important role in the development of fatigue cracks. Another probable cause for fatigue damage are the cyclic oscillations of the total wind load associated with the vortex shedding behind the DMS cabinet at high wind conditions. A resonance condition, causing large amplitude relatively steady vibrations of the support trusses can occur if the frequency of shedding coincides with a natural vibration frequency of the DMS cabinet.

In the first part of the study, state-of-the-art 3D numerical simulations of airflow around traffic signs were conducted to accurately determine drag coefficients for traffic signs of different shapes and how these coefficients vary with the main geometrical parameters (sign aspect ratio, ground clearance ratio). An advanced turbulence methodology called Detached Eddy Simulation (DES) that directly resolves the large-scale turbulence in the flow was used to calculate the wind loads and to estimate the temporal evolution and mean value of the drag coefficient. This is essential to be able to accurately capture the vortex shedding behind the signs and the pressure distributions on the sign's surfaces needed to estimate the time history of the drag force acting on the sign. This part of the study focused on DMS cabinets but results were also provided for several types of thin traffic signs. DES simulations performed as part of the present study predicted drag coefficients of 1.4-1.5 for thin rectangular signs and DMS cabinets with aspect ratios between 3 and 4. Moreover, the predicted range of the drag coefficient for rectangular signs attached to trusses was very close to the one (1.39-1.47) predicted in the wind tunnel experiments conducted by Letchford (2001) and the one (1.3 to 1.5) predicted in the wind tunnel experiments of Warnitchai et al. (2009) for the case of single panel thin rectangular billboards at high angle of attack. Meanwhile, the ASCE/SEI 7-10 recommendations for the design of aluminum sign structures recommend the use of even higher values (1.7-1.8). For the same cases, the drag coefficient calculated based on the AASHTO standard ranges between 1.14 and 1.19, which is lower than the values predicted by the simulations conducted in the present study

as well as by most experimental studies. This is an important conclusion from this part of the study. This leads to a recommendation from the present study to increase the mean drag coefficient values in the AASHTO standard by about 25%. Another recommendation supported by the findings of the present study is that AASHTO should provide more information on how the drag coefficient of the traffic sign varies with the shape of the sign and other geometrical parameters affecting the value of the wind loads.

Another significant contribution of this part of the study is that the CFD analysis performed generates time series of the wind forces acting on the traffic signs. Using this force-time history as input it was possible to perform a dynamic analysis of the support structures to directly investigate if vibrations induced by vortex shedding behind the sign can be a main contributor to fatigue failure. Simulation results showed that the temporal variation of the total pressure force on the sign is subject to relatively low frequency (vortex-shedding induced) oscillations in addition to the higher frequency ones associated with small-scale turbulence. Using this information on the unsteady wind loads the performance of test mitigation devices for reducing or eliminating wind-induced vibrations of support structures for highway signs can be tested.

Steady RANS simulations were also conducted to calculate individual drag forces on the members of a truss supporting a DMS cabinet. Then, using the projected area, the drag coefficient for each member was directly estimated. The study found that the drag coefficients were larger than 1.2 for the members situated in the region where the flow is accelerated as it passes the sign attached to the truss and that some of the shielded members had non-negligible drag coefficients in the 0.3-0.5 range. Using data from additional representative test cases, these results can lead to the development of a new methodology to estimate wind loads on the members of the structures supporting highway signs. Future work should focus on developing recommendations on how to split the support structure into different regions and give values of the drag coefficients to be used for the unshielded and shielded members within these regions. These recommendations can replace present procedures to estimate wind loads on trusses used by the state DOTs that are not easy to implement, fairly simplistic and subject to large errors.

In the second part of this study, a comprehensive field study paired with detailed numerical simulations were conducted on a four-chord sign support structure during transportation from the fabricator to the installation site to investigate the damage severity induced during the transportation of these trusses. For the field study, 12 strain gauges were mounted on various truss members and a short-term structural health monitoring was completed. Further to the field study, a detailed finite element (FE) model of the same truss was generated using the ABAQUS package to evaluate the distribution of strains and stresses within the entire truss members. To investigate the effects of road roughness on the potential of experiencing fatigue-induced damage, three artificial road profiles were generated following the ISO guidelines. To capture the vibrations transferred to the truss structure when it was being shipped by the truck, a quarter car suspension system was designed and the Simulink package was used to solve the corresponding partial differential equations of motion. The time-history of vertical vibrations at the truss supports were used as input to the detailed FE model of the truss generated in the ABAQUS package.

Following a set of numerical simulations for various road surface conditions, the stress time histories were obtained and the SCFs were estimated. This was one of the unique contributions of the current study, which highlights how the actual SCFs are compared with the constant value reported in the AASHTO Specifications. A fatigue analysis was then conducted using both the field data and simulation results. While the potential of experiencing fatigue-induced damage changes from one truss member to the other, it was shown that the predictions obtained from the developed computational framework is in a close agreement with the observations from the field in terms of identifying the most vulnerable elements as well as the percentage of fatigue damage during transportation.

A comprehensive field study paired with detailed numerical simulations was conducted on two overhead DMS support structures located in Iowa to evaluate the damage induced by the change of temperature in the regions that experience large diurnal temperature fluctuations. The case-study structures are unique because while they are close to each other and experience similar environmental conditions, one is in the north-south and the other is in the east-west direction. This helps to investigate sunlight as a factor contributing to potential damage. In the second phase of the study, two DMS support structures have been instrumented using a total number of 18 vibrating wire sensors for a long term structural health monitoring. In addition to the field study, FE model of one of the structures has been developed using ABAQUS to further investigate the potential thermal induced damages and localize the vulnerable members. This part of the study has two main contributions: (1) Fatigue life analysis of steel overhead DMS support structures using field data and results of finite element analysis. (2) Comparison fatigue performance of an aluminum overhead DMS support structure with tube to tube connections details with steel overhead DMS support structure with slotted tube to gusset plate connection detail. Analyzing the field data showed that both steel structures has the infinite fatigue life. Moreover, fatigue life calculated using the result of finite element simulation also indicated that the fatigue life the structure is infinite.

The fatigue performance of the steel structure was compared with that of aluminum structure using Analytical approach. Based on this analysis, it was demonstrated that a 1-D linear element of steel structure experiences approximately 64% more stresses than an aluminum one. However, the steel structure has roughly 30% more fatigue life comparing aluminum structure. In addition to analytical approach, a direct comparison has been also done between two structures. For this comparison, the environmental condition of steel structure has been applied to the aluminum structure the fatigue performance of the aluminum structure compared with the steel structure. The outcome of this comparison indicated that the steel structure has a highly better fatigue performance. Finally, comparing two different cycle counting method, i.e. rainflow and daily cycle counting methods, it is concluded that daily cycle counting method will underestimate the fatigue life and rainflow cycle counting method should be used for the fatigue analysis.

It is recommended that future trusses be constructed using steel members with connection details similar to those studied here. Previously utilized connection details coupled with aluminum members show notable fatigue issues. It is also recommended that additional monitoring of trusses during transportation be conducted with the goal of developing best

practices for transporting these trusses. The present study identified that a disproportionate percentage of fatigue life was used during transportation. Other anecdotal evidence illustrates that in some cases 100% of fatigue life has been used resulting in cracked members upon delivery. The apparent main contributing factor appears to be the means and method of securing the truss during transportation. The development of a best practices guide would represent an important step in ensuring that upon installation trusses are in the best possible condition.

## References

- AASHTO (2015), *LRFD Standard specifications for structural supports for highway signs, luminaires, and traffic signals* (Sixth Edition), American Association of State Highway and Transportation Officials, Washington, D.C.
- Agostinacchio, M., Ciampa, D. and Olita, S. (2014), *The vibrations induced by surface irregularities in road pavements – a Matlab® approach*, Eur. Transp. Res. Rev., Vol. 6, No. 3, 267–275.
- Alexandru, C., and Alexandru, P. (2011), *A comparative analysis between the vehicles' passive and active suspensions*, Int. J. Mech., Vol. 5, No. 4.
- Andren, P. (2006), *Power spectral density approximations of longitudinal road profiles*, Int. J. Veh. Des., Vol. 40, No. 1/2/3, 2-18.
- Arabi, S., Shafei, B., and Phares, B. (2017), *Vulnerability assessment of sign support structures during transportation*. Compd. Transp. Res. Board, 1-15.
- ASCE, *Minimum design loads for buildings and other structures*, ANSI/ASCE 7-10, ASCE, New York, 2010.
- ASTM E 1049-85. (2011), *Rainflow Counting Method*.
- Barbosa, R. S. (2011), *Vehicle dynamic response due to pavement roughness*, J. Brazilian Soc. Mech. Sci. Eng., Vol. 33, No. 3, 302–307.
- Barle, J., Grubisic, V. and Vlak, F. (2011), *Failure analysis of the highway sign structure and the design improvement*, Eng. Fail. Anal., Vol. 18, No. 3, 1076–1084.
- Chang, B., Phares, B. M., Sarkar, P. P., and Wipf, T. J. (2009), *Development of a Procedure for Fatigue Design of Slender Support Structures Subjected to Wind-induced Vibration*, Transportation Research Record: Journal of the Transportation Research Board, No. 2131, TRB, National Research Council, Washington, D.C., 23-33.
- Chang, B., Sarkar, P. P., and Phares, B. M. (2010), *Time-Domain Model for Predicting Aerodynamic Loads on a Slender Support Structure for Fatigue Design*. The ASCE Journal of Engineering Mechanics, Vol. 136, No. 6, 736-746.

- Chang, B., Phares, B., Sarkar, P. and Wipf, T. (2009), *Development of a Procedure for Fatigue Design of Slender Support Structures Subjected to Wind-Induced Vibration*, Transp. Res. Rec. J. Transp. Res. Board, Vol. 2131, 23–33.
- Chang, B., Phares, B., Zou, H. and Couch, T. (2014), *Thermal Analysis of Highway Overhead Support Structures*, Transp. Res. Rec. J. Transp. Res. Board, Vol. 2406, 32–41.
- Chavan, S. P., Sawant, H. and Tamboli, J.A. (2010) *Experimental Verification of Passive Quarter Car Vehicle Dynamic System Subjected to Harmonic Road Excitation with Nonlinear Parameters*, IOSR J. Mech. Civ. Eng., 2278–1684.
- Constantinescu, S.G., Bhatti, M.A., and Tokyay, T. (2007), *Improved method for determining wind loads on highway sign and traffic signal structures*, Final Report TR-559, Iowa Highway Research Board, Iowa DOT, IA
- Constantinescu, S.G., Bhatti, A., and Tokyay, T. (2008), *A numerical study of wind loads on large highway sign structures*, SEI 2008 Structures Congress, Vancouver, Canada, April 2008.
- Constantinescu, G., Bhatti, A., Wipf, T., and Phares, B. (2013), *Wind loads on dynamic message cabinets and behavior of supporting trusses*, Final Report TR-612, Iowa Highway Research Board, Iowa Department of Transportation, Ames, IA.
- Dodds, C. J., and Robson, J.D. (1973), *The description of road surface roughness*, J. Sound Vib., Vol. 31, No. 2, 175–183.
- Elson, J. M., and Bennett, J.M. (1995), *Calculation of the power spectral density from surface profile data*, Appl. Opt., Vol. 34, No. 1, 201-214.
- Fouad, H.F., Davidson, S.J., Delatte, N., Calvert, E., Chen, S., Nunez, E. and Abdalla, R. (2002), *NCHRP Report 494 – Structural Supports for Highway Signs, Luminaries, and Traffic Signals*. Washington, D.C., Transportation Research Board.
- Fouad, F. H., Davidson, J. S. et al. (2003), *Structural Supports for Highway Signs, Luminaires, and Traffic Signals*, NCHRP Report 494.
- Foutch, D. A., Rice, J.A., LaFave, J.M., Valdovinos, S., and Kim, T.W. (2006), *Evaluation of aluminum highway sign trusses and standards for wind and truck gust loadings*, Report No. FHWA/IL/PRR 153, Illinois Department of Transportation, Springfield, IL.
- Ginal, S. C. E. (2003), *Fatigue Performance of Full-Span Sign Support Structures Considering Truck-Induced Gust And Natural Wind Pressures*, Marquette University.
- Huckelbridge, A., and Metzger, A. (2007), *Investigation of the Dayton IR 75 Sign Truss Failure of 9/11/06*.
- Iyer, A. R., Venkatachalam, R. and Balaraju, A. (2007), *Analysis of Optimum Suspension Parameters of a Semi-Independently Suspended Automobile*, Int. J. Innov. Res. Sci. Eng. Technol. (An ISO Certif. Organ.), Vol. 3297, No. 5.
- ISO 8608 (1995), *Mechanical vibration - road surface profiles - reporting of measured data*.

- Kacin, J., Rizzo, P. and Tajari, M. (2010), *Fatigue analysis of overhead sign support structures*, Eng. Struct., Vol. 32, No. 6, 1659–1670.
- Letchford, C.W. (2001), *Wind loads on rectangular signboards and hoardings*, Journal of Wind Engineering and Industrial Aerodynamics, Vol. 89, No. 2, 135-151.
- Li, X., T. Whalen, and Bowman, M. (2005), *Fatigue Strength and Evaluation of Double-Mast Arm Cantilevered Sign Structures*, Transp. Res. Rec. J. Transp. Res. Board, Vol. 1928, 64–72.
- Martin, K.A., Ehsani, M.R., and Bjorhovde, R. (1987), *Field resting of highway sign support structures*, ASCE Journal of Structural Engineering, Vol. 113, No. 4, 850-863.
- Miner, A. M. (1945), *Cumulative damage in fatigue*, J. Appl. Mech., Vol. 12, No. 3, A-159.
- Moses F, Schilling CG, Raju KS. (1987), *Fatigue evaluation procedures for steel bridges*. Washington, DC..
- Newberry, C. and Eaton, K. (1974), *Wind Loading Handbook*, Building Research Establishment Report, HMSO, London, 1974.
- Prabhakar, S., and Arunachalam, K. (2015), *Simulation and analysis of passive suspension system for different road profiles with variable damping and stiffness parameters*, J. Chem. Pharm. Sci., No. 7, 32–36.
- Rice, J. A., Foutch, D. A., LaFave, J. M., and Valdovinos, S. (2012), *Field testing and analysis of aluminum highway sign trusses*, Eng. Struct., Vol. 34, 173–186.
- Rodi, W, Constantinescu, G. and Stoesser, T. (2013), *Large Eddy Simulation in hydraulics*, IAHR Monograph, CRC Press, Taylor & Francis Group (ISBN-10: 1138000247)
- Roy, S., Park, Y.-C., Sause, R. and Fisher, J. (2010), *Fatigue Performance of Groove-Welded Tube-to-End-Plate Connections in Highway Sign, Luminaire, and Traffic Signal Structures*, Transp. Res. Rec. J. Transp. Res. Board, Vol. 2152, 63–70.
- Sakamoto, H. and Arie, M. (1983), *Flow around a normal plate of finite width immersed in a turbulent boundary layer*, Journal of Fluids Engineering, ASME, Vol. 105, 98-104.
- Sanz-Andrés, A., Santiago-Prowald, J., Baker, C. and Quinn, A. (2003), *Vehicle-induced loads on traffic sign panels*, J. Wind Eng. Ind. Aerodyn., Vol. 91, No. 7, 925–942.
- Sharma, P., Saluja, N., Saini, D. and Saini, P. (2013), *Analysis of Automotive Passive Suspension System with Matlab Program Generation*, Int. J. Adv. Technol., Vol. 4, No. 2.
- Shpetim, S. P. (2012), *Designs and Optimizations of Active and Semi-Active Non-linear Suspension Systems for a Terrain Vehicle*, Strojniški Vestn. -Journal Mech. Eng., Vol. 5812, 732–743.
- Spalart, P. (2009), *Detached eddy simulation*, Annual Review of Fluid Mechanics, Vol. 41, 181-202.

*Texas DOT RiP Project 27756 (2015), Development of design guidelines and mitigation strategies for wind-induced traffic signal structure vibrations, Texas Department of Transportation, Austin, TX.*

Tyan, F., Hong, Y.F., Tu, S.H. Tu, and Jeng, W. S. (2009), *Generation of Random Road Profiles*, J. Adv. Eng., Vol. 4, No. 2, 1373–1378.

Warnitchai, P., S. Sinthuwong, and Poemsantitham, K. (2009), *Wind tunnel model tests of large billboards*, Advances in Structural Engineering, Vol. 12, No. 1, 103-114.

Zuo, D., Smith, D.A., and Mehta, K.C. (2012), *Benchmark wind tunnel study of wind loading on rectangular sign structures*, Seventh International Colloquium on Bluff Body Aerodynamics and Application, Shanghai, China.